

2

~~LEVEL~~  
**NAVAL POSTGRADUATE SCHOOL**  
Monterey, California

AD A102664



DTIC  
ELECT  
S AUG 11 1981

UNC FILE COPY

(9) M. J. J. S. L. 11-13  
**THESIS**

(6)

ACOUSTIC DIFFRACTION BY A FINITE  
BARRIER; THEORIES AND EXPERIMENT

by

(1) Gary M./Jebsen

111 March 1981

(10) 11-12

Thesis Advisor:

H. Medwin

Approved for public release; distribution unlimited

X  
81 8 11 050

Unclassified

SECURITY CLASSIFICATION OF THIS PAGE (When Data Entered)

REPORT DOCUMENTATION PAGE		READ INSTRUCTIONS BEFORE COMPLETING FORM
1. REPORT NUMBER	2. GOVT ACCESSION NO. AD-A102664	3. RECIPIENT'S CATALOG NUMBER
4. TITLE (and Subtitle) Acoustic Diffraction by a Finite Barrier; Theories and Experiment		5. TYPE OF REPORT & PERIOD COVERED Master's Thesis; March 1981
7. AUTHOR(s) Gary M. Jebsen		6. PERFORMING ORG. REPORT NUMBER
9. PERFORMING ORGANIZATION NAME AND ADDRESS Naval Postgraduate School Monterey, California 93940		8. CONTRACT OR GRANT NUMBER(s)
11. CONTROLLING OFFICE NAME AND ADDRESS Naval Postgraduate School Monterey, California 93940		10. PROGRAM ELEMENT, PROJECT, TASK AREA & WORK UNIT NUMBERS
14. MONITORING AGENCY NAME & ADDRESS (if different from Controlling Office)		12. REPORT DATE March 1981
		13. NUMBER OF PAGES 129
		15. SECURITY CLASS. (of this report) Unclassified
		15a. DECLASSIFICATION/DOWNGRADING SCHEDULE
16. DISTRIBUTION STATEMENT (of this Report)  Approved for public release; distribution unlimited		
17. DISTRIBUTION STATEMENT (of the abstract entered in Block 20, if different from Report)		
18. SUPPLEMENTARY NOTES		
19. KEY WORDS (Continue on reverse side if necessary and identify by block number)  Acoustic Diffraction, noise control, baffle, impulse wave		
20. ABSTRACT (Continue on reverse side if necessary and identify by block number) The Biot-Tolstoy (B-T) exact impulse solution of diffraction by an infinite half-plane is compared to the usual Helmholtz-Kirchhoff (H-K) integral formulation and to the exact continuous wave (CW) solution of Macdonald. For backscatter the B-T and H-K solutions are found to differ significantly, especially near the surface of the half-plane, where the B-T solution gives close agreement with experiment. For forward scatter the two exact		

DD FORM 1 JAN 73 1473

EDITION OF 1 NOV 68 IS OBSOLETE  
S/N 0102-014-6401

Unclassified

SECURITY CLASSIFICATION OF THIS PAGE (When Data Entered)

Unclassified

SECURITY CLASSIFICATION OF THIS PAGE (When Data Entered)

Item 20: continued.

solutions and experimental data are in agreement. B-T is found to agree well with measurements of diffraction by a barrier perpendicular to a rigid base. By considering source and source image in the base separately the concept of "image of the source in the barrier" is found to be unnecessary. Use of the time domain form of B-T solution in calculating the forward diffraction near a corner and behind a thin strip is shown to give results which agree well with measured data. Secondary diffraction effects are observed in the measurements of diffraction by a thin strip, a non-vertical barrier and a thick edge.

Accession For	
NTIS GRA&I	<input checked="checked" type="checkbox"/>
DTIC TAB	<input type="checkbox"/>
Unannounced	<input type="checkbox"/>
Justification	
By _____	
Distribution/	
Availability Codes	
Avail and/or	
Dist	Special
A	

Approved for public release; distribution unlimited

Acoustic Diffraction by a Finite  
Barrier; Theories and Experiment

by

Gary M. Jebsen  
B.S., Florida Atlantic University, 1969

Submitted in partial fulfillment of the  
requirements for the degree of

MASTER OF SCIENCE IN ENGINEERING ACOUSTICS

from the

NAVAL POSTGRADUATE SCHOOL  
March 81

Author:

Gary M. Jebsen

Approved by:

William Dyer

Thesis Advisor

W. W. Walker

Second Reader

W. Dyer  
Chairman, Department of Physics and Chemistry

William M. Jolley  
Dean of Science and Engineering

## ABSTRACT

The Biot-Tolstoy (B-T) exact impulse solution of diffraction by an infinite half-plane is compared to the usual Helmholtz-Kirchhoff (H-K) integral formulation and to the exact continuous wave (CW) solution of Macdonald. For backscatter the B-T and H-K solutions are found to differ significantly, especially near the surface of the half-plane, where the B-T solution gives close agreement with experiment. For forward scatter the two exact solutions and experimental data are in agreement. B-T is found to agree well with measurements of diffraction by a barrier perpendicular to a rigid base. By considering source and source image in the base separately the concept of "image of the source in the barrier" is found to be unnecessary. Use of the time domain form of the B-T solution in calculating the forward diffraction near a corner and behind a thin strip is shown to give results which agree well with measured data. Secondary diffraction effects are observed in the measurements of diffraction by a thin strip, a non-vertical barrier and a thick edge.

## TABLE OF CONTENTS

I.	INTRODUCTION .....	7
II.	THEORETICAL APPROACH .....	9
	A. GENERAL .....	9
	B. BIOT-TOLSTOY FORMULATION .....	10
	C. HELMHOLTZ-KIRCHHOFF FORMULATION .....	23
	D. MACDONALD'S FORMULATION .....	26
III.	COMPARISON OF SOLUTIONS .....	28
	A. BIOT-TOLSTOY AND HELMHOLTZ-KIRCHHOFF .....	28
	B. BIOT-TOLSTOY AND MACDONALD .....	42
IV.	EXPERIMENTAL APPROACH .....	50
	A. GENERAL .....	50
	B. DATA ACQUISITION .....	50
	C. SOUND SOURCE .....	53
	D. PLATE CONSIDERATIONS .....	60
V.	BACKSCATTER EXPERIMENTAL RESULTS .....	61
VI.	FINITE PLATE FORWARD SCATTERING RESULTS .....	66
	A. GENERAL .....	66
	B. FORWARD DIFFRACTION AT A CORNER .....	68
	C. FORWARD DIFFRACTION BY A STRIP .....	85
	D. FORWARD DIFFRACTION BY A THICK BARRIER ---	96
	E. FORWARD DIFFRACTION BY A BARRIER ON A RIGID BASE .....	100
VII.	CONCLUSIONS .....	114

APPENDIX: A APPROXIMATION OF THE BIOT-TOLSTOY SOLUTION NEAR THE SHADOW BOUNDARY -----	116
LIST OF REFERENCES -----	125
INITIAL DISTRIBUTION LIST -----	127

## I. INTRODUCTION

Many practical problems in acoustics are complicated by the presence of boundaries which influence the sound field in some way. When the direct path between source and receiver is not obstructed, these boundaries represent a perturbation to the free field solution. If the boundaries are infinite in extent, the image or normal mode methods are often applied. Finite boundaries introduce the additional phenomenon of diffraction or scattering, which is often treated as an additional perturbation to the free-field plus reflection solution. When the finite boundary is such that it blocks the direct path the problem is somewhat different.

In this case, the only sound reaching the receiver is that which has been diffracted at the edge of the finite boundary (assuming the boundary to be rigid). In terms of airborne noise control a finite boundary that blocks the direct path is often called a barrier or screen. When a similar technique is applied to the reduction of unwanted sound in a shipboard sonar system, the boundary is generally called a baffle. The location and size of baffles on submarines and surface ships are severely constrained by the size of the ships themselves. As a result, the baffle is often close to the radiating source and the receivers close to the baffle. Care must be used in selecting a theoretical



approach to solving the diffraction problem under these circumstances since some of the techniques in general use involve simplifying assumptions which may not be valid under these rigorous conditions.

Much work on the solution to the barrier problem may be found in the noise control literature. In this paper, two solutions used in noise control are examined, along with the little known solution by Biot and Tolstoy, and the theoretical results are compared. In addition, experimental results relating to the application of theoretical solutions to finite barriers are presented.

## II. THEORETICAL APPROACH

### A. GENERAL

The usual approach to solving the problem of diffraction by a plate or barrier is to approximate the barrier mathematically as an infinitely thin, opaque, half-plane. This problem was first solved by Sommerfeld [Ref. 1] for plane continuous waves and then by Carslaw [Ref. 2] for spherical continuous waves. Macdonald's [Ref. 3] work for spherical continuous waves is often referenced as the rigorous solution to diffraction by a wedge (and hence the half-plane). In 1957 Biot and Tolstoy [Ref. 4] published their exact impulse solution using the normal coordinate formulation. Despite the fact that the Biot-Tolstoy impulse solution is in closed form and contains only simple functions, many authors in the noise reduction field still consider Macdonald as the only exact solution [Ref. 5].

A second general approach to the problem is Kirchhoff's approximate solution to the integral equation formulation of Huygens' Principle. This approach has been used extensively in both optics and acoustics and can be shown to give reasonable agreement with observed results, within certain limits, in spite of the fact that the basic simplifying assumptions are generally acknowledged to be incorrect [Ref. 6].

There are additional approaches to this problem that will not be explored here. A good summary of the various solutions in the context of the noise control barrier can be found in Reference 5.

Rigorous derivation of the three theories will not be attempted, however the development of each will be summarized in order that basic differences can be understood.

#### B. BIOT-TOLSTOY FORMULATION

M.A. Biot and I. Tolstoy published their landmark paper [Ref. 4] on the normal coordinate approach to wave propagation in infinite media in 1957. Within this paper was an application of the normal coordinate approach in solving the problem of diffraction from an infinite wedge which forms the basis for the theoretical results in this paper. The important features of their work in the present application are as follows:

- a. The solution is exact and in closed form.
- b. The solution can be expressed in elementary functions.
- c. The use of an impulse source provides insight into the contributions from various edges and a means of separating the diffracted from reflected and direct components.

The extension of their results to other types of sources is straightforward.

The normal coordinate approach is related to the normal mode description in acoustics which is most often encountered

in the solution of problems where the medium is bounded such as room acoustics, shallow water sound propagation, and speaker enclosures. In these cases the normal coordinates are the allowable modes of vibration (normal modes) of the system. The overall response of the system is the superposition of these discrete normal modes. Stated another way, an external source excites all modes at various amplitudes and phases and the solution then is the coherent sum of all these individual excitations. The essence of the normal coordinate approach to the solution of general diffraction problems is the extension of the principle of superposition of normal modes to infinite media. As the boundaries of the "enclosure" are removed toward infinity the spacing between normal modes becomes progressively less, with the limit being a continuous response spectrum with the boundaries at infinity. If we now introduce a source which "turns on" at time  $t = 0$  (a transient source), the solution contains only waves traveling outward and no radiation condition need be imposed. The solution summarized here is taken primarily from Reference 7.

In order to formulate the problem of diffraction by a wedge, a cylindrical coordinate system is chosen with the origin at the wedge crest and the  $z$ -axis along the crest as shown in Figure 1. In this system the acoustic wave equation, in terms of displacement potential  $\phi$ , is written as

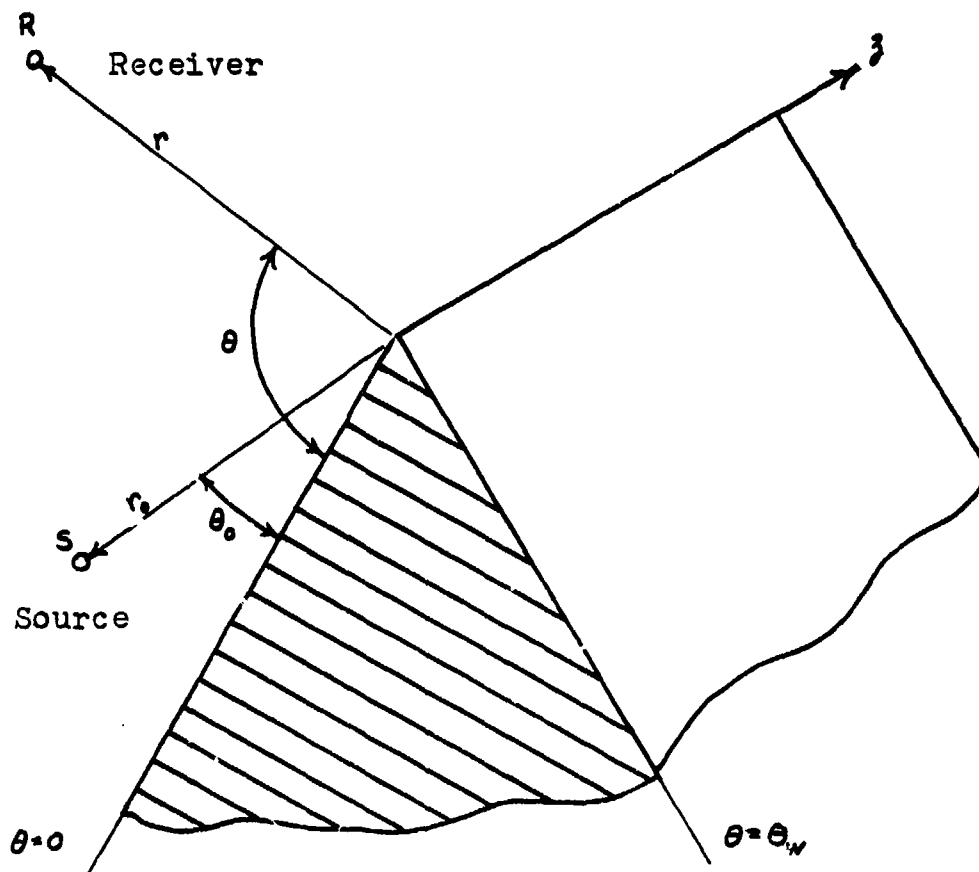


Figure 1. General Infinite Wedge Diffraction Coordinate System.

$$\frac{\partial^2 \phi}{\partial r^2} + \frac{1}{r} \frac{\partial \phi}{\partial r} + \frac{1}{r^2} \frac{\partial^2 \phi}{\partial \theta^2} + \frac{\partial^2 \phi}{\partial z^2} - \frac{1}{c^2} \frac{\partial^2 \phi}{\partial t^2} = 0 \quad (\text{II-1})$$

By separation of variables the harmonic solutions are

$$\phi = e^{\pm i\nu\theta} H_{\nu}^{(1,2)}(\kappa r) e^{\pm i\gamma z} e^{\pm i\omega t} \quad (\text{II-2})$$

where the separation constants are related by

$$\gamma^2 = \frac{\omega^2}{c^2} - \kappa^2, \quad k = \frac{\omega}{c}$$

Applying the boundary conditions for a rigid wedge,

$$\frac{\partial \phi}{\partial \theta} = 0; \quad \theta = 0, \theta = \theta_w$$

restricting the amplitude to be finite at  $r = 0$ , and choosing a location for our point source ( $r = r_0$ ,  $\theta = \theta_0$ ,  $z = 0$ ) that will result in  $z$ -axis symmetry, the solution is written as

$$\phi_n = J_{\nu_n}(\kappa r) \cos \nu_n \theta \cos \gamma_n z e^{\pm i\omega t} \quad (\text{II-3a})$$

$$\nu_n = \frac{n\pi}{\theta_w} \quad (\text{II-3b})$$

The solution can be separated into space-dependent and time dependent parts,

$$\phi_n = q_n \psi_n \quad (\text{II-4a})$$

$$\psi_n = J_{\nu_n}(\kappa r) \cos \nu_n \theta \cos \gamma_n z \quad (\text{II-4b})$$

The  $q_n$  are the normal coordinates which satisfy the differential equation

$$\ddot{q}_n + \omega^2 q_n = \frac{Q_n}{u_n} \quad (\text{II-5})$$

here  $Q_n$  is the generalized source function and  $u_n$  is proportional to the kinetic energy in each mode. The series represented by (II-4) is known to be orthogonal and may be normalized by the condition

$$u_n = \rho \int_0^{\theta_w} d\theta \int_{-\infty}^{+\infty} dz \int_0^{\infty} (\nabla \psi_n)^2 r dr$$

The medium is infinite in the  $r$  and  $z$  directions resulting in divergent integrals. These are handled by Tolstoy using a symbolic limiting procedure (discussed in detail in Reference 7, section 8-2) resulting in the following expression

$$u_n = \frac{\rho}{2} \theta_w \frac{\omega^2}{c^2} \frac{\pi}{k dk dy} \quad (\text{II-6})$$

It is at this point that we must choose an appropriate form for the generalized source,  $Q_n$ .

The usual approach (and the one which we will ultimately use) is to choose the delta function or unit impulse source. It has two distinct advantages over other forms. First, it will result in a solution identical to that achieved via the Green's function approach, at least for those modes which are physically realizable. Second, it provides a simple building block with which the solution for other source forms can be constructed through the application of Duhamel's theorem. The result is analogous to analysis of electronic filters: the response of the system to a unit impulse input is the

system impulse response. The system transfer function is the Fourier transform of this impulse response.

Biot and Tolstoy choose the source such that the displacement potential at a distance  $R$  is of the form

$$\phi = - \frac{1}{4\pi R} l(t - R/C) \quad (\text{II-7})$$

where  $l(t - R/C)$  is the unit step function having the value zero for  $(t - R/C) < 0$  and one for  $(t - R/C) > 0$ . This represents the instantaneous injection of a unit volume at the source coordinates and is commonly used as a mathematical approximation to an explosion. Since the pressure and displacement are related by

$$p = - \rho \frac{\partial^2 \phi}{\partial t^2} \quad (\text{II-8})$$

the pressure at a distance  $R$  due to the source function of Equation (II-8) will be

$$p = \frac{\rho}{4\pi R} \frac{d}{dt} [\delta(t - R/C)]$$

However, Medwin [Ref. 8] derives the solution for an impulse source directly from Biot-Tolstoy by simply taking the pressure to be proportional to the Biot-Tolstoy expression for particle velocity, since the two source functions differ by a first derivative. Medwin shows that this is equivalent to assuming a point source of strength  $S$  (volume per time) which flows uniformly beginning at time  $t = 0$ . The acoustic pressure at range  $R$  due to this source is given by



$$Q_n = -\lambda 1(-t) [\nabla^2 \psi_n]_0 \quad (\text{II-10})$$

where  $\lambda$  is the bulk modulus of the fluid, and  $\psi_n$  is the space dependent solution for the free modes (Equation II-4). The Laplacian of  $\psi_n$ , in brackets, is evaluated at the location of the source. Substituting (II-4) into (II-10) and utilizing (II-6), the differential Equation (II-5) can be written as

$$\ddot{q}_n + \omega^2 q_n = \frac{2C^2}{\pi \theta_w} 1(-t) J_{\nu_n}(\kappa r_0) \cos \nu_n \theta_0 \kappa d\kappa d\gamma \quad (\text{II-11})$$

The solution to (II-11) represents the normal coordinates for the problem,

$$q_n = \frac{\cos \omega t}{\omega^2} \frac{2C^2}{\pi \theta_w} J_{\nu_n}(\kappa r_0) \cos \nu_n \theta_0 \kappa d\kappa d\gamma \quad t \geq 0 \quad (\text{II-12})$$

Substituting into (II-4a) and taking the time derivative, the solution can be written as

$$\frac{\partial \phi}{\partial t} = - \frac{2C^2}{\pi \theta_w} \sum_n \cos \nu_n \theta \cos \nu_n \theta_0 \int_0^\infty \int_0^\infty J_{\nu_n}(\kappa r) J_{\nu_n}(\kappa r_0) \cos \gamma z X \frac{\sin \omega t}{\omega^2} \kappa d\kappa d\gamma \quad (\text{II-13})$$

Equation (II-13) represents an exact solution to the perturbation of a propagating wave by the presence of a rigid wedge, assuming Equation (II-10) as the form of the source. Its present form is not particularly useful, however the application of two known integral transforms to Equation (II-13) reveals its simplicity and its close relationship to the physical problem in an intuitively

satisfying way. The application of these transforms is discussed next.

Equation (II-13) contains integrals with respect to both the z-axis wavenumber  $\gamma$  and the radial wavenumber  $\kappa$ . Considering the integration over  $\gamma$  first,

$$\int_0^{\infty} \cos \gamma z \frac{\sin \omega t}{\omega^2} d\gamma = \frac{1}{c} \int_0^{\infty} \cos \gamma z \frac{\sin ct (\gamma^2 + \kappa^2)^{\frac{1}{2}}}{(\gamma^2 + \kappa^2)^{\frac{1}{2}}} d\gamma \quad (\text{II-14})$$

and the relationship of the separation constants

$$\omega^2 = c^2 (\gamma^2 + \kappa^2)$$

The integral on the RHS of Equation (II-14) represents a known integral transform, as follows [Ref. 7]:

$$\begin{aligned} \frac{1}{c} \int_0^{\infty} \cos \gamma z \frac{\sin ct (\gamma^2 + \kappa^2)^{\frac{1}{2}}}{(\gamma^2 + \kappa^2)^{\frac{1}{2}}} d\gamma &= \frac{\pi}{2c} J_0 [\kappa (c^2 t^2 - z^2)^{\frac{1}{2}}] \quad ct > z \\ &= 0 \quad ct < z \end{aligned} \quad (\text{II-15})$$

The existence of two distinct forms of the solution, one of which is zero, is a direct consequence of the choice of a transient source, i.e. if the source is turned on at  $t = 0$  there can be no effect at the receiver until a time equal to the source/receiver separation distance divided by the propagation speed. In this case,  $z$  is one component of that separation vector.

Using the result of (II-15) the remaining integral of (II-13) may be written as

$$I_n = \int_0^{\infty} J_{\nu_n}(\kappa r) J_{\nu_n}(\kappa r_0) J_0[\kappa(c^2 t^2 - z^2)^{1/2}] \kappa d\kappa \quad (\text{II-16})$$

This integral has a known solution which takes on three different forms depending upon the relationship of the variables  $r$ ,  $r_0$ , and  $(c^2 t^2 - z^2)^{1/2}$ . Tolstoy [Ref. 7] defines these three regions in terms of the propagation time of a pulse emitted by the source at  $t = 0$ . The time of arrival (at the receiver) of the earliest possible direct pulse is given by

$$t_1 = \frac{1}{c} [(r - r_0)^2 + z^2]^{1/2}$$

The earliest time of arrival of the pulse which has traveled from source to receiver via the crest of the wedge is

$$\tau_0 = \frac{1}{c} [(r + r_0)^2 + z^2]^{1/2}$$

With these new variables, the three regions of the solution are given by

$$\text{I.} \quad t < t_1 \quad I_n = 0 \quad (\text{II-17})$$

$$\text{II.} \quad t_1 < t < \tau_0 \quad I_n = (\pi r r_0 \sin X)^{-1} \cos \nu_n X$$

$$X = \arccos \frac{r^2 + r_0^2 + z^2 - c^2 t^2}{2 r r_0} \quad 0 \leq X \leq \pi \quad (\text{II-18})$$

$$\text{III.} \quad \tau_0 < t \quad I_n = -(\pi r r_0 \sinh Y)^{-1} \sin(\nu_n \pi) e^{-\nu_n Y}$$

$$Y = \operatorname{argcosh} \frac{c^2 t^2 - (r^2 + r_0^2 + z^2)}{2 r r_0} \quad (\text{II-19})$$

These three regions have a strong intuitive foundation. In Case I. it is obvious that a pulse transmitted by the source cannot be received until a finite time has elapsed, that time being equal to the separation divided by the propagation speed. Case II. represents that time during which reflections from the face of the wedge are received. Tolstoy [Ref. 7] shows that when this expression for  $I_n$  is substituted into Equation (II-13), the solution takes the form of images of the source in the reflecting wall. Finally, Case III. is the diffracted wave. It is characterized by an arrival time which is later than the last possible image source arrival, as seen from Figure 1.

The same results can also be interpreted geometrically, as discussed by Watson [Ref. 9]. If we rename the variables  $r$ ,  $r_0$ , and  $(c^2t^2 - z^2)^{1/2}$  in (II-16) as  $b$ ,  $c$ , and  $a$ , respectively, Watson points out that the three regions of the solution can be described in terms of the geometry of Figure 2 ( $z$  is taken to be zero for simplicity). The solution of Case II. applies whenever the value of side  $a$  is such that a triangle can be formed having sides  $a$ ,  $b$ ,  $c$ . It is obvious that this will be the case whenever  $a$  has the values

$$(b-c) < a < (b+c)$$

and, from the law of cosines, the angle  $A$  will be given by

$$A = \arccos \frac{b^2 + c^2 - a^2}{2bc} \quad (\text{II-20})$$

where  $A$  can take on values between 0 and  $\pi$ . The comparison with Equation (II-18) is immediate. In Case III.,  $a$  is

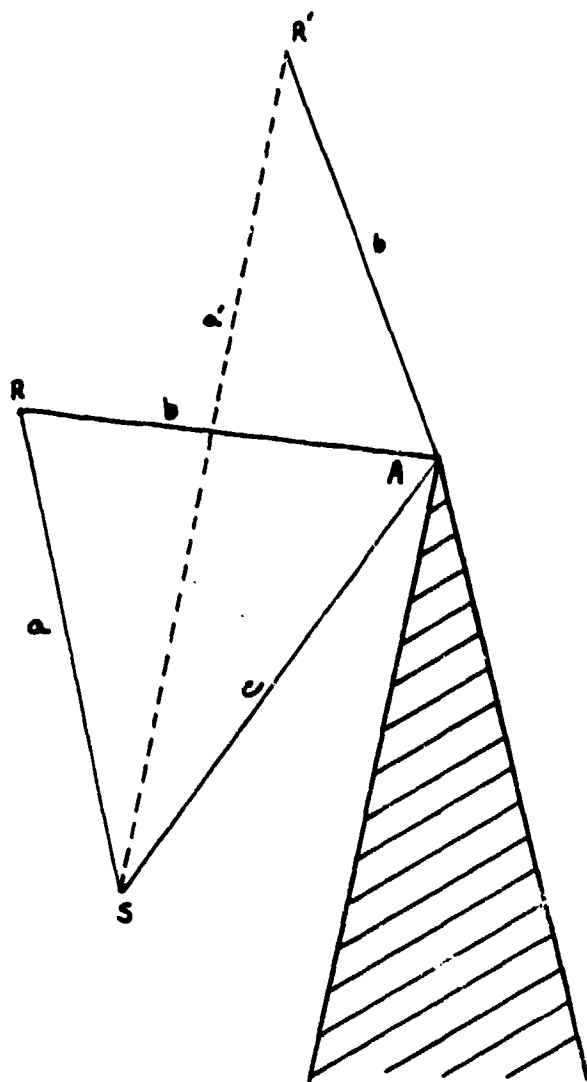


Figure 2. Source, Receiver, and Wedge Crest Geometry.

greater than  $(b+c)$ , the angle  $A$  becomes imaginary, and the expression corresponding to (II-20) must come from hyperbolic trigonometry:

$$A = \operatorname{argcosh} \frac{a^2 - b^2 - c^2}{2bc} \quad (\text{II-21})$$

It can be seen from this discussion that the Biot-Tolstoy formulation in the time domain decomposes into direct/reflected and diffracted components in an intuitively satisfying way. This is apparently due to the use of the normal coordinate formulation, which considers only modes which are physically realizable, and the choice of the transient form of the source. However, because of this distinct division between direct and diffracted solutions, considerable care must be exercised when working with a geometry where the arrival times of the direct and diffracted waves are close, such as near the boundary between the "illuminated" region and the geometric shadow.

To arrive at the final solution for the diffracted wave, the result of Equation (II-19) is applied to the general solution (II-13) as follows:

$$\frac{\partial \phi}{\partial t} = \frac{c}{\pi \theta_w} (rr_o \sinh Y)^{-1} \sum_{n=0}^{\infty} \cos v_n \theta_o \cos v_n \theta \sin v_n \pi e^{-v_n Y} \quad (\text{II-22})$$

$$v_n = \frac{n\pi}{\theta_w}$$

Expressing the sum in terms of exponentials, regrouping, and collecting in conjugate pairs, the solution can be written in exact, closed form as

$$\frac{\partial \phi}{\partial t} = \frac{c}{4\pi\theta_w} (rr_0 \sinh Y)^{-1} e^{-\frac{\pi Y}{\theta_w}} \left\{ \frac{\sin\left(\frac{\pi}{\theta_w}(\pi \pm \theta \pm \theta_0)\right)}{1 - 2e^{-\frac{\pi Y}{\theta_w}} \cos\left(\frac{\pi}{\theta_w}(\pi \pm \theta \pm \theta_0)\right) + e^{-\frac{2\pi Y}{\theta_w}}} \right\} \quad (\text{II-23a})$$

$$Y = \operatorname{argcosh} \frac{c^2 t^2 - (r^2 + r_0^2 + z^2)}{2rr_0} \quad (\text{II-23b})$$

where the term  $(\pi \pm \theta \pm \theta_0)$  indicates that the entire expression within the curly brackets is the sum of four terms, each of which corresponds to a unique combination of  $(\pi \pm \theta \pm \theta_0)$ .

Recalling the discussion concerning the forms of the impulse source, Equation (II-23) can now be used in place of the second partial derivative in (II-8) and the solution of the diffracted wave in terms of pressure can be written as

$$p(t) = - \frac{\rho c S}{4\pi\theta_w} (rr_0 \sinh Y)^{-1} e^{-\frac{\pi Y}{\theta_w}} \{\beta\} \quad (\text{II-24})$$

where  $Y$  is given by Equation (II-23b) and  $\beta$  represents the term in curly brackets in Equation (II-23a).

Equation (II-24) represents the diffracted pressure as a function of time due to a unit impulse source. To within a constant representing the source strength, this is analogous to the impulse response,  $h(t)$ , of a general linear system. This impulse response is often Fourier transformed to obtain the transfer function  $H(\omega)$  and examined in the frequency domain. Since there is no known analytical transform of

of Equation (II-24), the numerical technique of computing the impulse response in discrete time steps and then transforming using the Fast Fourier Transform (FFT) is employed. To avoid the problem of infinite values of  $h(t)$  for the earliest diffracted arrival, Medwin uses an approach which computes the first time point by a numerical integration. All of the Biot-Tolstoy theoretical results presented in this paper are calculated in this way.

### C. HELMHOLTZ-KIRCHHOFF FORMULATION

The Helmholtz-Kirchhoff formulation is a mathematical statement of the heuristic description of wave propagation due to Huygens. Simply stated, a source at some distance from the surface (in this case a plate which has one straight edge and extends to infinity in three directions) insonifies all points on the surface  $S$ . Each small area element,  $ds$ , on the surface then acts as a point source of spherical waves. At some observation point  $Q$ , the acoustic field is due to the incoming waves from the source directly plus the sum of the contributions from all of the point sources on the surface. Neglecting the effect of the direct incoming waves at  $Q$ , the field can be determined by integrating over the surface. To construct an exact solution in this manner one would have to know the amplitude and phase of each point "source" on the surface. This not possible, in general, and therefore the Kirchhoff approximation is used. The brief development



given herein follows that in Clay and Medwin [Ref. 10]. A detailed derivation can be found in most optics texts and in a book by Baker and Copson [Ref. 6].

From Green's theorem, assuming a source of time dependence  $e^{i\omega t}$ , the field at the observation point Q can be expressed as

$$U(Q) = \frac{1}{4\pi} \int_S \left[ U \frac{\partial}{\partial n} \left( \frac{e^{-ikR}}{R} \right) - \frac{e^{-ikR}}{R} \left( \frac{\partial U}{\partial n} \right) \right]_s ds \quad (\text{II-25})$$

where R is the distance from each element ds to the observation point Q and  $\frac{e^{-ikR}}{R}$  is the free space Green's function. That the integrand is evaluated on the surface is denoted by the subscript s on the brackets. This known as the Helmholtz-Kirchhoff integral. It describes the relationship of the field at Q to the field on S, but the problem of evaluating the field on S is not yet resolved.

Equation (II-25) can be used to evaluate the diffracted wave field on either side of the surface. Our primary interest is the diffracted field when source and receiver are on opposite sides of the surface, however, when they are on the same side (herein referred to as backscatter) the resulting expressions can be somewhat simplified. Since the purpose of this development is to compare the results with those of the normal coordinate approach, the simpler case will be used. For a complete treatment of this Helmholtz-Kirchhoff integral equation approach, see Baker and Copson [Ref. 6].

If  $U_s$  is defined as the incident wave field at the location of the surface, with the surface removed, then the quantity  $U$  within the integral can be approximated by

$$U = MU_s \quad (\text{II-26})$$

where  $M$  is the plane wave reflection coefficient. From equation (II-26) the normal derivative can be written as

$$\frac{\partial U}{\partial n} = -M \frac{\partial U_s}{\partial n} \quad (\text{II-27})$$

By Equation (II-26), the restriction has been imposed that the only wave field that can exist on the insonified surface of the barrier is that due to reflection of the incident wave field (i.e., there can be no scattered field on the surface). The consequence of this assumption will be seen when the diffracted field near the surface is examined.

The additional assumption that is required to make the integral in (II-25) tractable concerns the reflection coefficient  $M$ . Kirchhoff's assumption considers it to be equal to the plane wave reflection coefficient for an infinite plane interface. Here the surface is assumed to be perfectly rigid and  $M = 1$ . Equation (II-25) can now be written as

$$U(Q) = \frac{1}{4\pi} \int_S \frac{\partial}{\partial n} \left( U_s \frac{e^{-ikR}}{R} \right) ds \quad (\text{II-28})$$

When the integral in Equation (II-28) is taken over the surface of the half-plane, the  $U(Q)$  represents the backscattered wave field. If, on the other hand, the integral in Equation (II-28) is taken over the portion of the plane not

occupied by the surface (generally referred to as the aperture in optics literature),  $U(Q)$  would represent the wave field scattered forward into the shadow region on the side of the half-plane opposite the source. (Note that this approach would also require a change of sign due to Equation (II-27)).

#### D. MACDONALD'S FORMULATION

The final theoretical development to be considered here is that of Macdonald [Ref. 3]. His solution, like Biot-Tolstoy, is an exact solution for the infinite rigid wedge, except that Macdonald assumes a continuous wave (cw) source. A derivation of his solution will not be attempted, instead, the results of Kawai, Fujimoto and Itow [Ref. 11] will be used. The calculations in their paper are based on an approximate form of Macdonald's solution given by Bowman and Senior [Ref. 12] but only the form of the exact solution is presented below.

From Reference 11 the exact solution can be written in terms of the velocity potential as

$$v = V(\theta_0) + V(-\theta_0)$$

$$v = ik \int_{-T_R}^{\infty} \frac{H_1^{(1)}(T^2 + kR)}{(T^2 + 2kR)^{1/2}} dT + ik \int_{-T_R}^{\infty} \frac{H_1^{(1)}(T^2 + kR)}{(T^2 + 2kR)^{1/2}} dT \quad (\text{II-29})$$

where

$$T_R = \text{sgn}(\pi - \theta - \theta_0) (kR_1 - kR)^{1/2} \quad (\text{II-30a})$$

$$T_{R^-} = \text{sgn}(\pi - \theta - \theta_0) (kR_1 - kR^-)^{1/2} \quad (\text{II-30b})$$

$$\text{sgn}(X) = \begin{cases} +1 & X > 0 \\ -1 & X < 0 \end{cases}$$

$$R = (r^2 + r_0^2 + z^2 - 2rr_0 \cos(\theta + \theta_0))^{1/2} \quad (\text{II-31a})$$

$$R' = (r^2 + r_0^2 + z^2 - 2rr_0 \cos(\theta + \theta_0))^{1/2} \quad (\text{II-31b})$$

$$R_1 = ((r + r_0)^2 + z^2)^{1/2} \quad (\text{II-31c})$$

$$k = \omega/c$$

$r, r_0, z, \theta, \theta_0$  as defined in Figure 1

and  $H_1^{(1)}$  is the first order Hankel function of the first kind.

The significant feature of this solution, first pointed out by Macdonald [Ref. 3], is that it consists of the sum of two velocity potentials,  $V(\theta_0)$  and  $V(-\theta_0)$ . These are identified in the noise control literature as the source and the "image of the source in the barrier", respectively. This important interpretation of the solution will be discussed in a later section.

### III. COMPARISON OF SOLUTIONS

#### A. BIOT-TOLSTOY AND HELMHOLTZ-KIRCHHOFF

Biot-Tolstoy (B-T) and Helmholtz-Kirchhoff (H-K) solutions will be compared by choosing a geometry in which both can be expressed in closed form. The backscatter case is chosen wherein source and receiver are in the same location. For this case the time domain solution for the H-K formulation is derived from Equation (II-28), once again following the development in Clay and Medwin [Ref. 10] with some minor changes in notation.

Taking source and receiver to be in the same location (backscatter only) and assuming an impulse source,  $U_s$  in Equation (II-28) can be written as

$$U_s = \frac{e^{-ikR}}{R} \quad (\text{III-1})$$

Making this substitution and transforming the surface integral into an integral along the edge [Ref. 10, pg. 323] Equation II-28) can be written as follows:

$$\begin{aligned} U(Q) &= \frac{\gamma}{4\pi} \int_{-\frac{\pi}{2}}^{\frac{\pi}{2}} \int_{-\infty}^{\infty} d \left[ \frac{e^{-2ikR}}{R^2} \right] d\alpha \\ &= \frac{\gamma}{4\pi} \int_{-\frac{\pi}{2}}^{\frac{\pi}{2}} \left[ \frac{e^{-2ikR}}{R^2} \right]_{-\infty}^{\infty} d\alpha \end{aligned} \quad (\text{III-2})$$

here  $y$ ,  $\alpha$ , and  $R$  are defined as shown in Figure 3. If the  $y$  axis line through  $Q$  intersects the rigid half-plane, the integrand of equation (III-2) is represented by

$$\left[ \frac{y}{\infty} \right] + \left[ \frac{y}{r} \right] \quad (\text{Case I})$$

If not, the integrand becomes

$$\left[ \frac{r}{\infty} \right] \quad (\text{Case II})$$

Taking the inverse Fourier transform of (III-2), and denoting the time domain solution by a small  $u$ ,

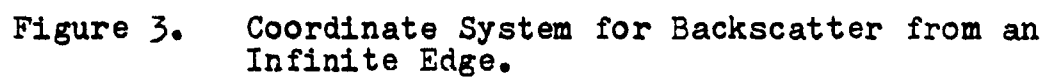
$$u(Q) = \frac{y}{4\pi} \int_{-\infty}^{\infty} \int_{-\frac{\pi}{2}}^{\frac{\pi}{2}} \frac{e^{-2ikR}}{R^2} \left[ \frac{r}{\infty} e^{i\omega t} \right] df d\alpha \quad (\text{III-3})$$

For Case I this becomes

$$u(Q) = \left[ \frac{\delta(t - \frac{2y}{c})}{4\pi y} \right] + \left[ \frac{\delta(t - \frac{2y}{c})}{4 y \pi} - \frac{y}{4\pi} \int_{-\infty}^{\infty} \int_{-\frac{\pi}{2}}^{\frac{\pi}{2}} \frac{e^{i(\omega t - 2kr)}}{r^2} d\alpha df \right] \quad (\text{III-4})$$

Where  $\delta$  represents the Dirac delta function, a consequence of the choice of the Green's function of the Helmholtz equation for the incident wave field.

The first bracket on the right hand side of (III-4) represents the reflection from one half of an infinite plane.



The second bracket contains the specular reflection from the other half of the plane but reduced by the integral expression representing the fact that the plate is finite. This is in the form of an integral along the edge. Following Clay and Medwin [10], this is called the boundary wave and defined as follows:

$$D(t) = \frac{c^2}{4} \int_{-\infty}^{\infty} \int_{-\frac{\pi}{2}}^{\frac{\pi}{2}} \frac{e^{i(\omega t - 2kr)}}{r^2} d\alpha df \quad (\text{III-5})$$

Case II results in a similar expression but without the reflection.

In terms of Equation (III-5) the following expressions are written for the time domain impulse solution:

$$u(Q) = \left[ \frac{\delta(t - \frac{2y}{c})}{2y} - \frac{y}{\pi c^2} D(t) \right] \quad (\text{Case I}) \quad (\text{III-6})$$

$$u(Q) = \frac{y}{\pi c^2} D(t) \quad (\text{Case II}) \quad (\text{III-7})$$

Taking advantage of the time domain form of the solution and separating the reflected and diffracted (boundary wave) components of the wave field results in

$$u(Q) = \mp \frac{y}{\pi c^2} D(t) \quad \begin{array}{l} (-) \text{ Case I} \\ (+) \text{ Case II} \end{array}$$

This can be written in terms of the geometry of Figure 3 as follows (from reference 10, section 10.2.3)



$$u(Q) = \frac{y}{\pi c^2} \left\{ \frac{2T_x}{t(t^2 + T_x^2 - \tau_0^2)(t^2 - \tau_0^2)^{1/2}} \right\} \quad t \geq \tau_0 \quad (\text{III-8a})$$

$$= 0 \quad t < \tau_0 \quad (\text{III-8b})$$

where

$$\begin{aligned} T_x &= \frac{2x_1}{c} = - \frac{2r}{c} \cos \theta = - \tau_0 \cos \theta \\ y &= \frac{ct_0}{2} \\ \tau_0 &= \frac{2R}{c} \end{aligned}$$

Finally, through trigonometric substitutions,

$$u(Q) = - \frac{2}{\pi c^3} \left\{ \frac{r^2 \sin 2\theta}{t(t^2 - t_0^2)(t^2 - \tau_0^2)^{1/2}} \right\} \quad (\text{III-9})$$

The diffracted pressure at Q as a function of time is given by

$$p_d(t, Q) = - P_\delta R_0 u(Q) \quad (\text{III-10})$$

where  $P_\delta$  is the source pressure spectral density and  $R_0$  is the reference distance. Taking the product  $P_\delta R_0 = 1$  Pascal meter, the diffracted pressure at Q, as a function of time, can be written as

$$\begin{aligned} p_d(t, Q) &= - u(Q) \\ &= - \frac{2}{\pi c^3} \left\{ \frac{r^2 \sin 2\theta}{t(t^2 - t_0^2)(t^2 - \tau_0^2)^{1/2}} \right\} \end{aligned} \quad (\text{III-11})$$

The corresponding expression for the Biot-Tolstoy formulation can be obtained from equation (II-22). For the thin plate ( $\theta_w = 2\pi$ ),

$$\frac{\partial \phi}{\partial t} = \frac{c}{2\pi^2} (rr_0 \sinh Y)^{-1} \sum_n \cos \frac{n\theta}{2} \cos \frac{n\theta_0}{2} \sin \frac{n\pi}{2} e^{-\frac{nY}{2}} \quad (\text{III-12})$$

Working with the sum and noting that  $\theta = \theta_0$  (source and receiver coincident),

$$S = \sum_n \cos^2 \frac{n\theta}{2} \sin \frac{n\pi}{2} e^{-\frac{nY}{2}} = \sum_n \frac{1}{2} \left( 1 + \frac{e^{in\theta} - e^{-in\theta}}{2} \right) \sin \frac{n\pi}{2} e^{-\frac{nY}{2}}$$

Multiplying terms and observing that  $\sin \frac{n\pi}{2}$  is zero for  $n$  even and  $\pm 1$  for  $n$  odd, the sum can be evaluated as

$$\begin{aligned} S &= \frac{1}{2} \left( e^{-\frac{Y}{2}} - e^{-\frac{3Y}{2}} + e^{-\frac{5Y}{2}} - \dots \right) + \\ &+ \frac{1}{4} \left( e^{-u_1} - e^{-3u_1} + e^{-5u_1} - \dots \right) + \\ &+ \frac{1}{4} \left( e^{-u_2} - e^{-3u_2} + e^{-5u_2} - \dots \right) \\ &= \frac{1}{4} \operatorname{sech} \frac{Y}{2} + \frac{1}{8} \operatorname{sech} u_1 + \frac{1}{8} \operatorname{sech} u_2; \quad \operatorname{Re}\left(\frac{Y}{2}\right) > 0 \end{aligned} \quad (\text{III-13})$$

where

$$u_1 = \frac{Y}{2} - i\theta$$

$$u_2 = \frac{Y}{2} + i\theta$$

After considerable manipulation the sum can be written as

$$s = \frac{i}{4} \left[ \frac{2 \cosh^2 \frac{Y}{2} \cos \theta + \cosh Y + \cos 2\theta}{(\cosh Y + \cos 2\theta) \cosh \frac{Y}{2}} \right] \quad (\text{III-14})$$

From the geometry of Figure 3 the following can be defined

$$\begin{aligned} t_0 &= \frac{2Y}{c} & y &= \frac{ct_0}{2} \\ \tau_0 &= \frac{2r_0}{c} = \frac{2r}{c} & r_0 = r &= \frac{c\tau_0}{2} \end{aligned}$$

The various trigonometric quantities in equation (III-4) can now be expressed in terms of these as follows:

$$\begin{aligned} \sin \theta &= \frac{Y}{r_0} = \frac{t_0}{\tau_0} \\ \cos 2\theta &= 1 - 2 \sin^2 \theta = 1 - 2 \frac{t_0^2}{\tau_0^2} \end{aligned}$$

For  $r = r_0$  equation (II-23b) can be written as

$$Y = \operatorname{argcosh} (V)$$

$$\text{where } V = \left( \frac{1}{2} \frac{c^2 t^2}{r^2} - 1 \right) = \left( 2 \frac{t^2}{\tau_0^2} - 1 \right)$$

Using the half angle relations for hyperbolic functions

leads to

$$\cosh \frac{Y}{2} = \left( \frac{1}{2}(V+1) \right)^{1/2} = t/\tau_0$$

Similarly,

$$\begin{aligned} \sinh Y &= (V^2 - 1)^{1/2} \\ &= 2 \frac{t}{\tau_0^2} (t^2 - \tau_0^2)^{1/2} \end{aligned}$$

And finally, to within a factor of 2,

$$p(t) = - \frac{S \rho r}{2\pi^2 c^2} \left( \frac{t^2(\cos\theta + 1) - t_0^2}{t^2(t^2 - t_0^2)(t^2 - \tau_0^2)^{1/2}} \right) = - P_\delta R_0 \frac{2r}{\pi c^2} \left( \right) \quad (\text{III-15})$$

Letting  $P_\delta R_0$  be unity, as before, results in an expression for the diffracted pressure wave in the time domain which can be compared directly to the H-K result.

Biot-Tolstoy:

$$p(t)_{BT} = - \frac{2r}{\pi c^2} \left( \frac{t\tau(\cos\theta + 1) - t_0^2}{t(t^2 - t_0^2)(t^2 - \tau_0^2)^{1/2}} \right) \quad t > \tau_0 \quad (\text{III-16})$$

Helmholtz-Kirchhoff:

$$p(t)_{HK} = - \frac{2r}{\pi c^3} \left( \frac{r \sin 2\theta}{t(t^2 - t_0^2)(t^2 - \tau_0^2)^{1/2}} \right) \quad t > \tau_0 \quad (\text{III-17})$$

Equation (III-16) and (III-17) are similar in overall form but differ in several important ways. When  $\tau_0$  is much greater than  $t_0$ , the time dependence of both expression is determined by the  $(t^2 - \tau_0^2)^{-1/2}$  factor. (for  $t_0$  approaching  $\tau_0$ , the behavior is more complex and is treated in detail in Appendix A).

Since the impulse source has an infinite amplitude, the leading edge of the diffracted pressure signal ( $t = \tau_0$ ) must also be infinite. After this infinite leading edge, the time behavior can be described as follows:

$$\Delta t = t - \tau_0 \quad t^2 = \Delta t^2 + 2t\tau_0 - \tau_0^2$$

For the 'early diffracted signal,  $\Delta t \ll \tau_0$  and

$$(t^2 - \tau_0^2)^{1/2} \approx (2t\tau_0 - 2\tau_0^2)^{-1/2} = (2\tau_0(t - \tau_0))^{-1/2} = (2\tau_0 \Delta t)^{-1/2}$$

The initial diffracted time signal decays as  $\Delta t^{-\frac{1}{2}}$  for both solutions. Since the amplitude is highest in the early time portion of the signal, this  $\Delta t^{-\frac{1}{2}}$  dominates the Fourier transform of the signal and the frequency dependence of both solutions takes the form  $f^{-\frac{1}{2}}$  which is characteristic of many diffraction problems. As time increases, however, the H-K solution approaches the form  $t^{-\frac{1}{2}}$  while the B-T form approaches  $t^{-1}$ .

Both solutions have been implemented on the IBM computer system at NPS. The diffracted time signals for a representative geometry are shown in Figure 4. Care should be exercised in comparing the magnitude of the first point ( $t = 0$ ) since the "infinite" values here were handled differently in the two solutions. The approach used in the B-T computation is the numerical integration technique discussed earlier while the approach for the H-K results are taken directly from Clay and Medwin [Ref. 10].

The behavior of the two solutions as a function of  $\theta$  is also fundamentally different. Examination of the numerators of Equations (III-16) and (III-17) over the region of  $\theta$  from 0 to 180° (the problem of the thin plate being symmetrical with respect to 180°), reveals three apparent zero values for the H-K solution (0, 90°, 180°) vice two for B-T (90°, 180°). Actually, the zero in the numerator at 90° is offset, in the limit, by the term  $(t^2 - t_0^2)$  in the denominator which goes to infinity at  $t = t_0$ . Physically, this means that

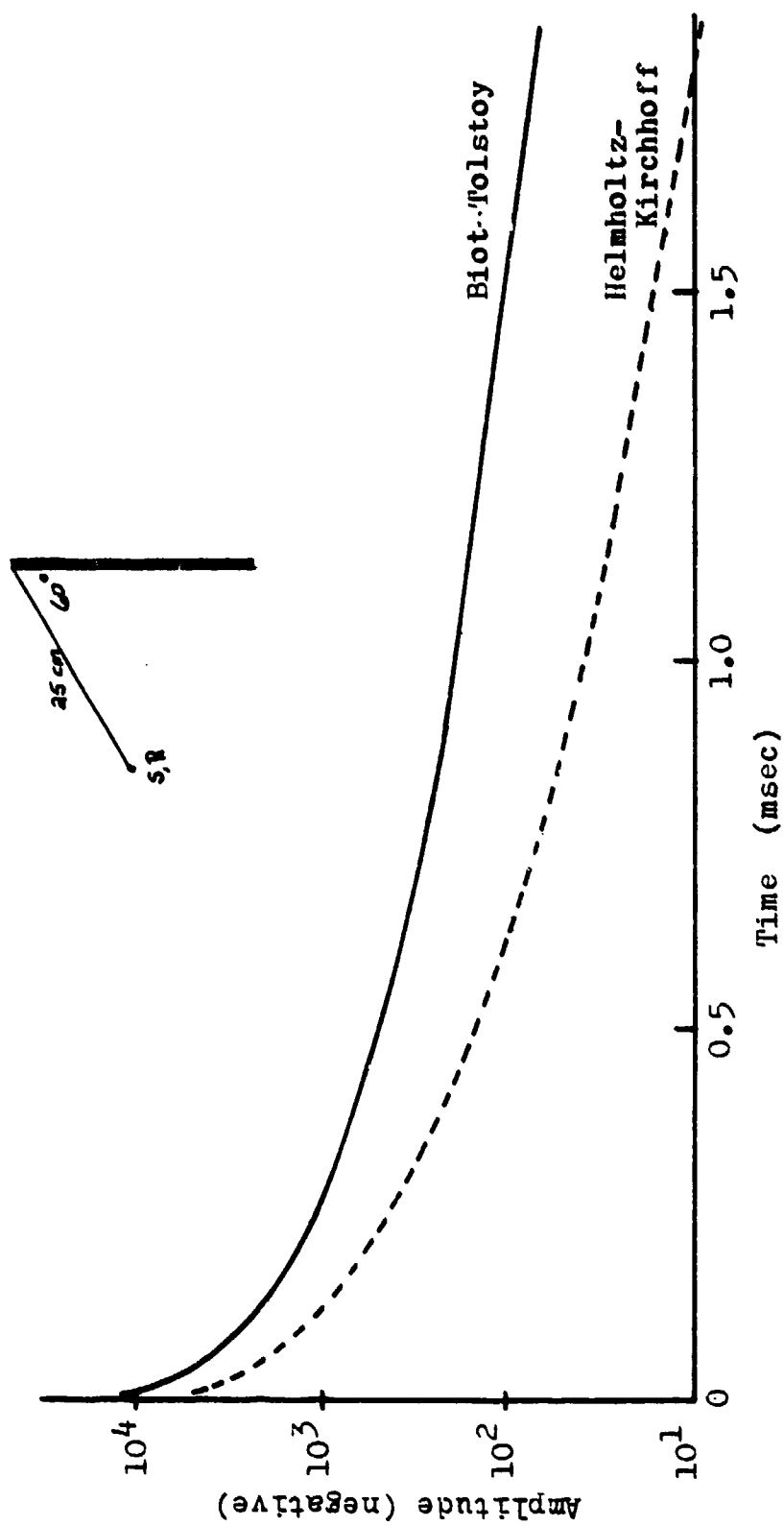


Figure 4. Comparison of Time Dependence of Biot-Tolstoy and Helmholtz-Kirchhoff Backscatter Solutions.

when source and receiver are directly over the edge, perpendicular to the plate, the solution consists of reflection only. In order to show the detailed  $\theta$  dependence, the time domain solution has been computed for a variety of geometries and each time solution transformed to the frequency domain. These results are plotted versus  $\theta$  for several frequencies in Figures 5 and 6. The amplitudes are in dB with the reference being twice the range from source to edge. The differences between the two solutions are significant, with the only region of agreement being near  $90^\circ$  where both solutions appear to approach the value of -6dB. This is the expected result and represents one half of the pressure amplitude that would result from reflection by an infinite plane. Actually, the H-K formulation produces the correct result at  $\theta = 90^\circ$  while the B-T solution appears to fail in the immediate vicinity of  $90^\circ$ . As  $\theta$  approaches  $90^\circ$ , the travel time of the reflection  $t_0$  approaches the travel time of the leading edge of the diffracted pulse  $\tau_0$ .

In this region, equivalent to approaching the shadow boundary in the forward scattering case, the B-T solution is approaching the delta function form and the approximation used to calculate the first time point may not be valid (see Appendix A). The B-T diffraction solution can only be used for  $\theta$  approaching  $90^\circ$  since at  $\theta = 90^\circ$  the separate reflection solution would apply (Equations II-18 and II-19).

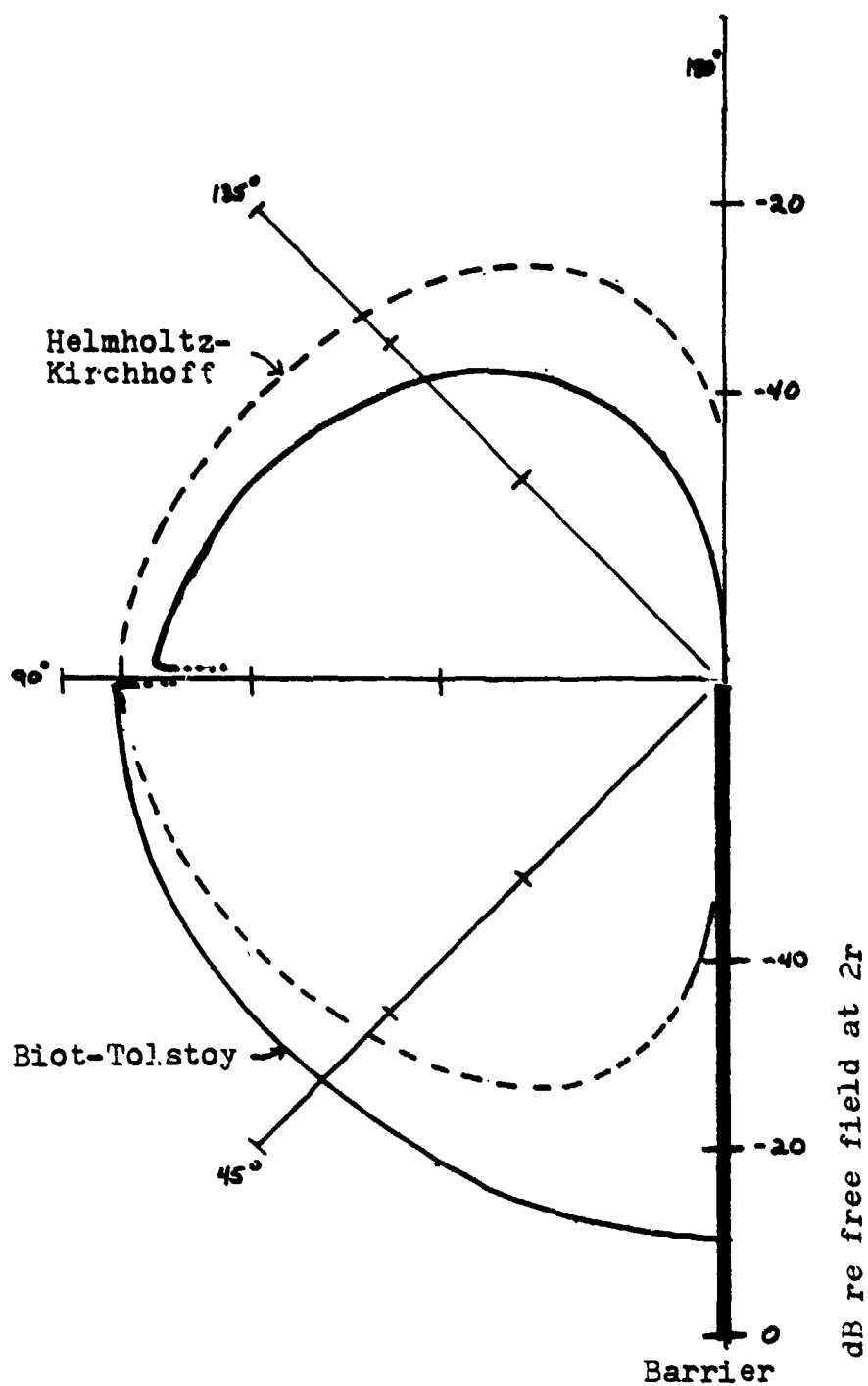


Figure 5. Comparison of B-T and H-K Backscatter Solutions as a Function of  $\theta$  at  $r=20$  cm and a Frequency of 781 Hz.



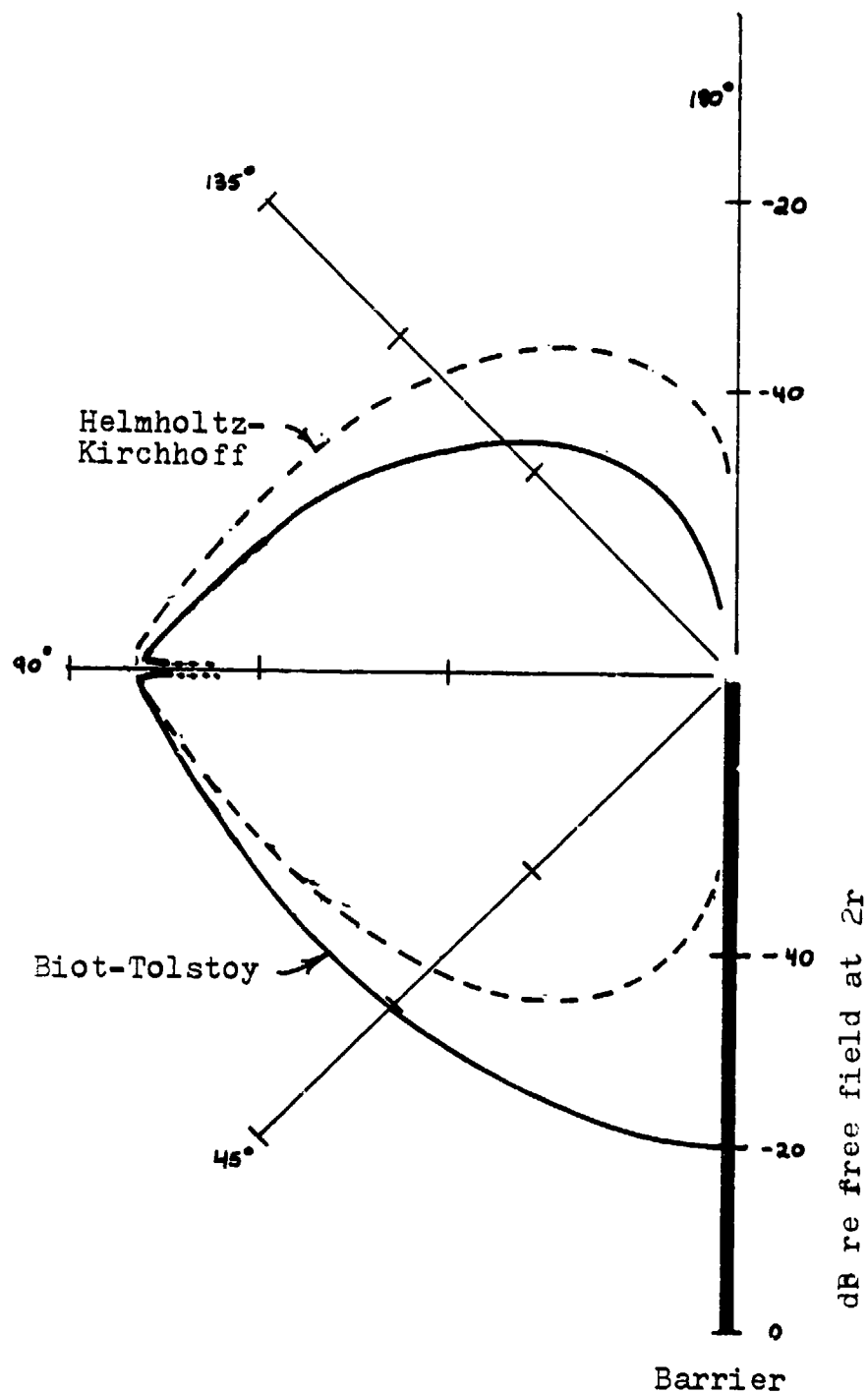


Figure 6. Comparison of B-T and H-K Backscatter Solutions as a Function of  $\Theta$  at  $r=20$  cm and a Frequency of 10,100 Hz.

As the source and receiver are moved away from  $90^\circ$  the disagreement between the solutions is dramatic. It is intuitively correct that both solutions go to zero as  $\theta$  approaches  $180^\circ$ , since the plate is infinitely thin and would not be "sensed" by a wave from this direction. The way in which the solutions approach this zero value is quite different.

The most significant disagreement between the solutions is seen when source and receiver are close to the plate ( $\theta$  approaching 0). The H-K solution approaches zero near the plate (it is symmetrical, except for sign, about  $90^\circ$  due to the  $\sin 2\theta$  term) while B-T approaches a constant value for each frequency. This zero in the H-K solution appears as a consequence of the simplifying assumption stated in Equation (II-26), where the total pressure field in the plane of the plate is assumed to be the value of the incoming wave field evaluated at that location ( $M = 1$  assumed). This "boundary condition" therefore forces the diffracted pressure field to be zero anywhere in the plane of the plate. It will be shown in the experimental portion of this paper that the B-T solution is correct in this region near the plate. Although not shown in Figures 5 and 6, both solutions exhibit the proper sign behavior, i.e., the direct and diffracted pulses are opposite in sign in the region 0 to  $90^\circ$  but have the same sign for  $90$  to  $180^\circ$ .

The summary, the B-T and H-K solutions simplified for the case of coincident source and receiver, are dramatically different. They approach agreement, in general, only in the region near, but not at,  $\theta = 90^\circ$ .

The final consideration before leaving the topic of backscatter is an examination of the form of the B-T solution. Multiplying out the numerator and regrouping terms, Equation (III-16) can be written as

$$p_d(t)_{BT} = - \frac{2r}{\pi c^2} \left( \frac{\cos \theta}{(t^2 - t_0^2)(t^2 - \tau_0^2)^{1/2}} + \frac{1}{t^2(t^2 - \tau_0^2)^{1/2}} \right) t > \tau_0 \quad (\text{III-18})$$

When written in this way, the solution is seen to have an interesting characteristic. The solution is the sum of two terms, one which takes into account the overall geometry of source/receiver and plate (the first term in III-18) and a term which depends on the distance from the edge of the plate to the source/receiver. This seems to be a characteristic of exact solutions of the problem of diffraction by a half-plane and is directly related to the "image in the barrier" first mentioned by Macdonald [Ref. 3]. This "image" approach will be discussed in some detail in the next section.

#### B. BIOT-TOLSTOY AND MACDONALD

In comparing the B-T and Macdonald half-plane diffraction solutions, an approach similar to that of the previous section will be used. However, the solutions will not be limited to backscatter but will be kept general and the emphasis will

be on "forward scatter", i.e., diffraction of sound into the geometric shadow region (source and receiver on opposite sides of the half-plane). The purpose of the comparison is twofold: to show that computations based on the two "exact" solutions, one impulse and one CW do, in fact, produce the same results, and to gain some insight into the use of the "image in the barrier". As discussed in section II, the Macdonald's solution form and computations are from Kawai's excellent paper [Ref. 11].

The comparison between B-T and Macdonald computational results requires some manipulation of geometric quantities. Kawai's results are converted to the notation of this paper for consistency, however, this results in only 2-3 points per frequency spectrum. To alleviate this problem somewhat, the geometry is selected in such a way that several different B-T runs result in basically the same values. Figure 7 shows this geometry and the comparison between B-T and Macdonald results. The reference pressure is the free-field pressure that would be measured at a distance of  $r + r_0$  from the source with the plate removed. Data referenced in this manner are labeled "dB re free field at 2r". This combination of geometry and reference results in B-T theoretical values which vary only one dB over the range  $\theta = 330^\circ$  to  $\theta = 360^\circ$ . Kawai's computations are then converted from his normalized presentation [Ref. 11, Figure 3] to the format of Figure 6 in  $5^\circ$  increments of  $\theta$  between  $330^\circ$  and  $360^\circ$  inclusive and

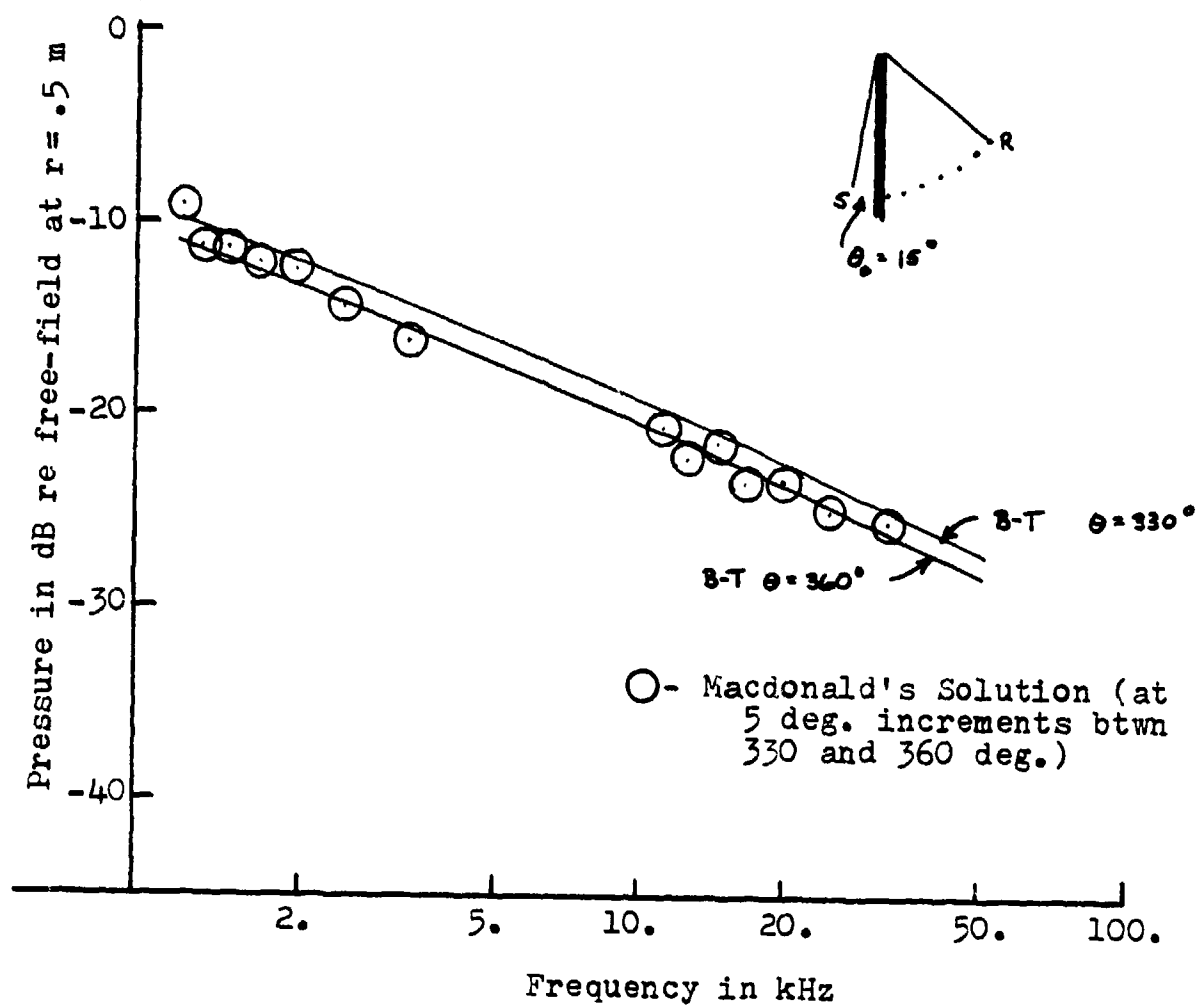


Figure 7. Comparison of B-T and Macdonald's Forward Diffraction solutions for Various  $\theta$ 's at  $r = 25 \text{ cm}$  as a Function of Frequency.

plotted in Figure 7 as discrete points. The agreement between the two solutions is seen to be very good. The scatter in the Kawai points is almost certainly attributable to the process of reading these values from the graphs of Ref. 11. Additional comparisons were made over a wide range of different geometries using the B-T theoretical results of Bremhorst [Ref. 12] with agreement similar to that shown in Figure 7 observed in all cases.

It should be noted, however, that the comparisons were not made for the general case of high frequency, large range, near the shadow boundary ( $R_N$  large and  $N$  small in the presentation of Kawai).

Kawai [Ref. 11] actually presents two sets of computations of Macdonald's theory; one for the "real" source only (referred to as  $ATT_0$ ) and one for the "real" plus "image" source (ATT). This terminology appears to be traceable directly to Macdonald [Ref. 3]. In his solution he separates a complex integral [Ref. 3, p. 422] into two integrals, performs the integrations separately, and recombines the two into an overall solution for velocity potential [Ref. 3, p. 425]. Bowman and Senior's approximate form of this overall solution [Ref. 1]] is given as equations (II-29), (II-30), and (II-31). The comparison of B-T and Macdonald in Figure 7, is based on Macdonald's complete solution, ATT. Indeed, if the complete solution of the half-plane problem is the sum of these two terms, it is not clear why one would want to consider them

separately. Yet this is precisely what is done by many authors in the noise reduction field [cf. Ref. 5].

In order to examine the "real" and "image" terms in MacDonald's solution more closely, equations (II-30) and (II-31) are repeated here with a slight change in the way  $\theta$  and  $\theta_0$  are expressed;

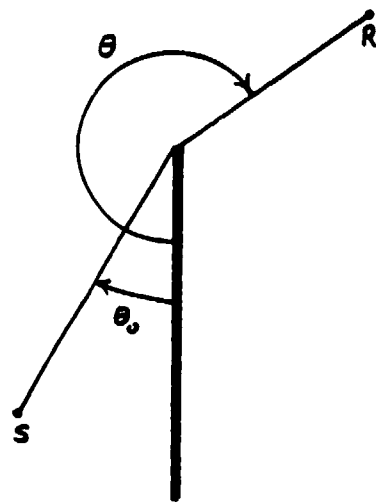
$$T_R = \text{sgn}(\pi - (\theta - \theta_0))(kR_1 - kR)^{1/2} \quad (\text{II-30a})$$

$$T_{R'} = \text{sgn}(\pi - (\theta + \theta_0))(kR_1 - kR')^{1/2} \quad (\text{II-30b})$$

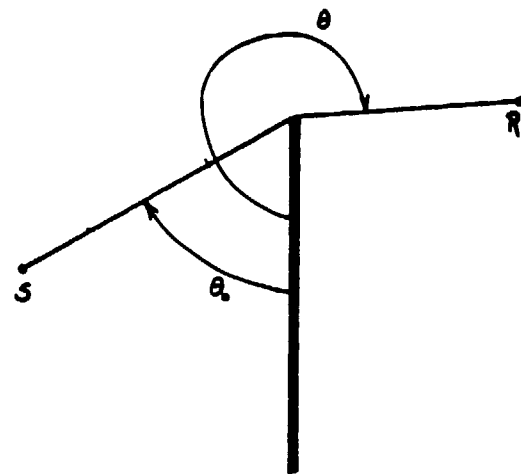
$$R = (r^2 + r_0^2 + z^2 - 2rr_0 \cos(\theta - \theta_0))^{1/2} \quad (\text{II-31a})$$

$$R' = (r^2 + r_0^2 + z^2 - 2rr_0 \cos(\theta + \theta_0))^{1/2} \quad (\text{II-31b})$$

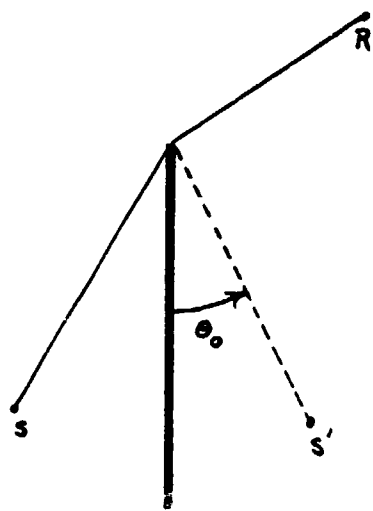
The primed values represent the "image" source terms. The real source terms are a function of the difference between  $\theta$  and  $\theta_0$  while the "image" terms are a function of their sum. The significance of this is shown graphically in Figure 8. Figures 8(a) and 8(b) show two different geometries, both of which have the same value of the quantity  $\theta - \theta_0$ . Since  $(\theta - \theta_0)$  is only form in which the quantities  $\theta$  and  $\theta_0$  enter real source portion of the solution, it is easily seen that the real source solution is independent of the orientation of the plate. It depends only on the locations of source and receiver relative to the edge. However, the geometries of Figures 8(a) and 8(b) are different in terms of  $(\theta + \theta_0)$ . It is this term which retains the information concerning the orientation of the plate (half-plane) relative to source and



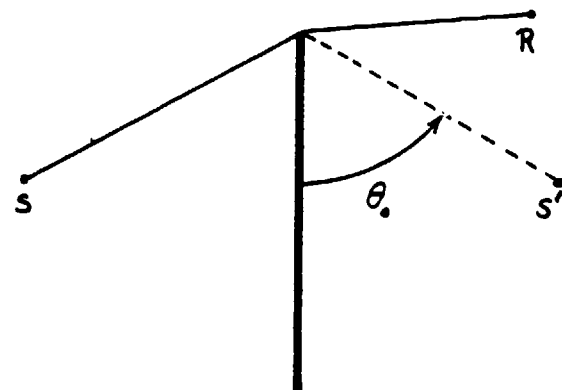
(a)



(b)



(c)



(d)

Figure 8. Geometry of the Image of the Source in the Barrier.



receiver. Since changing the sign of  $\theta_0$  is the same, geometrically, as moving the source to the opposite side of the barrier, one can easily see why the second term of the solution is associated with the "image of the source in the barrier". This interpretation is shown in Figures 8(c) and 8(d).

This interpretation is not unique to Macdonald's solution. Recalling equation (III-18), it was shown that the B-T solution, for the case of coincident source and receiver, could be written as the sum of two terms, one which depended only on the orientation of the edge and one which also considered the location of the plate. Indeed, the general form of the B-T solution given by equation (II-24) could be written as the sum of a term that is a function of  $\theta - \theta_0$  and another that is a function of  $\theta + \theta_0$ . This would be done in the following way:

$$\begin{aligned}
 p(t) &= p(t, \theta_0) + p(t, -\theta_0) \\
 &= -\frac{S\rho c}{4\pi\theta_w} (rr_0 \sinh Y)^{-1} e^{-\frac{\pi Y}{\theta_w} \{\beta_{\theta_0} + \beta_{-\theta_0}\}} \\
 \beta_{\theta_0} &= \frac{\sin \frac{\pi}{\theta_w} [\pi \pm (\theta - \theta_0)]}{1 - 2 \exp\left(\frac{\pi Y}{\theta_w}\right) \cos \frac{\pi}{\theta_w} [\pi \pm (\theta - \theta_0)] + \exp\left(-\frac{2\pi Y}{\theta_w}\right)} \\
 \beta_{-\theta_0} &= \frac{\sin \frac{\pi}{\theta_w} [\pi \pm (\theta + \theta_0)]}{1 - 2 \exp\left(\frac{\pi Y}{\theta_w}\right) \cos \frac{\pi}{\theta_w} [\pi \pm (\theta + \theta_0)] + \exp\left(-\frac{2\pi Y}{\theta_w}\right)}
 \end{aligned}$$

where each  $\beta$  term is actually the sum of two terms, one with the term in brackets evaluated using the (+) sign and the other using the (-) sign. There appears to be no advantage to writing the B-T solution in this way except to show the geometrical similarity to Macdonald's result. Indeed, Biot and Tolstoy specifically identify both terms as diffraction not reflection. True reflections have separately been identified by B-T as occurring before the diffraction; an interpretation that is direct and obvious in their impulse solution, but which is obscured in Macdonald's CW solution.

In summary, the B-T and Macdonald exact solutions have been found to be in very close agreement for all of the cases examined. Real and image sources have been shown to be a valid, if not particularly useful, interpretation of both solutions.

#### IV. EXPERIMENTAL APPROACH

##### A. GENERAL

The measurements reported herein were made in the NPS anechoic chamber utilizing pulse techniques. The anechoic chamber provided the low noise, low reverberation environment necessary to make precise amplitude measurements at low source levels. The use of a pulsed source provided a signal that was both wideband and deterministic and made it possible to control the effects of extraneous scattering by judicious choice of the sampling window. Detailed descriptions of the anechoic chamber and the data acquisition hardware may be found in Reference 12, and will not be repeated here, except when necessary to explain the results.

##### B. DATA ACQUISITION

A block diagram of the overall experimental data acquisition process is shown in Figure 9. Overall timing of the acquisition process is controlled by the programmable timing simulator. A typical sequence is as follows. The waveform generator is triggered by the timing simulator, sending a single replica of the preprogrammed pulse to the power amplifier. This pulse is amplified to approximately 50 volts peak, added to the 150 volt D.C. bias voltage, and applied to the source (source and receiver characteristics will be

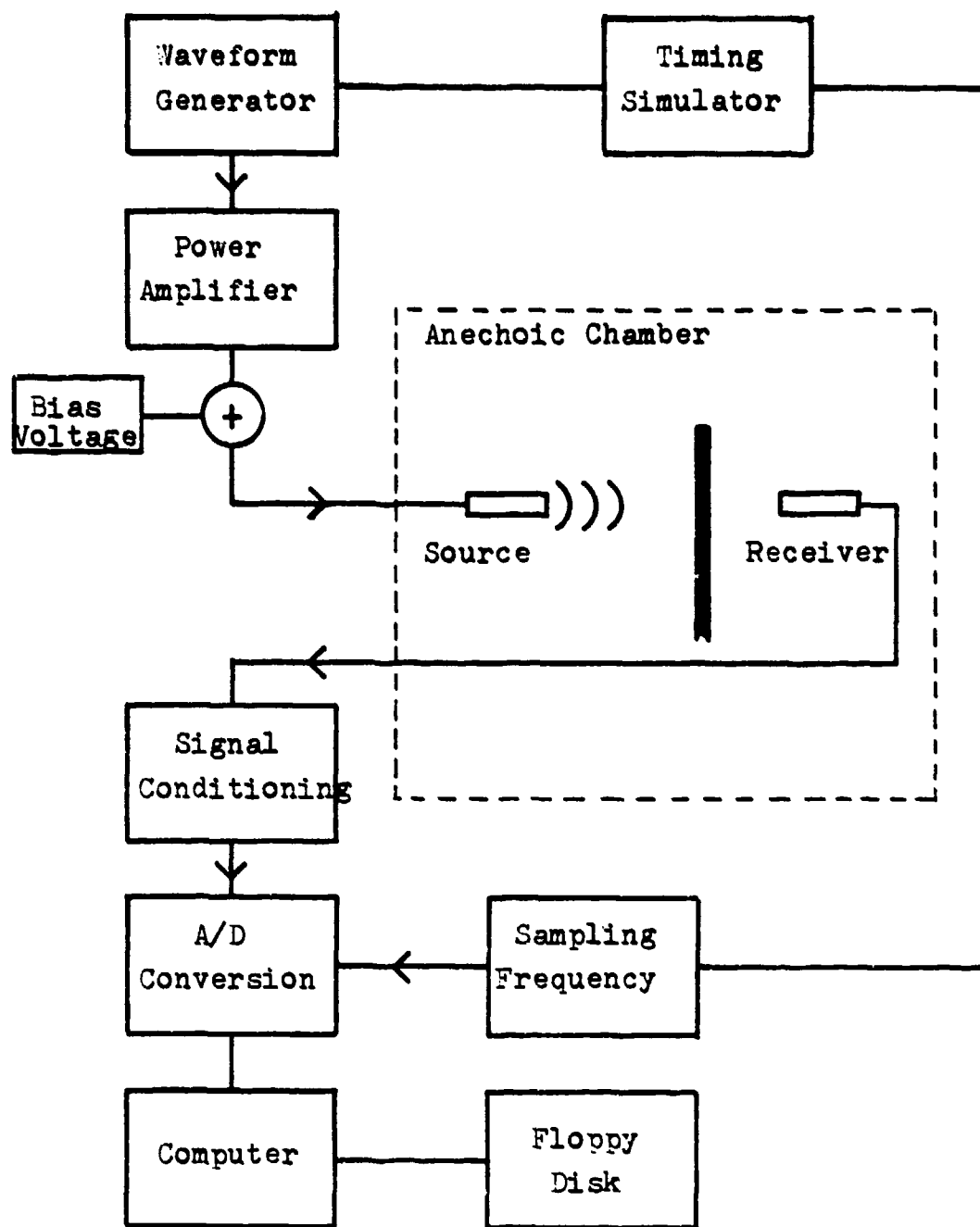


Figure 9. Experimental Data Acquisition General Block Diagram.

discussed separately). The transmitted signal is received by the  $\frac{1}{4}$  inch condenser microphone (B+K 4133) and sent to the signal conditioning equipment. Here the signal is amplified, filtered to remove low frequency noise and to prevent aliasing in the sampling process, further amplified and digitized (12 bits). Here the timing simulator determines the start time and duration of the sampling of each pulse. By selecting the sampling frequency and duration, the number of samples available to the FFT can be determined. In practice, the number of samples is set slightly higher than the number to be transformed since the computer begins with the first sample and disregards those coming after the specified number have been acquired. This process is repeated for each pulse with a pause of approximately 80 milliseconds between pulses.

The computer accumulates the samples by averaging up to 10,000 samples in the time domain and then computes the Fourier transform of this averaged waveform using a standard software FFT algorithm. Since the FFT must be taken only once, the system runs in real-time, which allows a very large number of pulses to be averaged in a reasonable amount of time. Since this averaging is coherent, the signal-to-noise ratio is proportional to  $N$ , the number of pulses, rather than the usual  $N^{\frac{1}{2}}$ . The averaged time waveform or FFT results are stored on a floppy disk for later use.

### C. SOUND SOURCE

The ideal sound source for these experiments would be a point source capable of high acoustic output over very short time durations, with zero output at all other times. These characteristics can only be approached with a real source. The obvious choice of a spark source is rejected in order to avoid finite amplitude effects. Fortunately, the extremely low noise levels of the anechoic chamber plus coherent averaging makes accurate measurements possible with a source of relatively low intensity. The search for a useful source of small dimensions and narrow time response has been a continuing one at NPS [cf. Ref. 14]. The source chosen for the experimental work in this paper were the B & K  $\frac{1}{2}$  inch and 1 inch condenser microphones. The use of these microphones as sound sources is described in Reference 12 and in a B & K technical pamphlet [Ref. 15]. In general, the  $\frac{1}{2}$  inch source covered the higher frequencies (6-40. kHz) while the 1 inch source was used to provide additional low frequency coverage (down to approximately 1.5 kHz). The 1 inch source is actually capable of providing sufficient output over the entire frequency range but directivity does become significant at the higher frequencies.

Typical source waveform and frequency spectra are shown in Figures 10 through 13. In Figure 10, the waveform at the output of the power amplifier is the top curve with the received waveform shown below. The received waveform (and

Source -  $\frac{1}{2}$ " B-K

Receiver -  $\frac{1}{2}$ " B-K

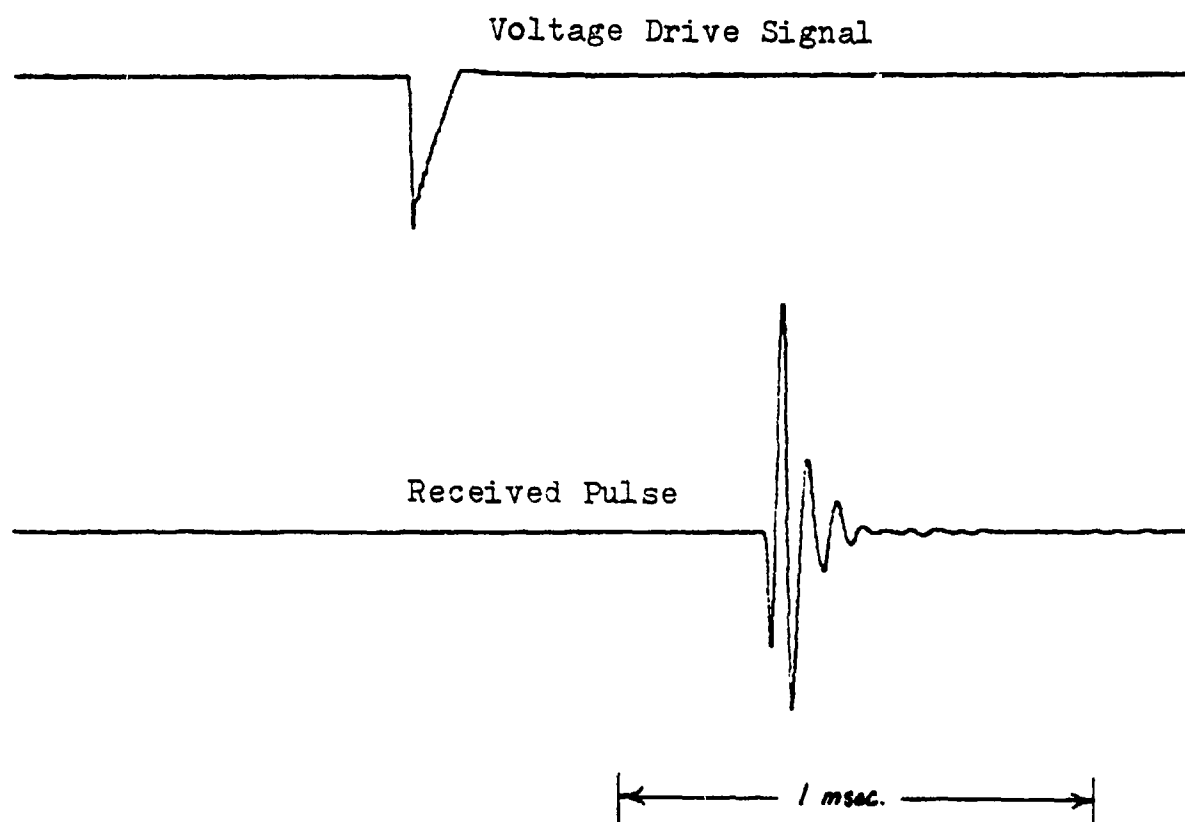


Figure 10. Typical Time Domain Signal,  $\frac{1}{2}$ " Source.

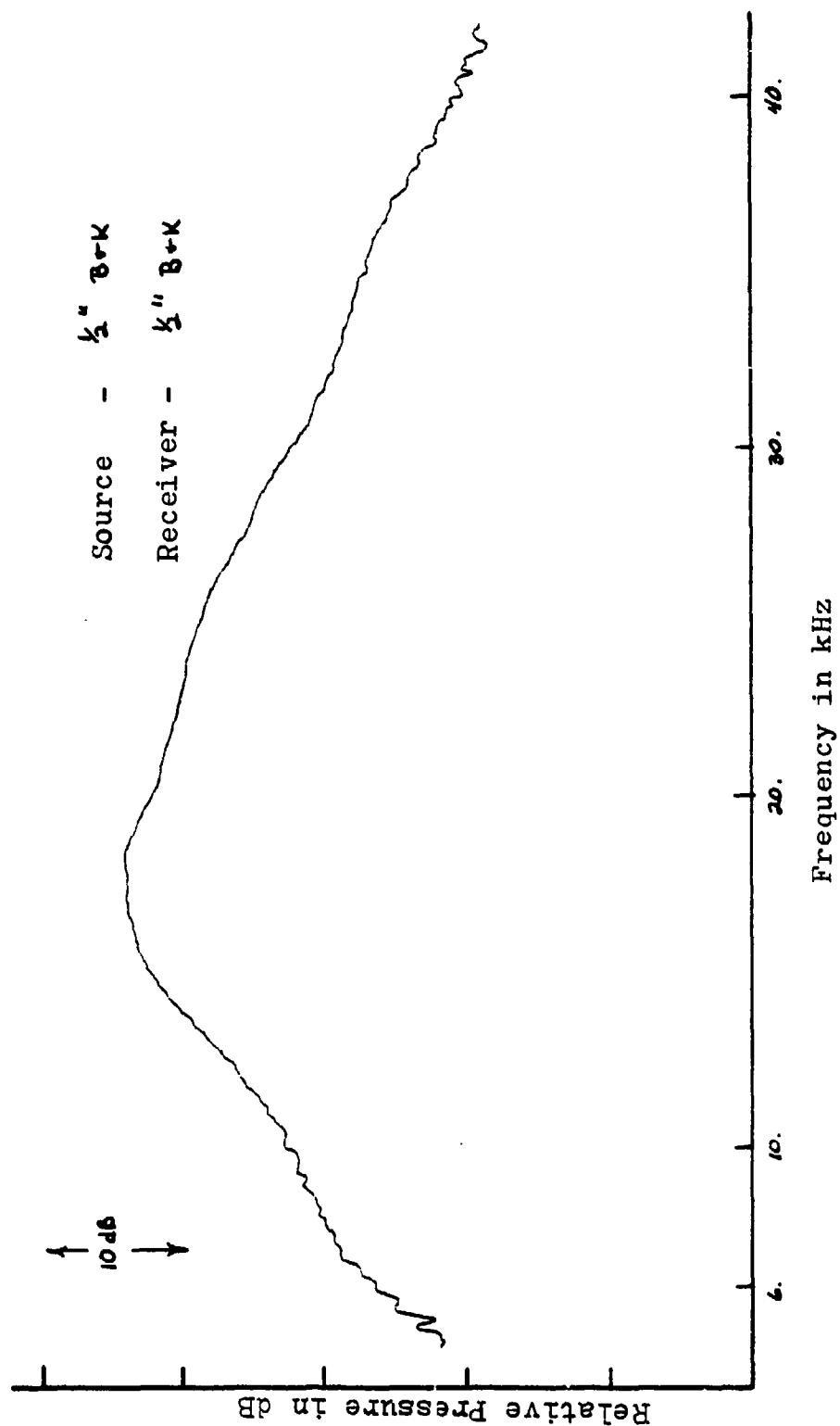


Figure 11. Typical Frequency Spectrum of Acoustic Pulse,  $\frac{1}{2}$ " Source.



Source - 1" B+k

Receiver - 1/2" B+k

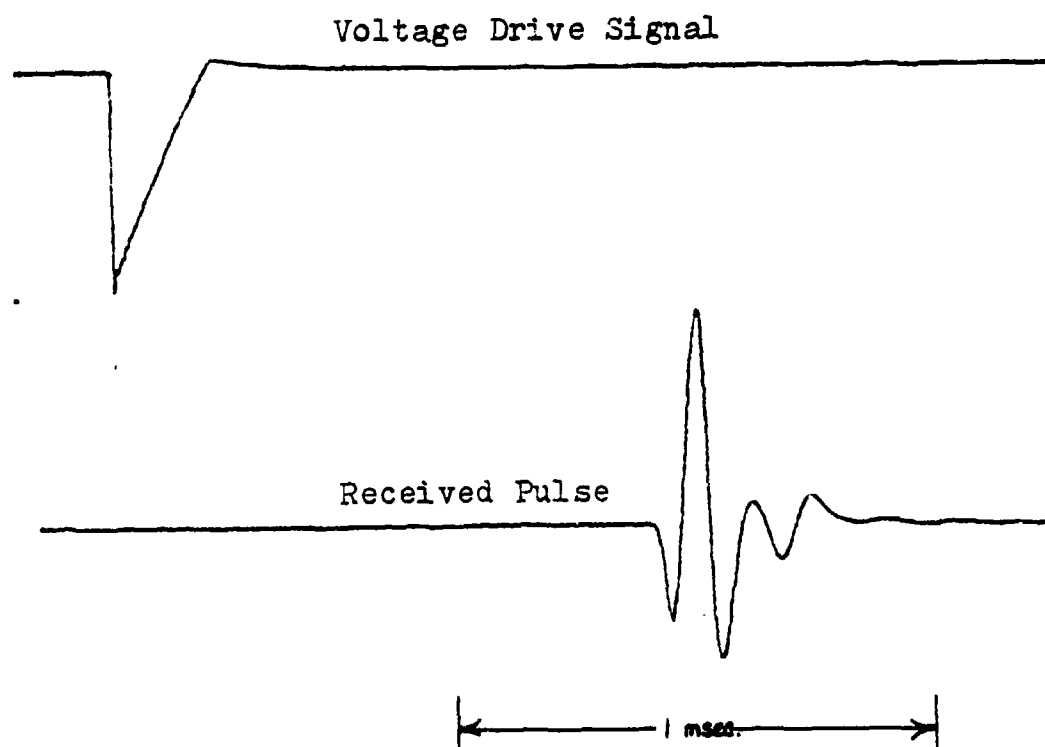


Figure 12. Typical Time Domain Signal, 1" Source.

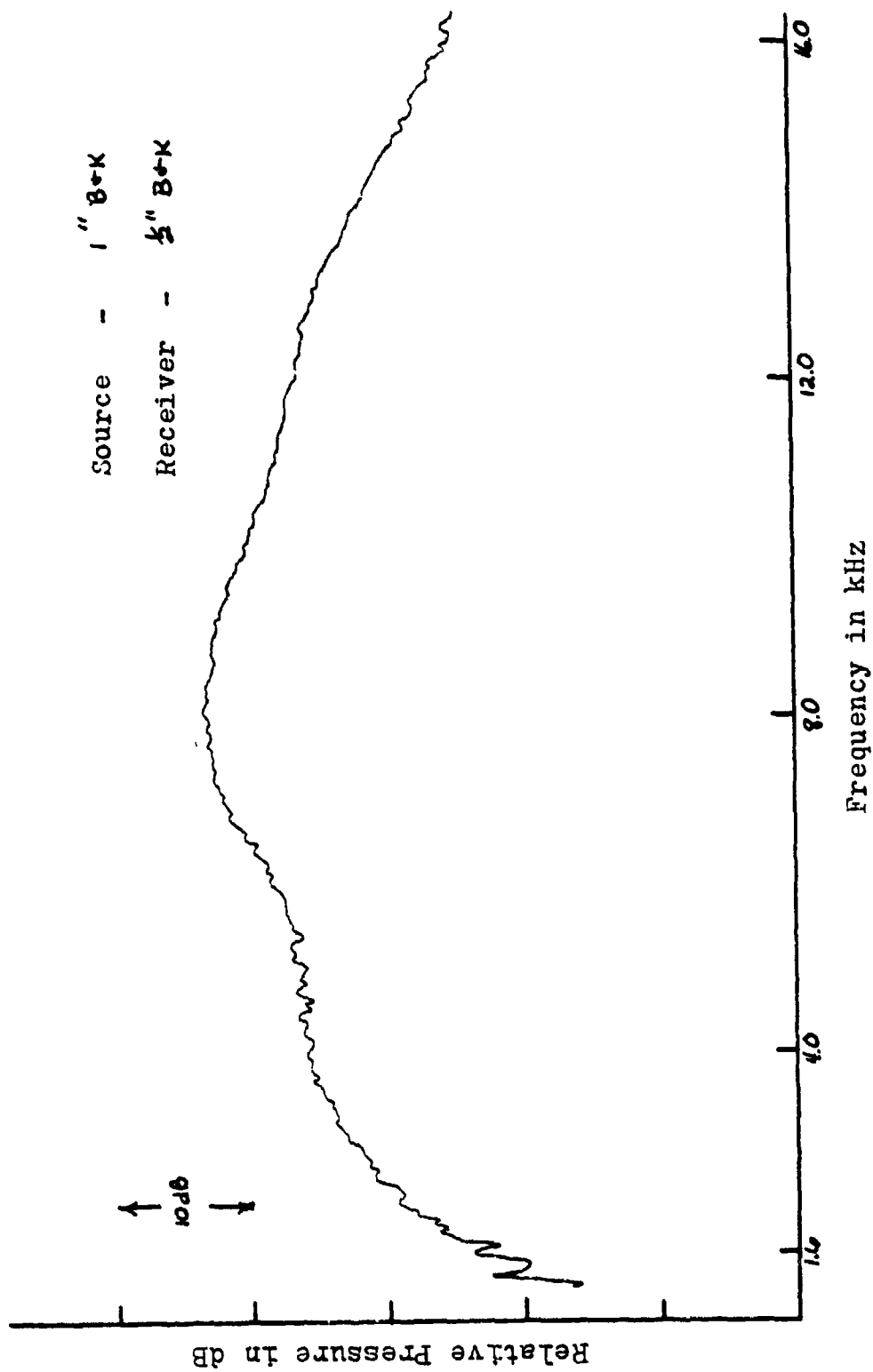


Figure 13. Typical Frequency Spectrum of Received Pulse, 1" Source.

associated frequency spectrum) is actually due to a combination of source and receiver response, however, the relative contributions of each are not particularly important since all results are normalized by an appropriate reference measurement using the same source and receiver. The time duration (or "ringing") of the pulse is important since all of the desired diffracted pulse must be sampled before the unwanted arrivals from the other edges of plate. The longer the acoustic pulse, the larger the specimen must be to separate the pulses. This ringing is especially important in measuring backscatter since the low amplitude diffracted pulse will arrive after the direct/reflected pulse which is much higher in amplitude. Figure 11 shows the energy spectral density of acoustic pulse in Figure 10.

Figures 12 and 13 present the same data as Figures 10 and 11, with the same receiver, but using the 1 inch source. In this case, the received pulse was low pass filtered at 14 kHz in order to enhance the low frequency portion of the spectrum.

Once an acceptable source and receiver were selected, a mounting system had to be devised which allowed the microphones to be positioned accurately yet present a minimum of additional scattering surface. The approach used is shown in Figure 14. The diffracting object (in this case a thick plate) was suspended with nylon fishing line from a frame attached to the ceiling of the anechoic chamber. Heavier

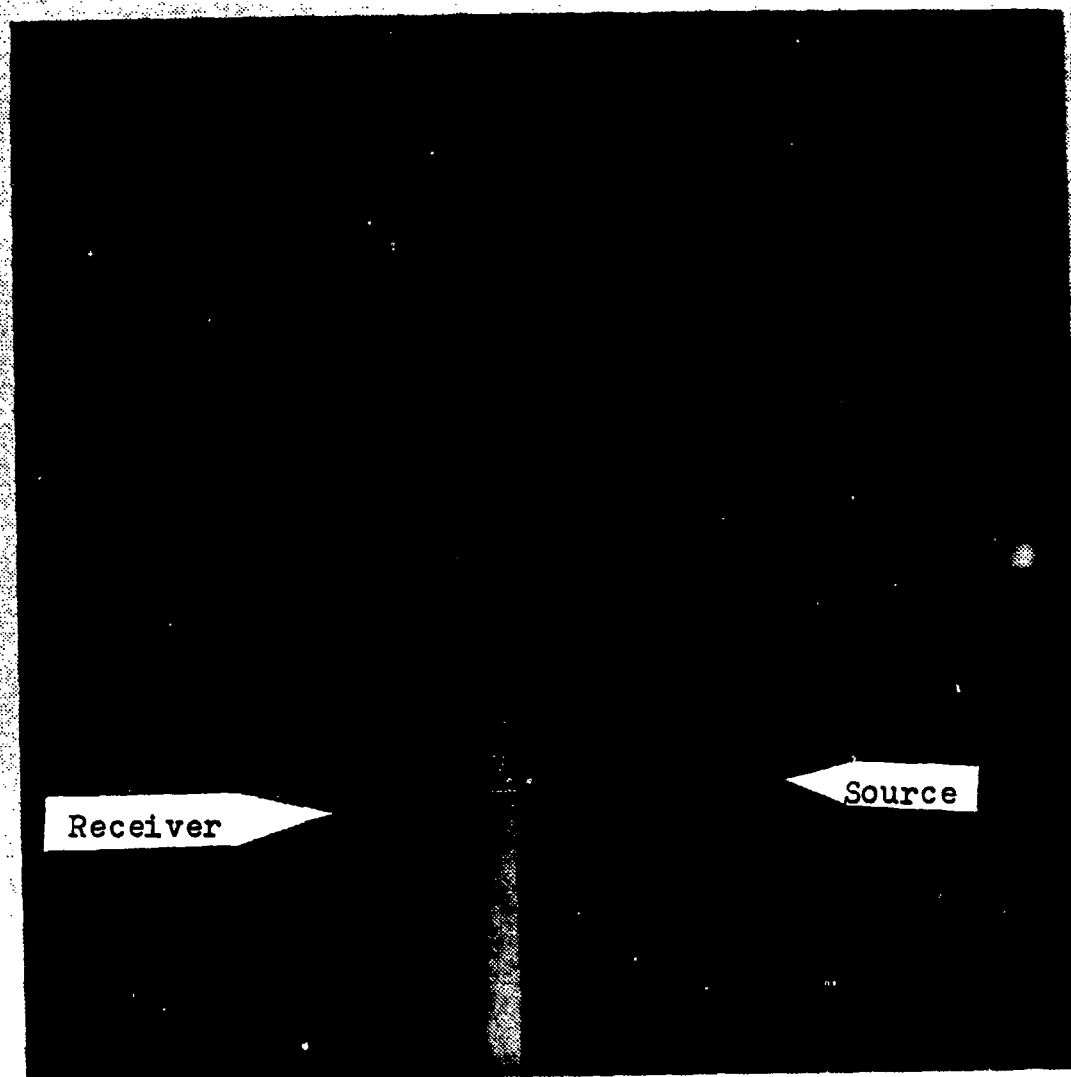


Figure 14. Typical Anechoic Chamber Measurement Apparatus.

objects were also supported from below. The source and receiver were each attached to a pair of thin stainless steel wires mounted firmly to the ceiling frame and resiliently to the wire mesh floor of the chamber. Source and receiver were positioned in the horizontal by moving the ceiling and floor attachments and vertically by moving up or down the wires. Additional support of the signal cables was provided, as necessary, with nylon line from the ceiling frame.

#### D. PLATE CONSIDERATIONS

The plate used in the experiment should be as thin and yet, as rigid and non-transparent as possible. In addition, it was desirable to keep the overall weight of the plate low to facilitate handling and suspension within the anechoic chamber. Aluminum plate .475 cm thick was chosen as a reasonable compromise. The transmission loss, calculated using the approach of Reference 12, was greater than 40 dB at 1.5 kHz, increasing with frequency. This was considered adequate since no thin plate measurements were planned where the direct path through the plate was to be substantially less than the diffracted path. For the thick plate tests the direct path would be short but two plates would be used and the resulting attenuation would certainly be adequate. These estimates were verified by examining the received signal prior to the arrival of the first diffraction to ensure there was no significant direct path arrival.

## V. BACKSCATTER EXPERIMENTAL RESULTS

In Figures 5 and 6 it was shown that the B-T and H-K solutions give dramatically different results for backscatter near the surface of the rigid half-plane. A simple experiment was performed to determine which solution is correct. The one inch B+K microphone was used as the source with the one-half inch B+K microphone used as the receiver. They were taped together and positioned at a distance of 25 cm from the edge at various angles as shown in Figure 15. Although the source and receiver acoustic centers are separated by approximately 2.5 cm they will be assumed to be coincident.

The transmitted waveform was the half triangle discussed earlier but the received signal was low pass filtered at 60. kHz vice the 14. kHz shown in Figures 12 and 13, to achieve a higher frequency response. Each transmitted pulse actually resulted in three received pulses. The first pulse, which arrived almost immediately, was the direct source/receiver path. The second was the reflection from the plate. while the third was the desired diffraction from the edge. Unfortunately, the first two pulses were considerably higher in amplitude than the diffracted pulse. Even with the ability to exclude the first two pulses in the time domain, the ringing of the reflected pulse interfered with the analysis of the diffracted pulse. This limited the geometry to

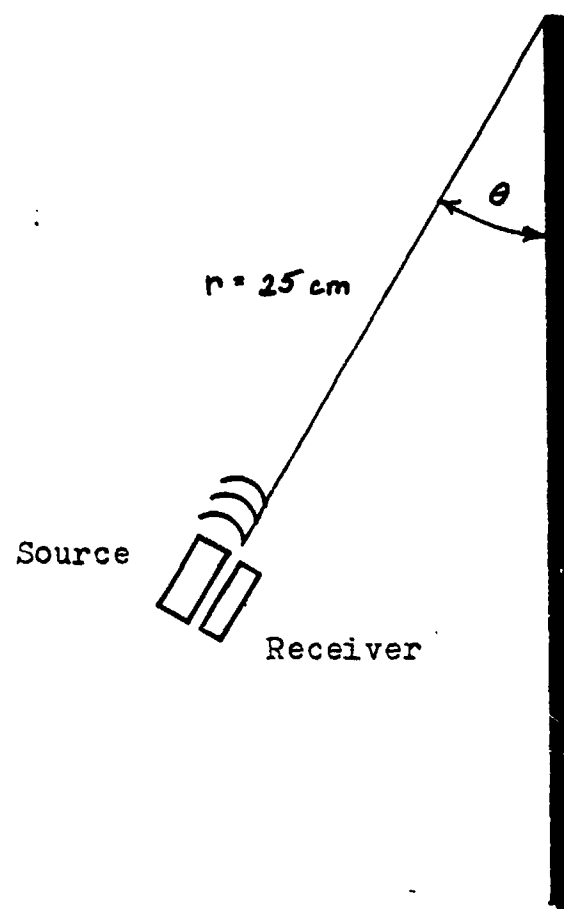


Figure 15. Backscatter Experimental Geometry.

source/receiver locations near the plate, which presented no particular problem since this was the region of most interest anyway.

The results of this experiment are presented in Figure 16, with the free-field pressure at  $2r$  used as the reference. For the comparison, the theoretical B-T and H-K results are shown for angles approximating those of the measurements. (These theoretical results are the same as those presented in Figures 5 and 6, now plotted as a function of frequency for specific angles.) The B-T theoretical results are plotted as a single line since they vary by less than one dB over the range of angles presented. It is clear that the measured data tend to agree with the results predicted by the B-T solution rather than going to zero at the surface of the plate as in the H-K solution. The considerable scatter in the measured data, especially near 9 kHz at 30 degrees, is attributable to interference between the diffraction pulse and the ringing of the reflected pulse.

The measured data not only favor the B-T solution but also confirm the presence of a scattered wave near the surface. If this scattered wave also exists on the surface, as predicted by B-T, (there is no reason to think otherwise) it points out a serious fallacy in the Kirchhoff assumption. In order to evaluate the integral in Equation II-25, the wave field at all points on the surface of integration had to be known. This was accomplished, through the Kirchhoff



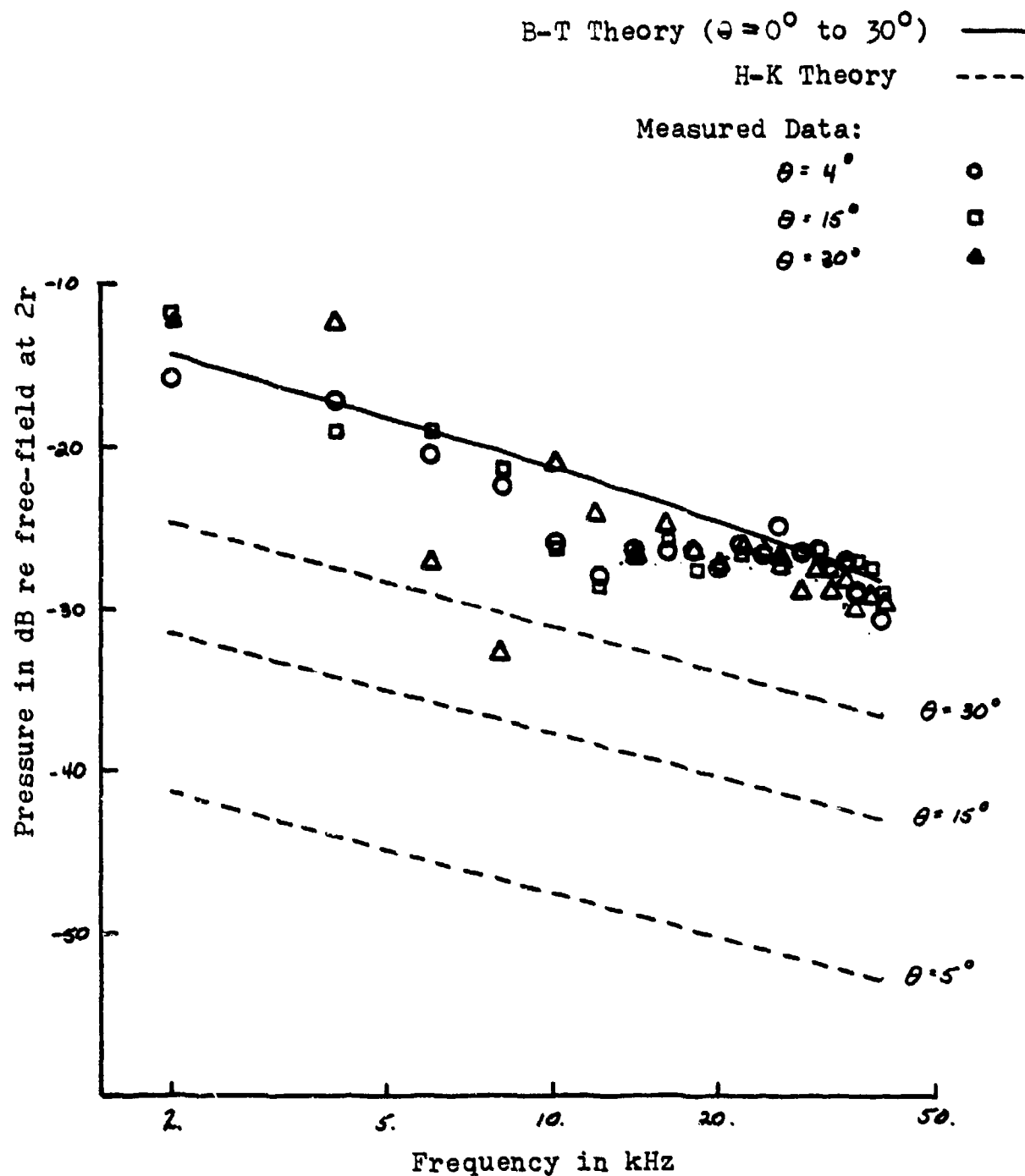


Figure 16. Comparison of Measured Backscatter from a Half-plane with Theoretical B-T and H-K Solutions for  $r = 25$  cm at various  $\theta$ 's ( $\theta = \theta_0$ )

assumption, by simply taking the wave field on the surface to be the reflection of the incoming wave. This is equivalent to a boundary condition which forces the diffracted wave field due to the edge to zero at the surface of the plate. When the solution is transformed to the time domain (Equations III-6 and III-7) where the diffracted and reflected terms are considered separately, the diffracted term must go to zero at  $\theta = 0^\circ$  in order to satisfy the imposed boundary condition. That this is clearly not the case indicates that the H-K formulation should not be used to estimate the backscattered wave field near the surface of the plate. For forward scattering, the H-K diffraction solution would also be expected to go to zero near the plate. Since Bremhorst's data [Ref. 12] show the presence of a forward scattered wave at the surface, the above argument can probably be applied to this case as well.

## VI. FINITE PLATE FORWARD SCATTERING EXPERIMENTAL RESULTS

### A. GENERAL

When a rigorous diffraction solution such as Biot-Tolstoy is applied to the problem of diffraction by a real object, one must be careful to ensure that the original boundary conditions are applicable. For a finite barrier, two important considerations are whether the barrier is large enough to be considered infinite in extent and thin enough to ignore thickness (the double edge). Since the geometry of the half-plane diffraction problem is such that everything is described in terms of a cylindrical coordinate system with the origin at the edge, there is a tendency to think of diffraction as simply an edge effect. This is the interpretation of the H-K boundary diffraction wave. This is also the simplest interpretation of a time domain, impulse solution such as B-T, where it is easy to visualize an expanding spherical wavefront intersecting the edge and reradiating acoustic energy as it "propagates" along the edge. If this were generally true, one could solve any diffraction problem by describing the diffracting object in terms of a series of edges (or, more appropriately, wedges) and adding their contributions. The problem with this approach is that the original solution assumed the presence of a rigid surface at some angles  $\theta = 0$  and  $\theta = \theta_w$  extending to infinity in the

radial and axial directions and an infinite fluid elsewhere (see Figure 1). When the physical situation approximates this condition, the diffraction problem can generally be treated by considering a source at the edge. For an extreme example where this is not true, one could consider the difference between the diffraction due to a rigid half-plane and that due to a large plate shrunk to become a thin wire at the location of the edge.

A related problem concerns the treatment of barrier corners. Here the barrier may be "high" enough to consider the radial dimension to be infinite but its width (the axial, or  $z$ , dimension) is finite. A roadside billboard or a tall building could be described this way. If the ground is totally absorbant (no reflections) Medwin [Ref. 8] treats the diffraction from this type of a barrier by adding the impulse response of each of the three edges, truncating the solution for each edge when the wave reaches the corner, to obtain the total time domain solution. The assumption implicit here too is that the boundary conditions of the theoretical B-T solution are sufficiently well approximated by the actual barrier.

The third major difference between the theoretical B-T solution and the actual barrier is the double edge caused by the finite thickness. The theoretical solution is based on a rigid, infinitely thin screen whereas the actual barrier is often approximately rigid but of finite thickness.

Some researchers have minimized this problem in their measurements by placing a "knife edge" at the top of the barrier [cf. Kawai, Ref. 11] but this introduces additional sources of diffraction where the face of the barrier changes angle. In any case, the real barrier will always have some finite thickness dimension and it is desirable to be able to calculate or at least understand the nature of its effect on the diffracted field.

A series of experiments was performed in order to define these "finite barrier" effects.

#### B. FORWARD DIFFRACTION AT A CORNER

Bremhorst [Ref. 12] showed excellent agreement over a wide frequency range between the B-T infinite plate solution and pulse measurements on a 3/16" thick plate, provided the pulse is sampled in such a way as to exclude late arriving diffracted pulses from other edges. However, discrepancies between measurements and theory of 5-10 dB were observed at frequencies approaching 50 kHz with source and receiver near the plate. The purpose of this experiment was to measure the diffracted pressure field in the vicinity of the corner of a plate and compare it to the field predicted by B-T using Medwin's truncation approach. The present geometry was chosen to ensure that only the edges intersecting at the corner of interest would contribute to the measurements (Figure 17).

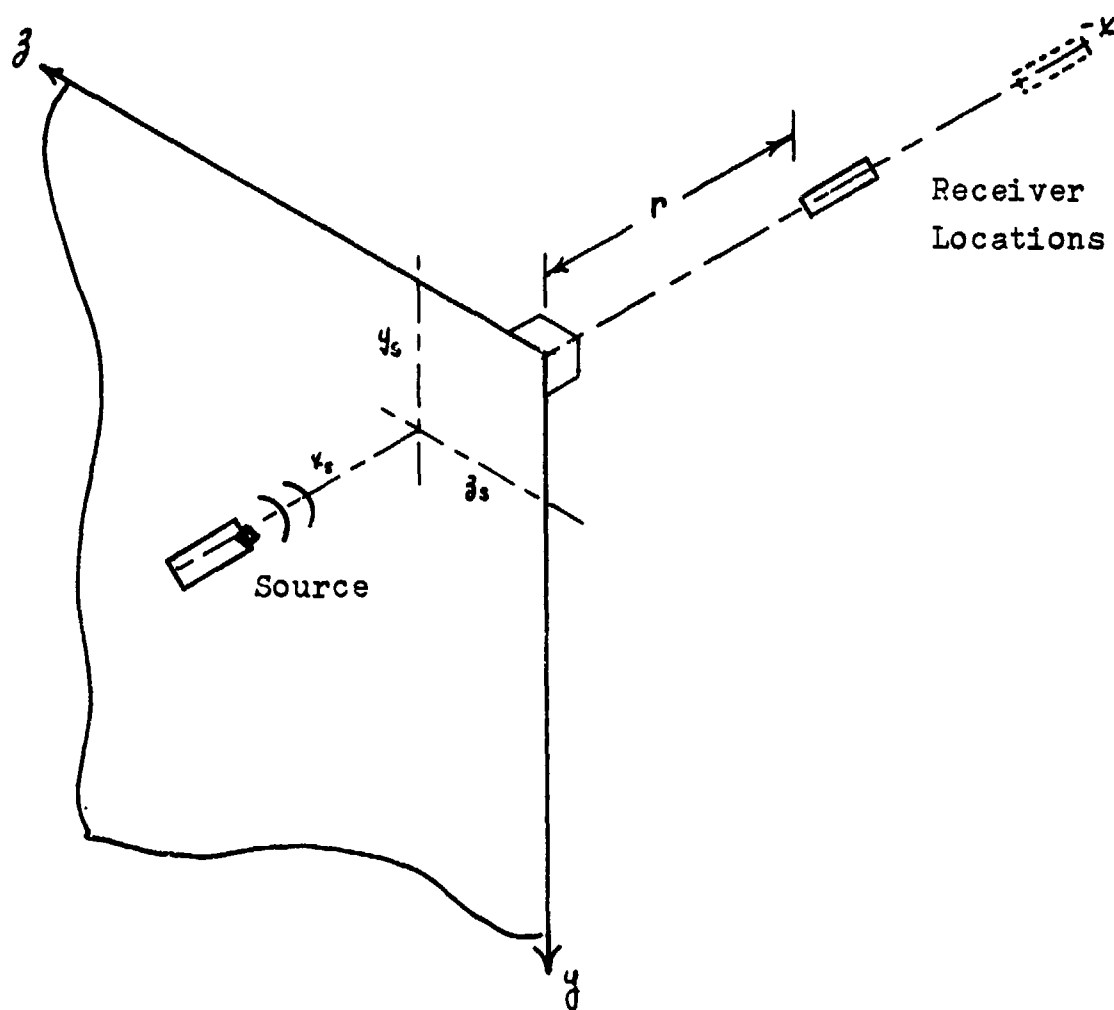


Figure 17. Corner Diffraction Experimental Geometry.

The source was placed at the coordinates  $(x_s, y_s, z_s)$  of 25.5 cm, 8.0 cm, 8.0 cm, respectively. Separate measurements were made using the  $\frac{1}{2}$  and 1 inch sources to achieve the widest possible frequency coverage. The receiver was positioned along the x axis ( $y_r = 0, z_r = 0$ ) at various points between  $r = 3$  cm and  $r = 45$  cm. This geometry was dictated by two considerations; source/receiver directivity and coherent interference. Source and receiver are both to be omnidirectional in the theoretical B-T solution. In order to approximate this adequately, it was considered important that the source appear omnidirectional when viewed from points along a significant portion of the edge near the corner. By orienting the source and receiver in this way all points on the edge between the corner and the point where the least time path crosses the edge were within 2 dB of omnidirectionality up to approximately 30 kHz. The symmetry of the geometry was chosen to eliminate the frequency domain interference pattern created by taking the Fourier transform of a time signal which has two coherent pulses separated by a time delay. The geometry ensures that the diffracted pulses from both edges arrive at the same time. This was accomplished by moving the receiver slightly to maximize the total pulse signal at the nearest and farthest ranges and locating the intermediate measurement points on a straight line between them.

These considerations resulted in a geometry which was somewhat artificial but would allow a relatively simple analysis of the corner effect. The Fourier transformed diffracted pulse data for the 1" and  $\frac{1}{2}$ " sources are presented in Figures 18 and 19 respectively. The free-field pressure at a range of 28 cm (the distance from source to corner) was used as a reference pressure. Although the measured data using both sources show good agreement in the frequency region where they overlap, their dimensions are large enough to be considered as an effect on the results and are therefore presented separately. The theoretical results from truncating and adding the B-T solutions for the two perpendicular edges is also shown. The agreement between the measurements and this superposition of the truncated components of two cases of B-T theory is seen to be excellent across the entire frequency region.

The theoretical and measured results in Figures 18 and 19 also clearly show the effect of moving closer to the shadow boundary. Because of the geometry shown in Figure 17, decreasing  $r$  also moves the receiver nearer to the shadow boundary. The theoretical solution as the receiver approaches the shadow, is shown to approach the delta function form (Appendix A). The measured data clearly show this result, as they approach a flat spectrum for small  $r$ , with the more familiar  $f^{-\frac{1}{2}}$  frequency dependence observed at larger  $r$ .



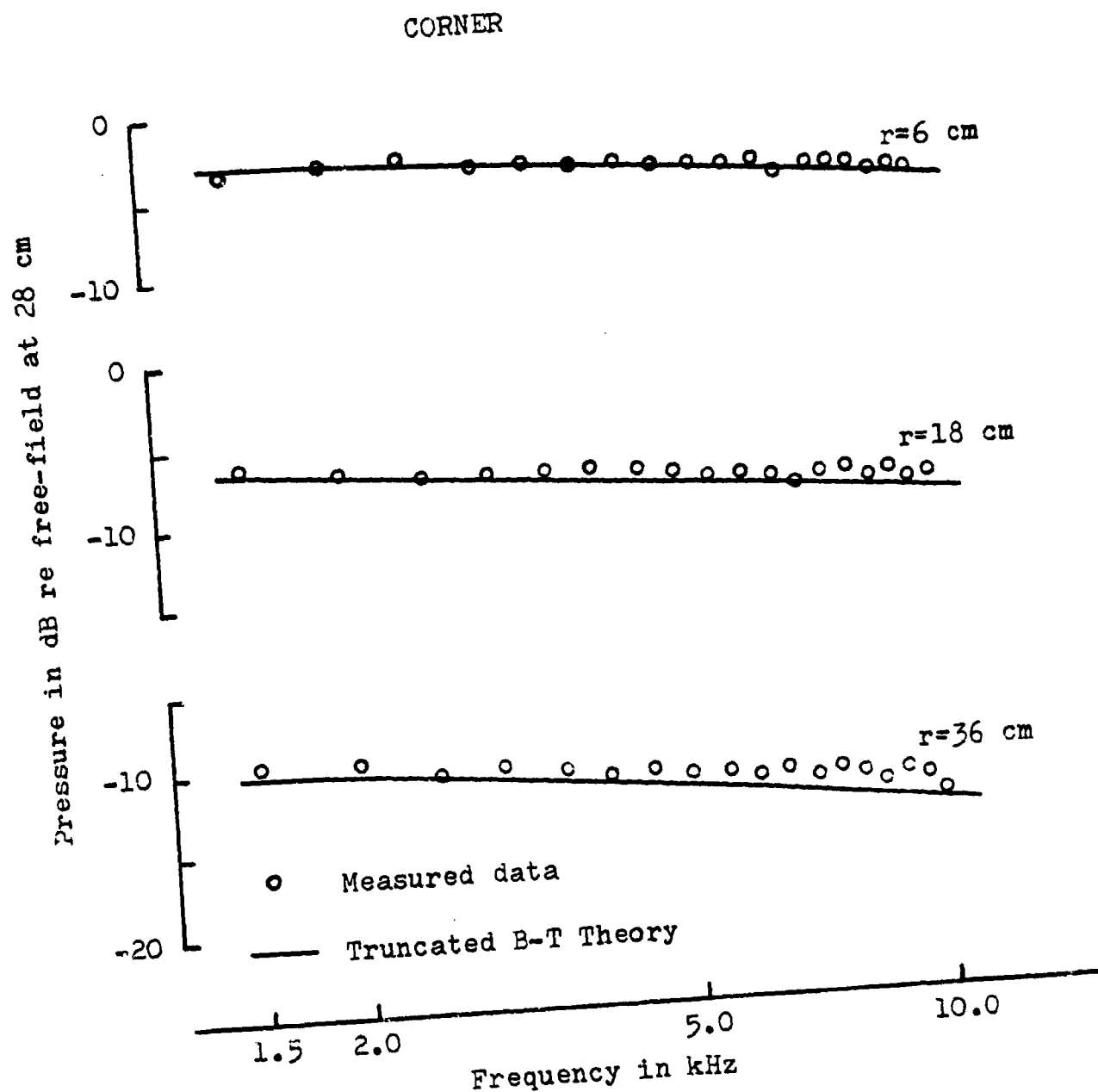


Figure 18. Forward Diffracted Pressure as a Function of Frequency at Various Distances ( $r$ ) from the Corner, 1" Source (Geometry of Fig. 17).

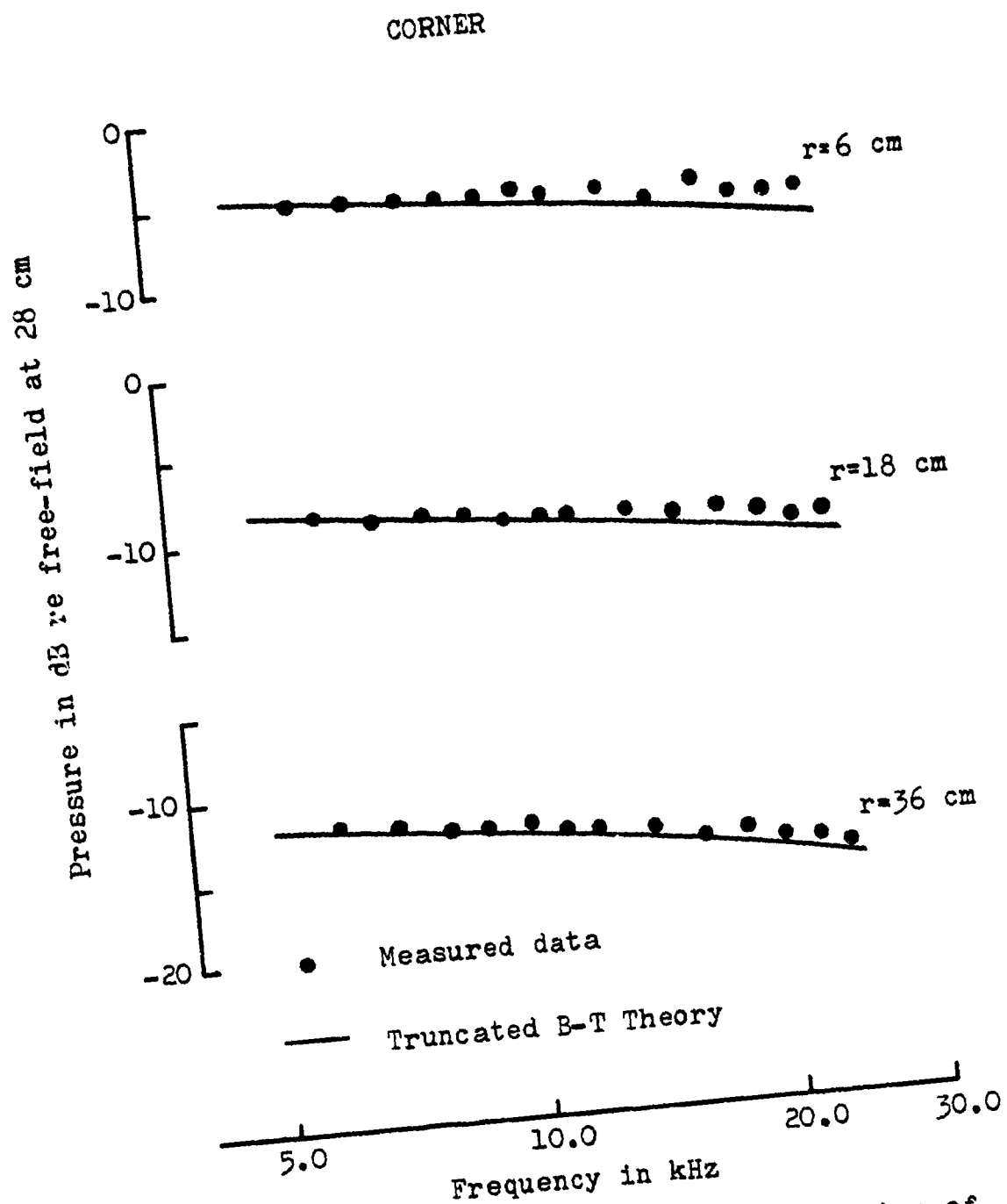


Figure 19. Forward Diffracted Pressure as a Function of Frequency at Various Distances ( $r$ ) from the Corner,  $\frac{1}{2}$ " Source (Geometry of Fig. 17).

In Figure 20, these same measurements are presented as diffracted pressure as a function of range (from the corner) for selected frequencies, once again compared to the sum of "truncated" B-T theoretical solutions. Also presented for comparison are lines of arbitrary level with slopes of  $-10 \log r$  (cylindrical) and  $-20 \log r$  (spherical). An apparent source at the corner would be expected to radiate spherically while an infinitely long edge would radiate cylindrically. Because of the geometry the ranges to the corner and to the point on the edge where the least time "ray" crosses are essentially equal so the data may be examined directly for evidence of a spherical divergence from the corner.

The data, as well as theoretical results, of Figure 20 range from a slope of less than 3 dB per double distance near the corner, low frequency, to almost 6 dB per double distance at the highest frequency and largest distance from the corner. In terms of the dimensionless parameter  $kr$  (wavenumber times range), it appears that the corner cannot be characterized as a simple spherical or cylindrical source for low values of  $kr$ . As  $kr$  is increase, the range dependence gradually increases to a value approaching 6 dB per double distance. Although the results are somewhat inconclusive due to limited data, the two line sources, one at each edge, begin to resemble a virtual point source at higher values of  $kr$ .

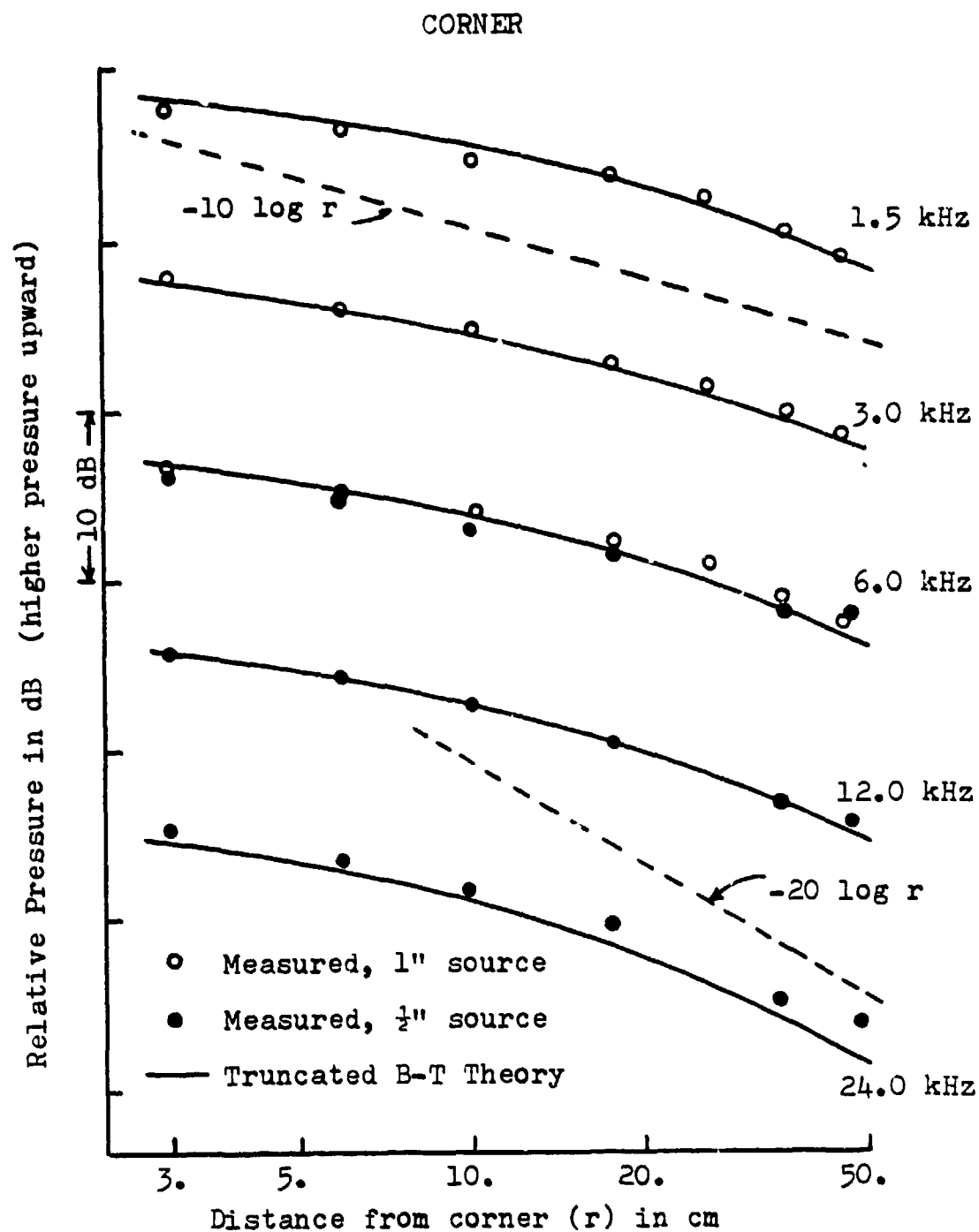


Figure 20. Forward Diffracted Pressure as a Function of Distance from the Corner for Various Frequencies (Geometry of Fig. 17).

An additional experiment was performed to better define the difference between diffraction by an edge and diffraction by a corner. The plate used in this experiment was identical to that used for the corner (Fig. 17) except that the source and receiver were set up on a long edge, as shown in Figure 21. As before, the measured data are compared to the B-T calculated results (for a single infinite edge) in Figures 22 and 23. Unfortunately, the agreement between measurements and theory is not nearly as good in this case as it was for the corner. The reason for the significant deviation between measurement and theory at higher frequencies and small ranges is not known. Figure 24 presents a direct comparison between corner and infinite edge results, as a function of range, along with the appropriate B-T theoretical results.

From this comparison it can be seen that the diffracted pressure field behind the corner is approximately 6 dB higher than that behind a half-plane (single edge) for the larger ranges and higher frequencies. As the receiver moves closer to the plate, the difference between corner and single-edge data decreases. Furthermore, there does appear to be a frequency dependence in the difference between the corner and edge at a given range. To better define this frequency dependence and to estimate the effect of moving away from the shadow boundary, a final experiment was performed.

Referring to the geometry of Figure 17, the receiver was placed distances ( $r$ ) of 18 and 32 cm from the corner on a

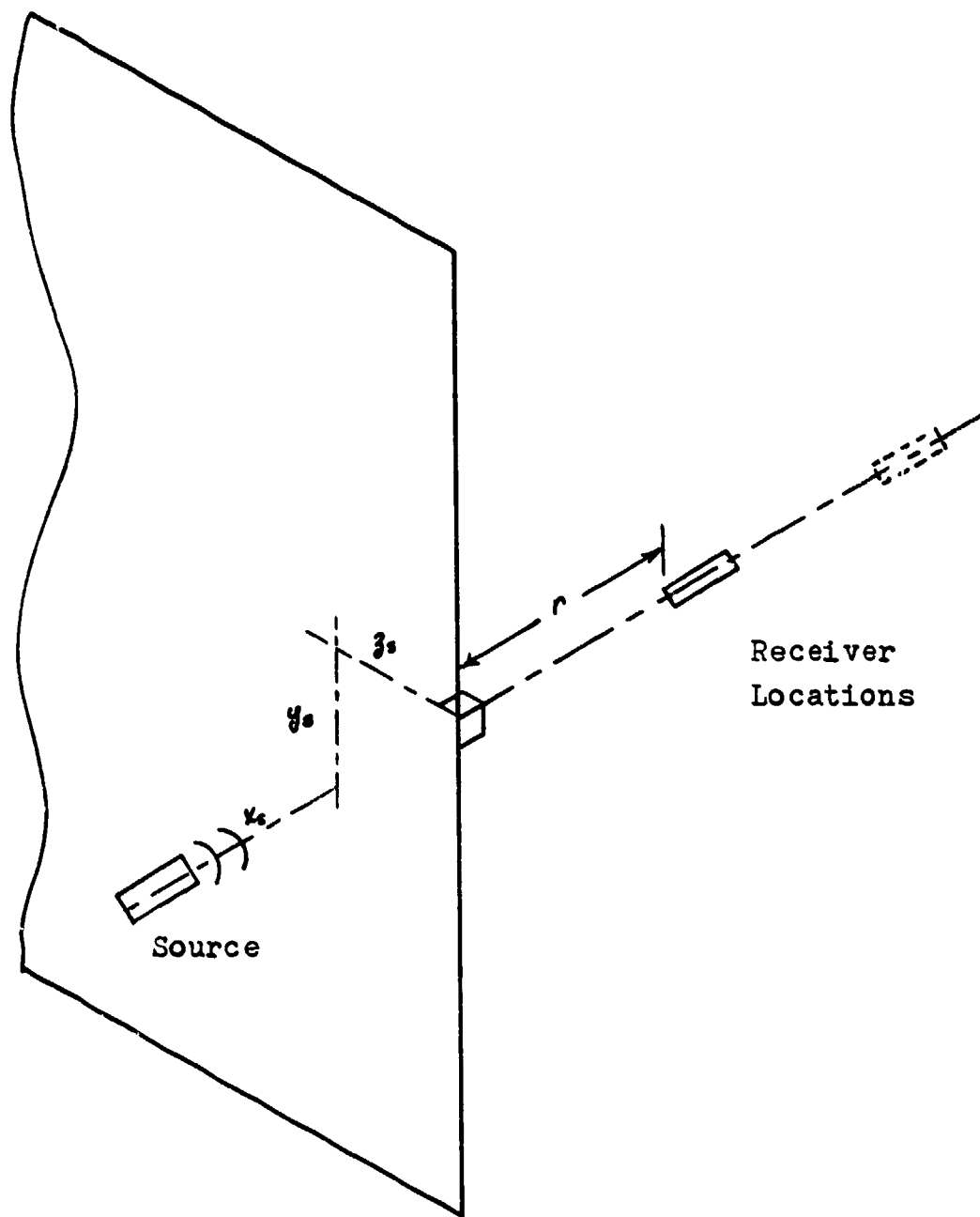


Figure 21. Single Edge Experimental Geometry.

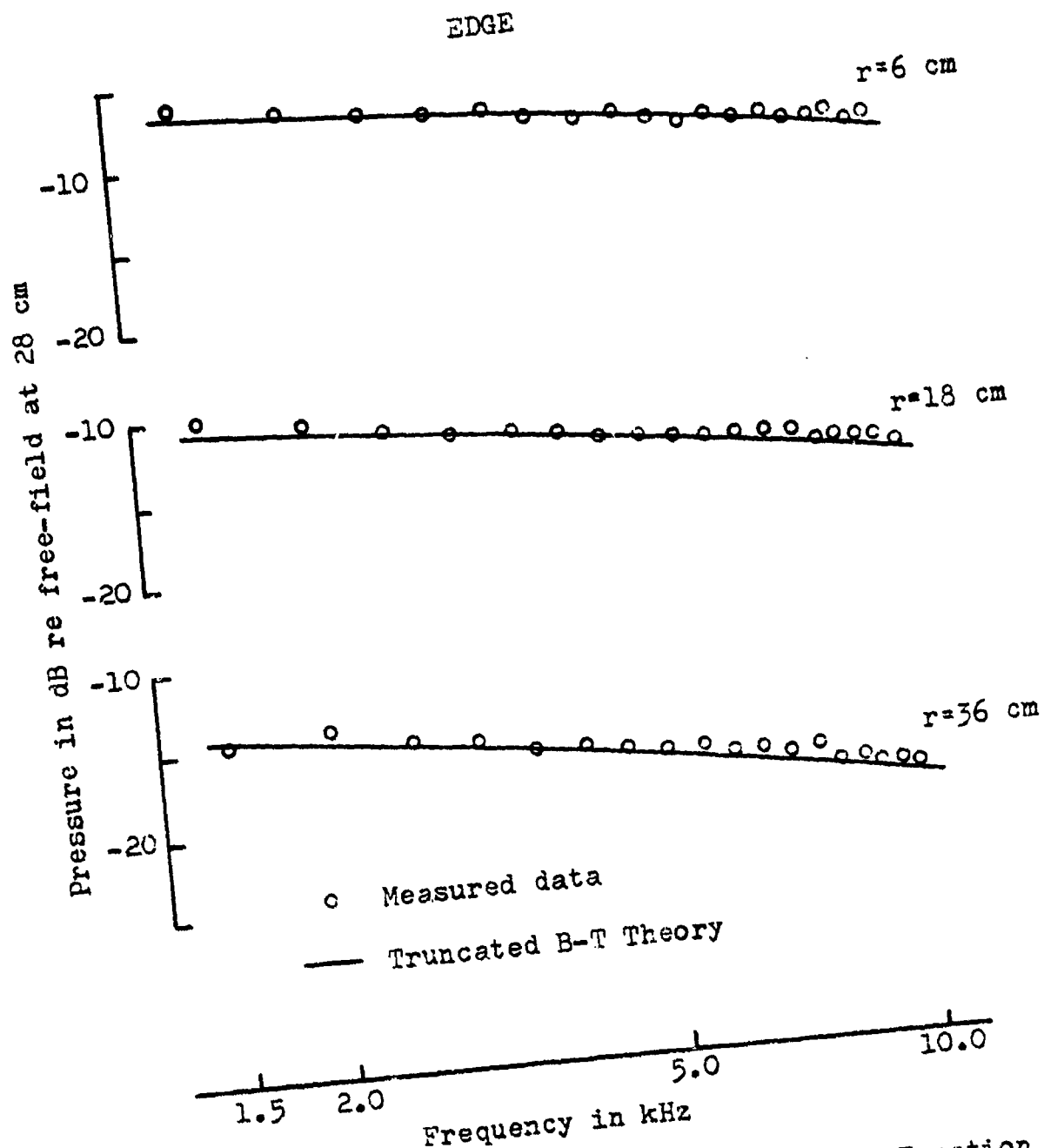


Figure 22. Forward Diffracted Pressure as a Function of Frequency at Various Distances ( $r$ ) from the Edge, 1" Source (Geometry of Fig. 21).

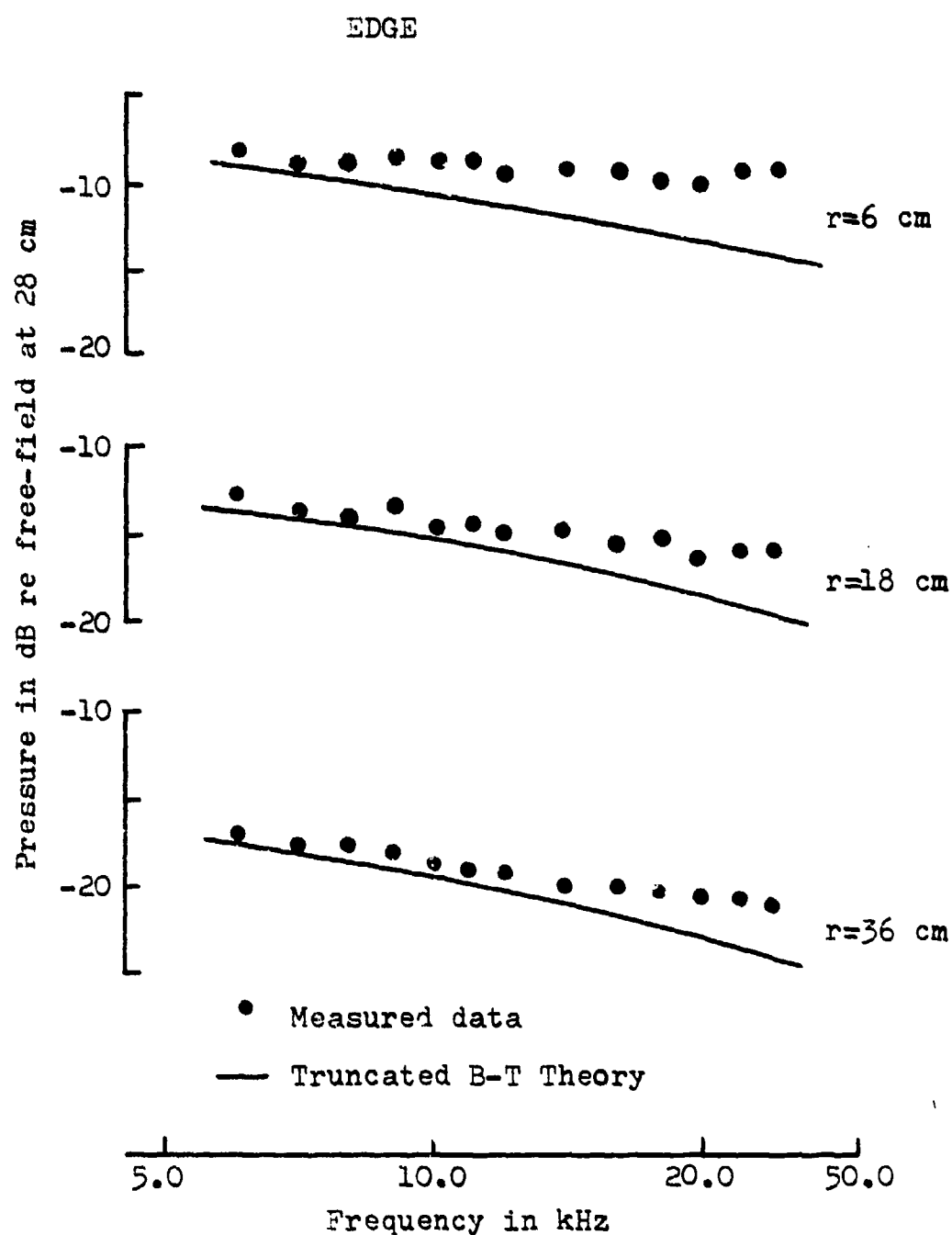


Figure 23. Forward Diffracted Pressure as a Function of Frequency as Various Distances ( $r$ ) from the Edge,  $\frac{1}{2}$ " Source (Geometry of Fig. 21).



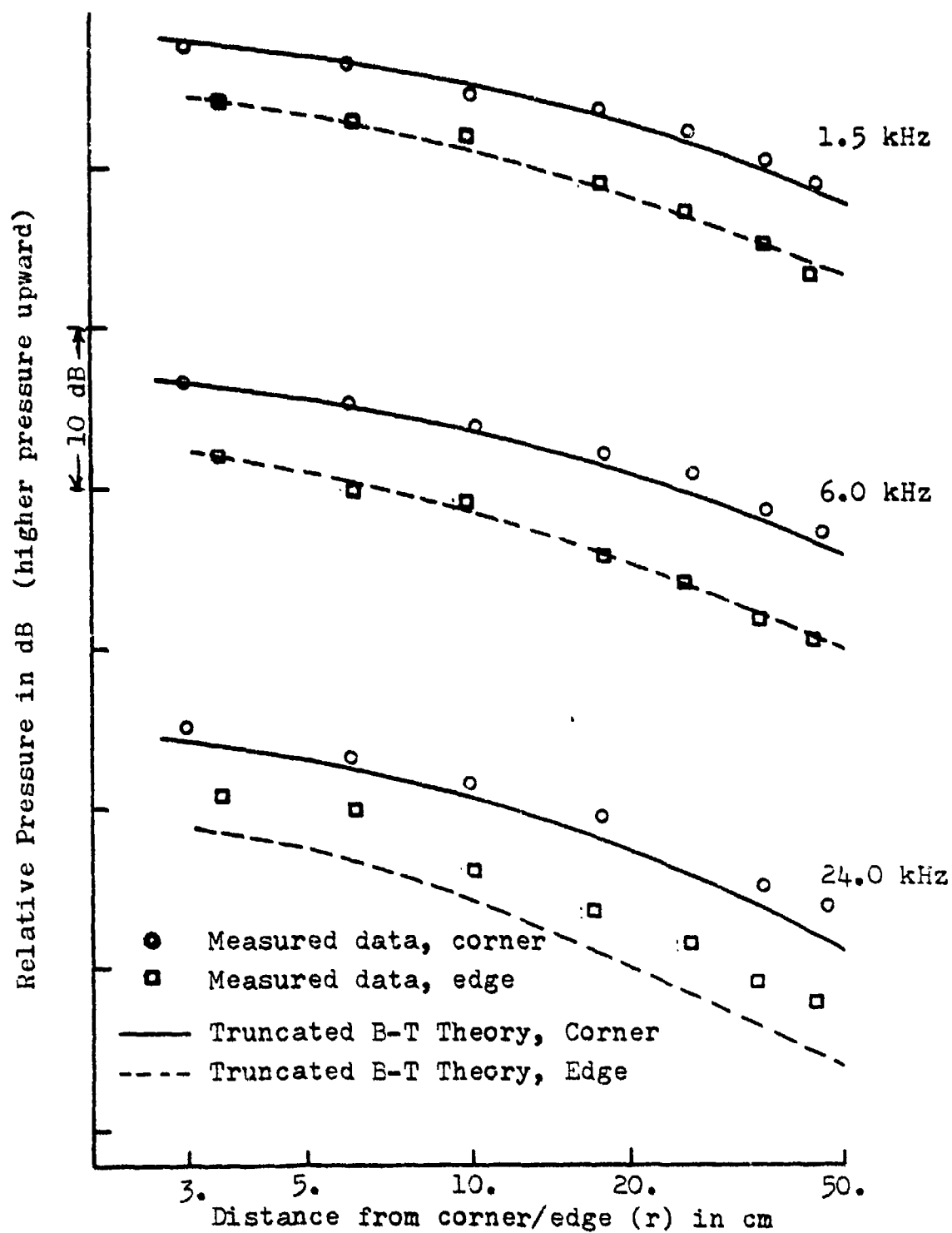


Figure 24. Comparison of Forward Diffracted Pressure as a Function of Distance (r) for the Corner and the Single Edge for Various Frequencies.

line perpendicular to the plate (this is the same geometry as the previous corner measurements). Measurements were also made at distances of 18 and 32 cm from the corner on a  $45^\circ$  line extending into the shadow region "behind" the plate as shown in Figure 25. As before, four identical measurements were made along a single "infinite" edge for comparison. The magnitude of the Fourier transformed data from the corner, divided by the corresponding data from the single edge, are presented in Figure 26. The upper two curves present data taken on the perpendicular line while the lower two are taken on the  $45^\circ$  line (deeper in the shadow). Also shown with the upper curves is the theoretical difference between the corner and edge based on B-T. The general trend indicated by the upper two curves is one of less than a doubling of pressure (due to line sources) at the lower frequencies, increasing to slightly more than double the pressure at the higher frequencies.

When the receiver is moved deeper into the shadow region, the character of the ratio plotted in Figure 26 changes dramatically, as shown by the lower two curves. The monotonic frequency dependence seen near the shadow boundary has been replaced by a more complicated dependence. The average value of the difference appears to be approximately 6 dB, even at the lower frequencies. The detailed frequency dependence will be addressed in the next section. The general conclusion to be drawn from Figure 26 is that the farther the

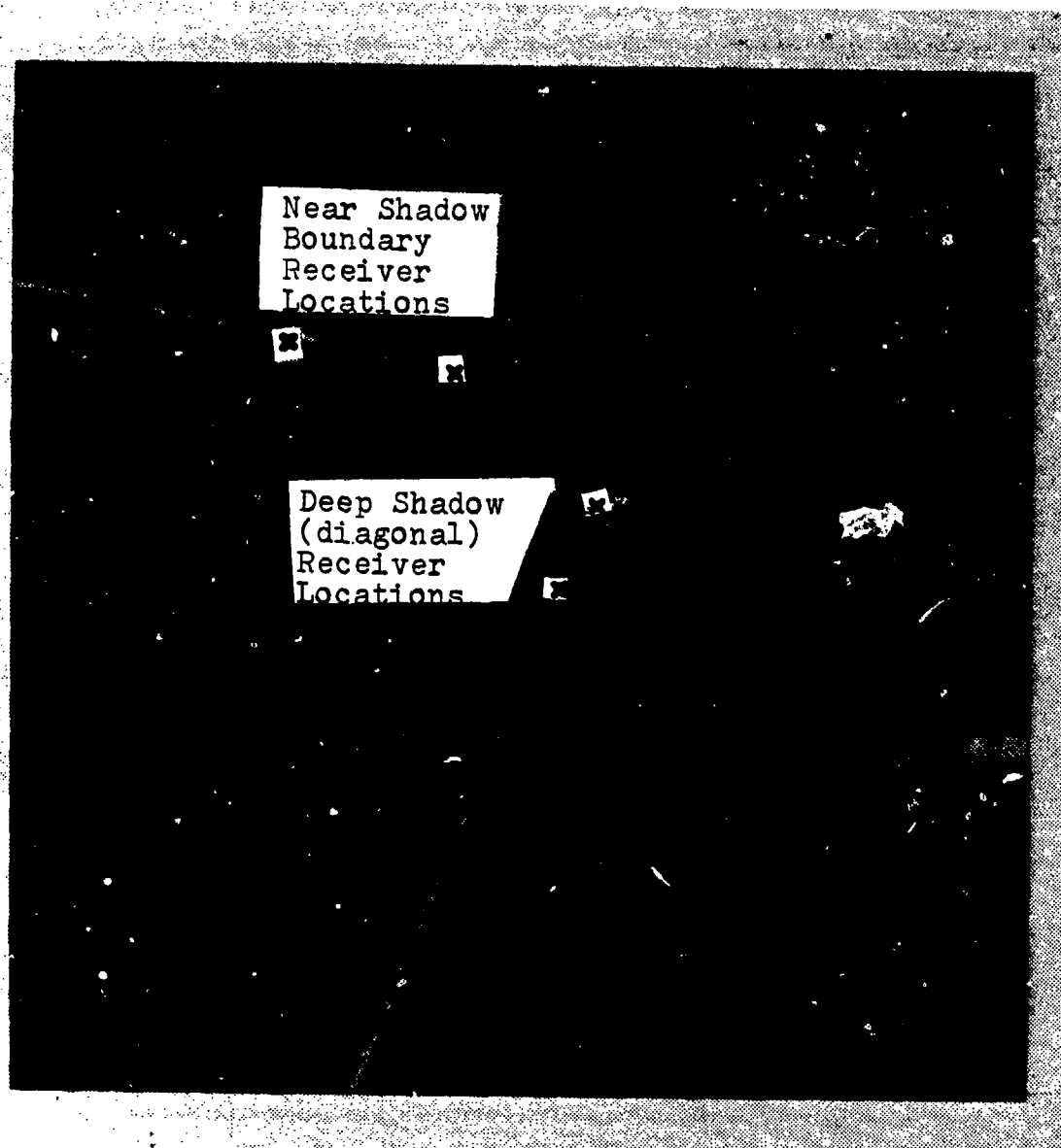
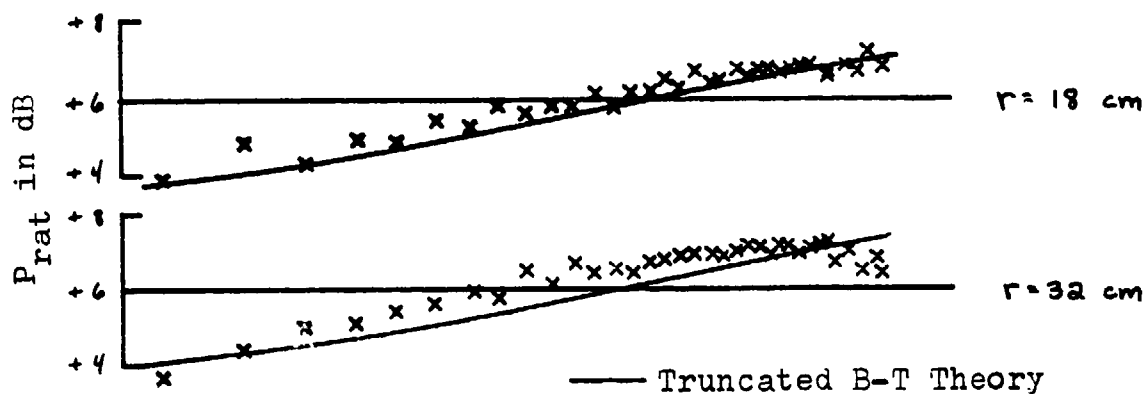


Figure 25. Experiment Geometry for "Near Shadow Boundary" "Deep Shadow" Forward Diffraction Comparison Measurements.

NEAR SHADOW BOUNDARY (Fig. 25)



DEEP SHADOW DIAGONAL (Fig. 25)

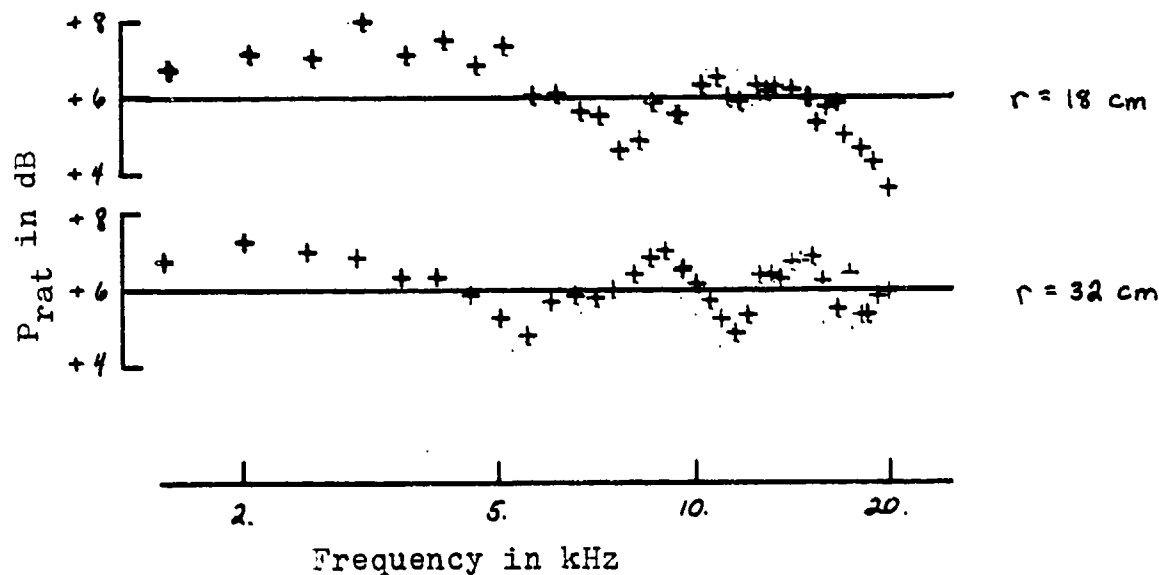


Figure 26. Comparison of  $P_{rat}$  as a Function of Frequency for Receiver Locations in the Deep Shadow and Near the Shadow Boundary (see text).

receiver moves into the shadow region, the more the diffracted pressure field looks like the coherent addition of two infinite edges, plus a small frequency dependent variation.

In summary, the measurements presented herein show that the basic approach of adding impulse diffractions from each edge in the time domain is valid. Near the corner, the diffracted pressure is less than a simple addition of two infinite edge diffractions. In this region, the approach proposed by Medwin [Ref. 8], wherein the time domain solution is "truncated" at the point where the edge wave reaches the corner, estimates the diffracted pressure very closely as shown by Figures 18 and 19. The usual treatment of the corner as a source of spherically diverging diffracted sound is not evident in the measured or B-T theoretical results, at least over the lower range of  $kr$  presented. At high values of  $kr$ , the results may be approaching spherical divergence.

In the high frequency limit, Keller [Ref. 16] predicts that the corner does produce spherically diverging waves but that the resulting diffracted field decreases with increasing frequency much more rapidly than the field produced by an edge. This characteristic has been used as justification for disregarding the diffraction at a corner when approaching practical problems [cf. Ref. 17]. Figure 26 would seem to indicate that radial distance from the corner and frequency are not sufficient to determine when to disregard the effects

of a corner; one must also consider the relationship of the receiver location to the shadow boundary. The dimensionless parameter implied in Medwin's truncation approach is  $kd$  where  $d$  is the distance from the corner to the point where the least time "ray" intersects the edge. No substantiation for this parameter is offered here, however it does take into account both distance from the corner and nearness to the shadow boundary.

### C. FORWARD DIFFRACTION BY A STRIP

The next experiment was designed to investigate the behavior of diffraction from an "infinite" strip of material whose width was of the order of a wavelength. Two strips were actually measured, with widths 10 cm and 4 cm. Given the measurement capability of 1.5 to 40 kHz, these two strips provided a total range of  $ka$  ( $a$  represents the width of the strip) of 1.09 to 72.8. Source and receiver were located on a perpendicular line through the center of each strip, as shown in Figure 27a. The source was 14.5 cm from the strip for all tests while the receiver was located at distances from the strip of 9.5, 23.2, 39.5, and 59.5 cm in the case of the 10 cm wide strip and 9.5, 23.2 for the 4 cm strip. Once again, this geometry was chosen to eliminate the coherent interference that would result from different path lengths around each edge. Identical measurements were also performed on a single "infinite" edge as shown in Figure 27b.

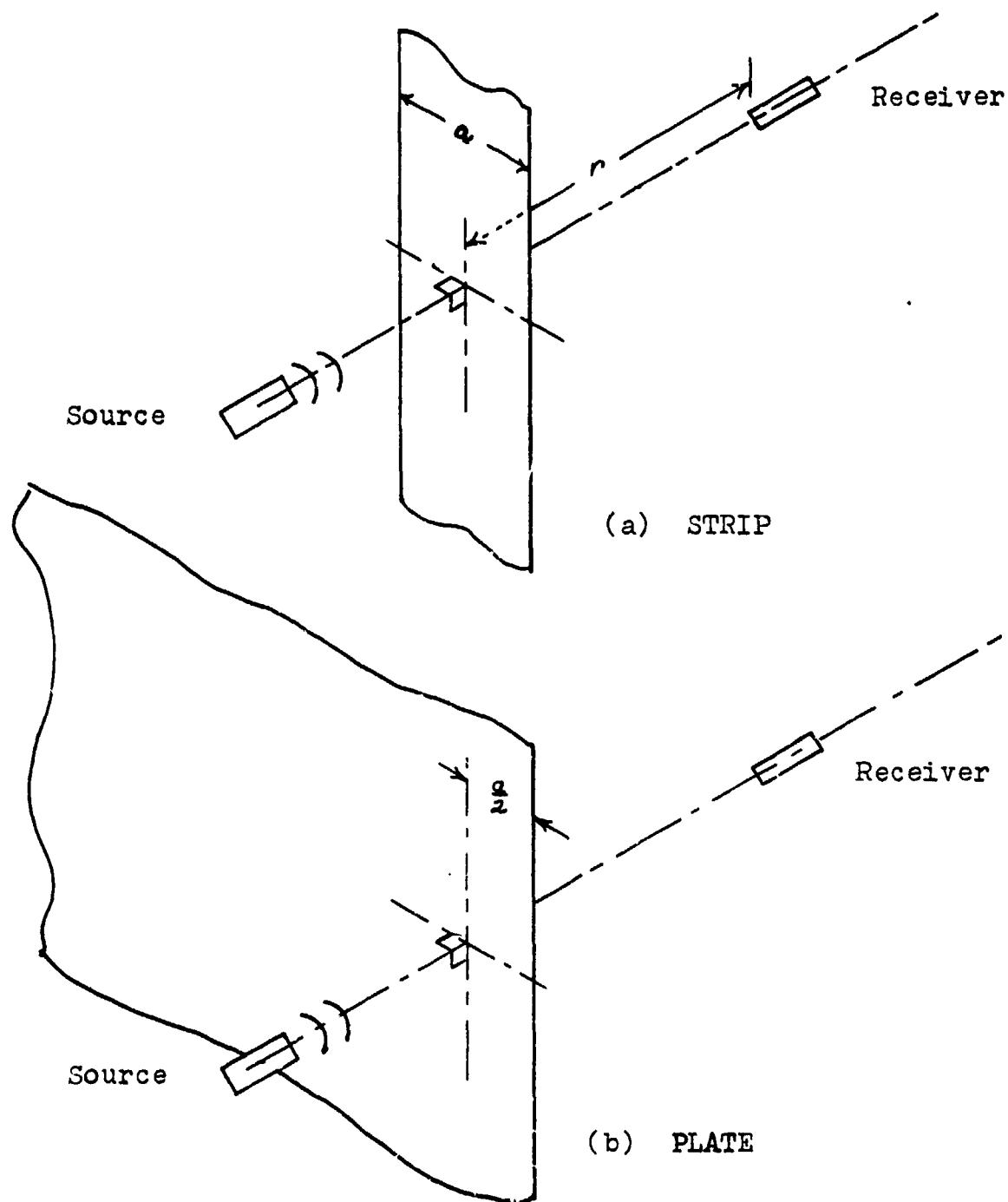


Figure 27. Strip Diffraction Experimental Geometry.

As long as linear superposition of edge effects holds, the diffracted pressure at any of the measurement points will be double for the strip compared to the corresponding plate (single edge), since there is no truncation involved. With this in mind, all data are presented as the following ratio:

$$p_{\text{rat}} = \frac{\text{diffracted pressure behind strip}}{\text{diffracted pressure behind plate}}$$

When superposition holds, there will be a simple doubling of pressure and this ratio will be +6dB at all frequencies.

This ratio, calculated from the measurements on the 10 cm strip and corresponding plate, is presented in Figure 28. The data are not presented above 30 kHz because of limitations in the determination of the perpendicular to the strip (i.e. the path lengths around the two edges could not be equalized well enough to prevent cancellation effects above this frequency). The oscillating pattern in the low frequency portion of the measurements is evident from Figure 28. If this is interpreted as coherent interference between two signals, two features can be extracted from the data. First, this interference pattern does not depend on distance from the strip/plate. Second, by estimating the spacing (in frequency) between adjacent peaks or between adjacent nulls the apparent path difference can be calculated from the relation  $d = \lambda = c/\Delta f$  in meters. From the data of Figure 28,  $d$  is estimated to be 9 cm, quite close to the strip width of 10



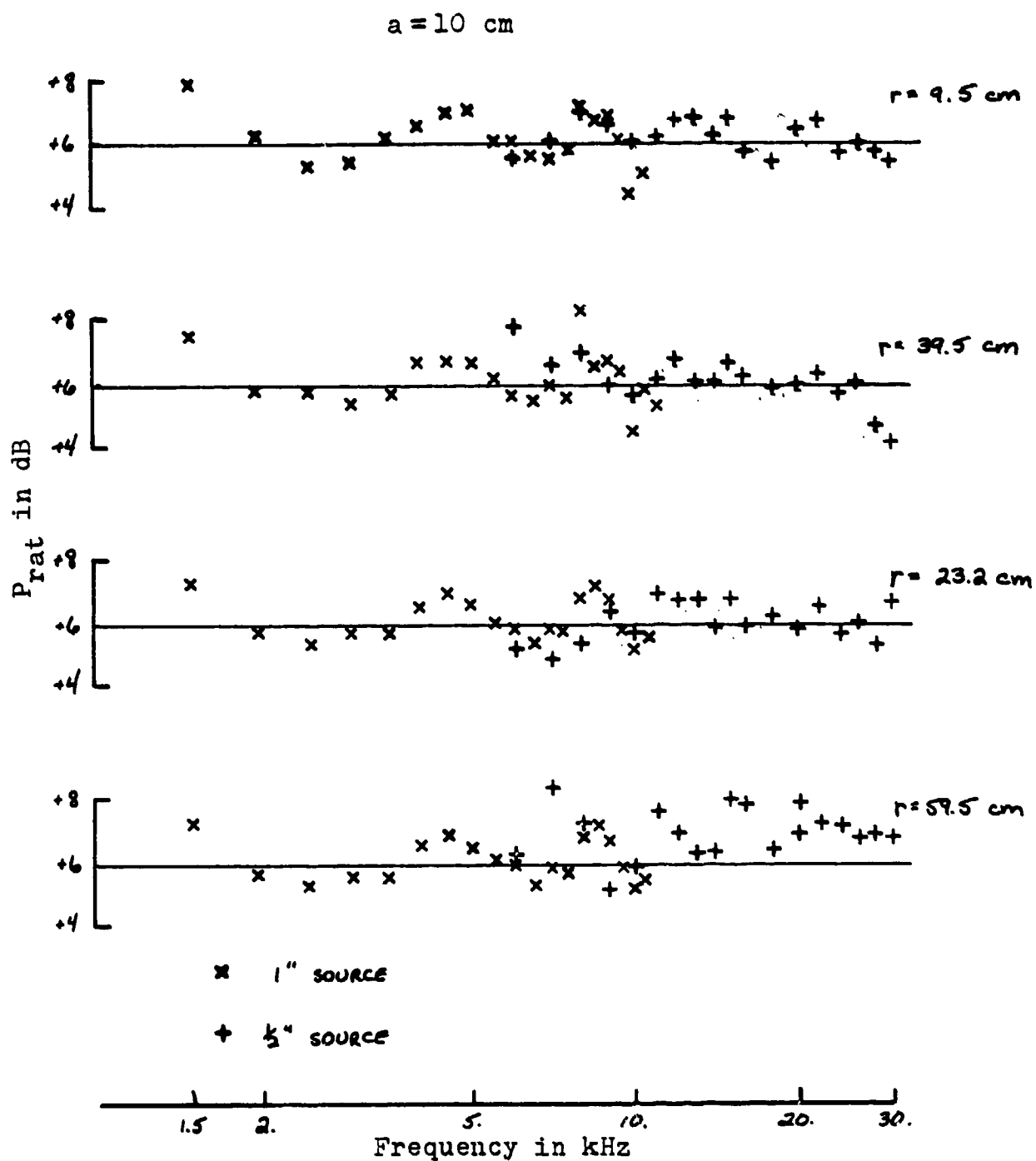


Figure 28. Comparison of  $P_{rad}$  as a Function of Frequency at Various Distances ( $r$ ) for the 10 cm Strip (Geometry of Fig. 27).

cm. To verify that strip width is the characteristic dimension, the experiment was repeated for the 4 cm strip.

The 4 cm strip results are presented in Figure 29. The strip width from Figure 29 data is estimated to be 4.1 cm, confirming that the width of the strip is the factor determining the form of the "interference pattern".

The data measured at 9.5 and 23.2 cm are averaged and plotted as a function of  $ka$  for both strips in Figure 30. For simplicity, the data from both 1 inch and 1/2 inch sources were averaged in the overlapping region 6-10 kHz. Figure 30 clearly shows that the frequency dependence is directly related to the strip width  $a$ , with a  $ka$  spacing of  $2\pi$  between peaks as expected from a simple interference pattern.

The physical explanation offered for this interference is called secondary diffraction or secondary scattering. The application of secondary diffraction to the strip is illustrated in Figure 31. The figure shows only the interaction at one edge; the mirror image of the process shown is occurring simultaneously at the other edge. The solid lines in Figure 31 depict the path of the pulse as it diffracts over the upper edge, while the dashed lines show how the diffraction of the same pulse at the opposite edge generates signals on both sides of the strip which propagate across the strip and diffract once again at the upper edge. The doubly diffracted pulse arrives at the receiver at time equal to the width ( $a$ ) divided by the propagation velocity

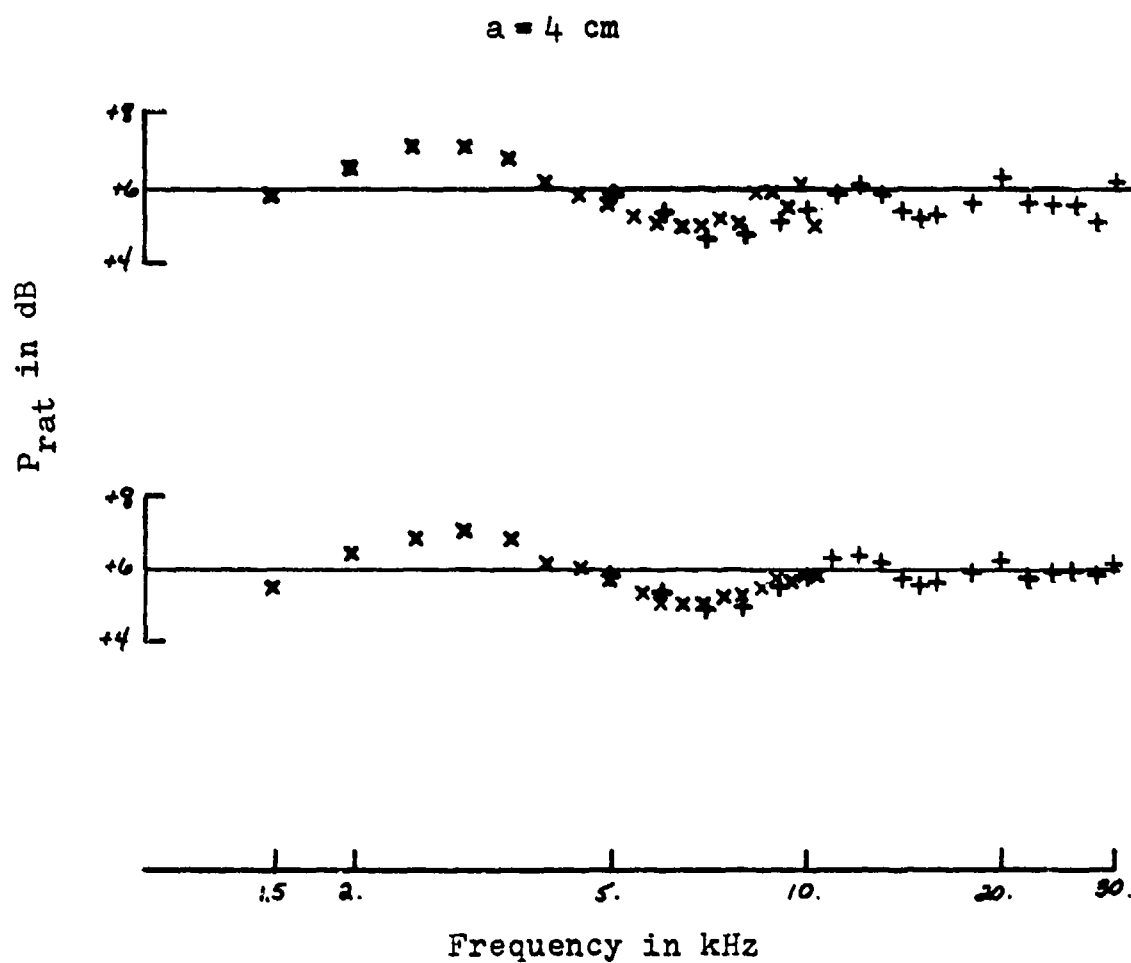


Figure 29. Comparison of  $P_{rat}$  as a Function of Frequency at Various Distances ( $r$ ) for the 4 cm Strip (Geometry of Fig. 27).

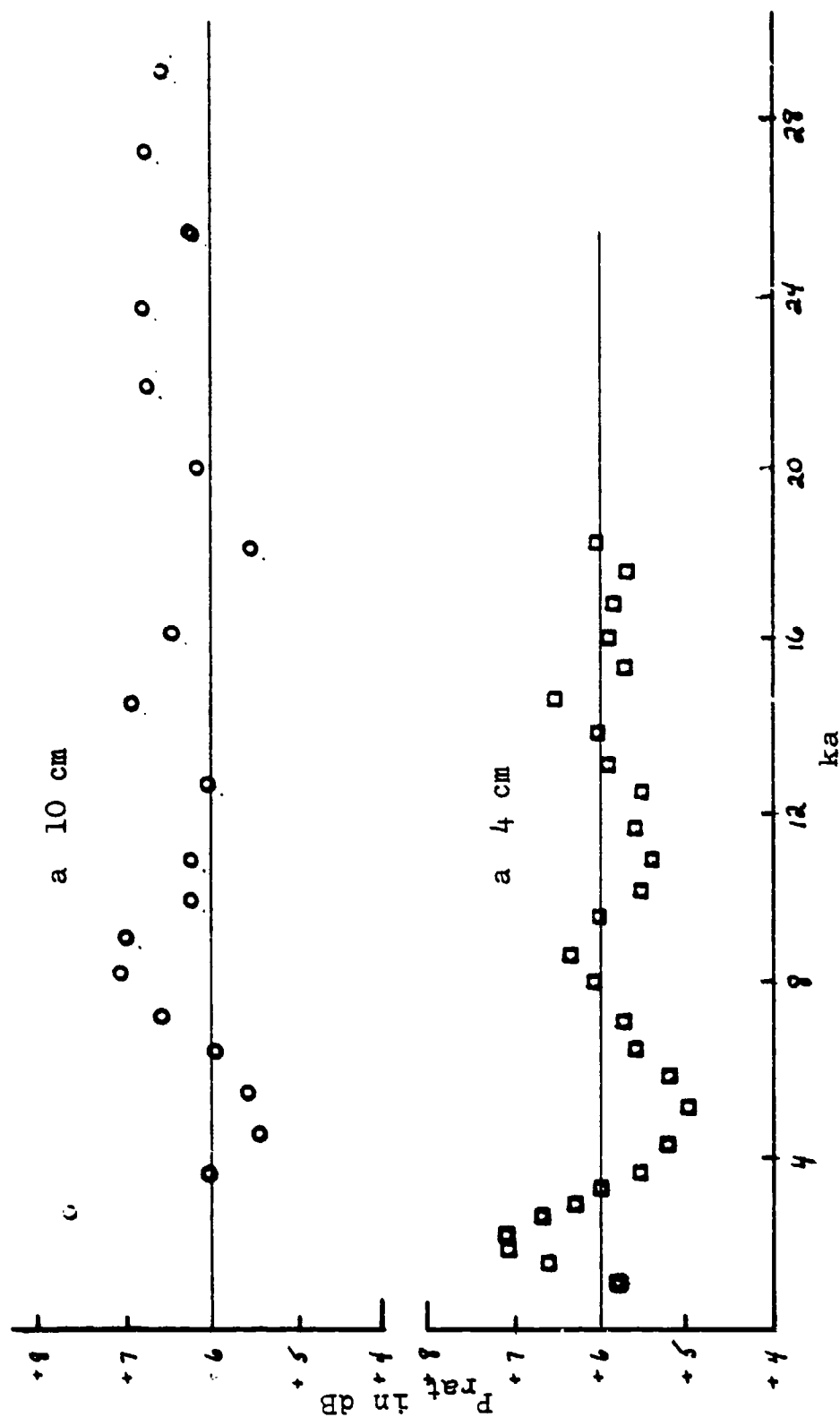


Figure 30. Comparison of  $P_{rat}$  as a Function of  $ka$  for the 4 and 10 cm Strips.

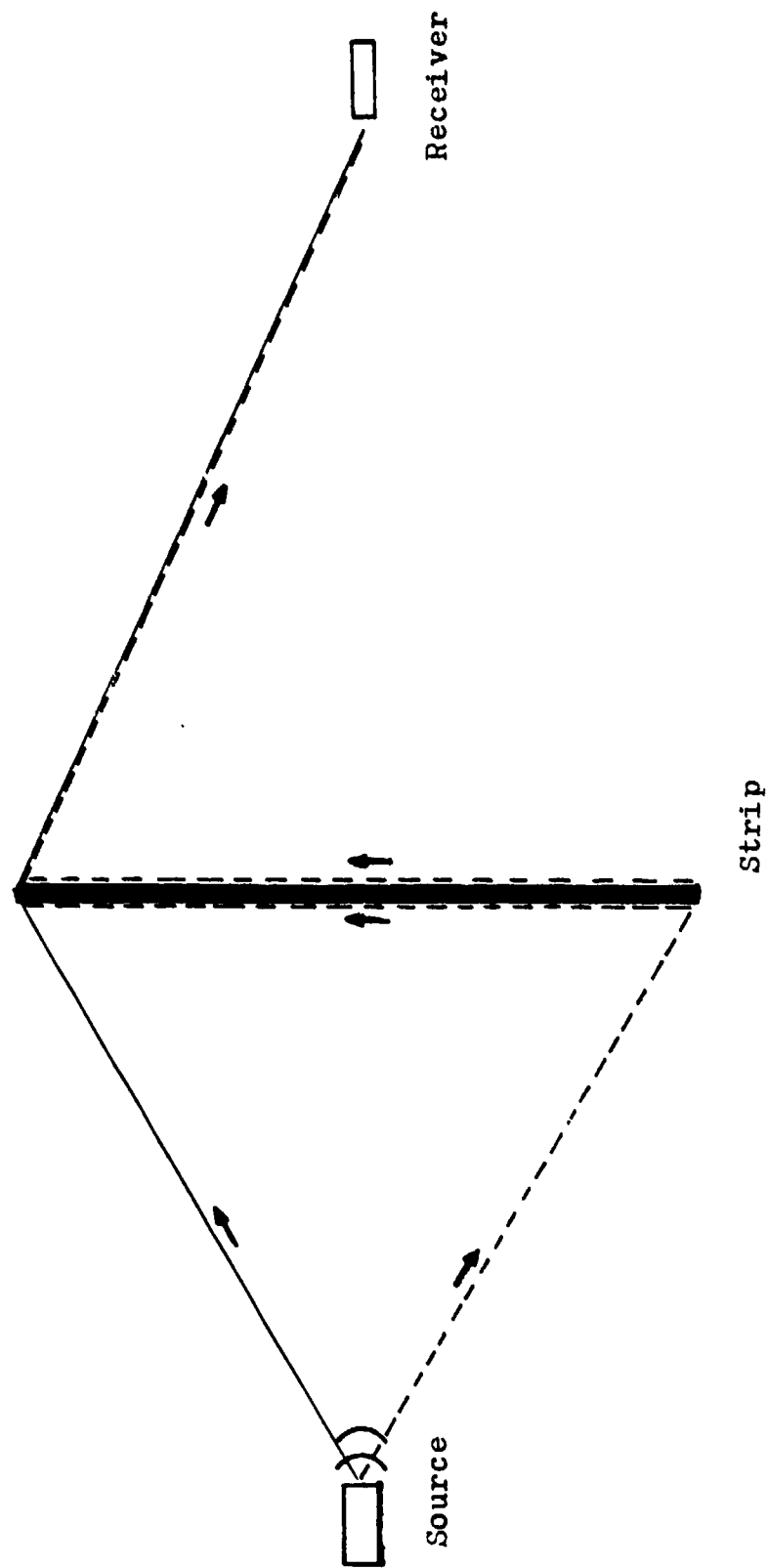


Figure 31. Secondary Diffraction (Dashed Line) Concept Applied to the Strip.

(c) later than the initial pulse, resulting in the observed interference pattern. This late pulse would have two distinct characteristics, arising from the additional diffraction, which are immediately observable in the measured data of Figure 30. First, it will be considerably reduced in amplitude relative to the earlier (single diffraction) pulse. This is seen in the data as a weak interference pattern (the peaks are approximately  $6 + 1$  dB compared to  $6 + 6$  dB if the two were of equal amplitude). Second, the difference in amplitude between singly and doubly diffracted pulses will be greater with increasing frequency since each diffraction should increase the frequency dependence and decrease the strength of the diffraction by approximately  $f^{-1/2}$ . This causes the decaying amplitude of the interference pattern with increasing frequency.

A method of calculating the secondary diffraction has been proposed by Medwin<sup>1</sup> and implemented by Ms. Emily Childs. The general description of the implementation which follows is due to Childs.<sup>2</sup> When a spherical pulse intersects an edge, a boundary or edge wave is generated which appears to propagate along the edge. Calculating the B-T time domain solution in discrete time increments, this edge wave becomes a series of discrete sources on the edge, each with a

---

<sup>1</sup>Personal communication to author from Dr. H. Medwin.

<sup>2</sup>Personal communication to author from Ms. E. Childs.

characteristic amplitude and phase. Extending this to a two edge system (the thin edged strip in this case), these discrete sources on the first edge (now called secondary sources) each diffract at the second edge and contribute to the diffracted field at the receiver. The proper amplitude is assigned to each secondary source through a system of virtual receivers located at the second edge. The phase of each source is taken into account by performing the entire calculation in the time domain. Figure 32 presents the results of this theoretical calculation in terms of  $P_{rat}$  for each strip at a receiver distance of 23.2 cm., compared to the measured data from Figure 30. Two theoretical curves are presented for each strip; one which considers the secondary diffraction on both sides of the strip (double secondary path) and one which considers secondary diffraction only on one side (single secondary path). Although the double secondary path is the intuitively correct interpretation, the measured data obviously agree with the single path approach. One possible explanation is that in using the double path interpretation, each path should be reduced in amplitude by 1/2 (the diffracted pressures along the paths on either side of the strip are of equal amplitude but opposite sign). Keller [Ref. 16] describes a similar phenomenon for the thin slit in an opaque plane using the Geometrical Theory of Diffraction.

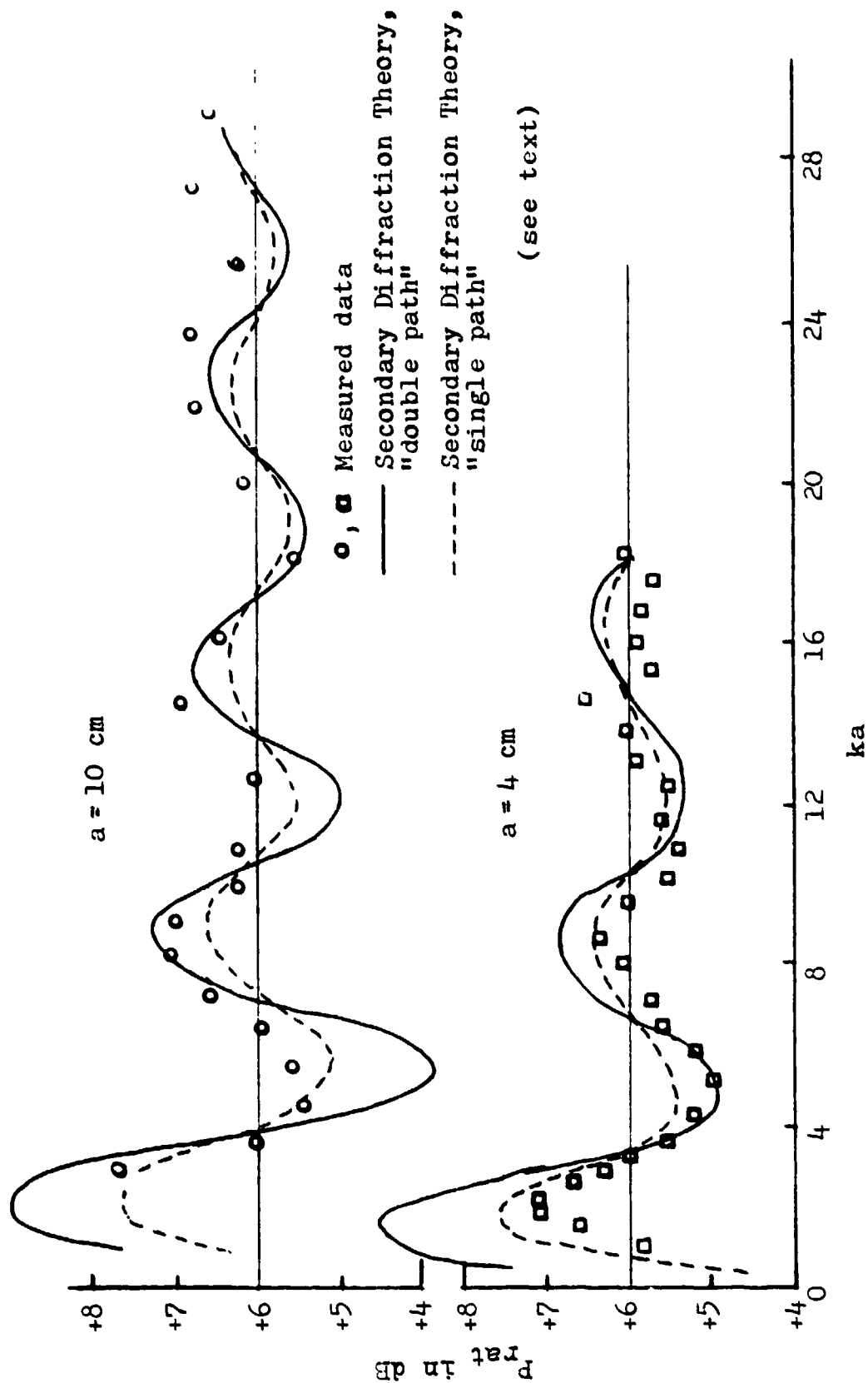


Figure 32. Comparison of Measured and Theoretical  $P_{rat}$  as a function of  $ka$  for the 4 and 10 cm strips.



At this point it is also appropriate to point out that the use of secondary diffraction in the preceding explanation of the interference pattern would not be possible with the Helmholtz-Kirchhoff approach, since the scattered or diffracted field on the plate would be zero. There would be no way the pulse could propagate between edges.

It appears that the secondary diffraction explanation can also be applied to the somewhat more complicated geometry of the corner. Recalling Figure 26, there was a detailed frequency dependence in the results, especially where the receiver was deep in the shadow region (the lower curves of Figure 26). Consider now a corner with one edge horizontal and one vertical as shown in Figure 17. There will be a pulse that travels from source to receiver by diffracting over the horizontal edge. In addition, a pulse also diffracts at the vertical edge, propagates across the plate near the corner, and diffracts over the horizontal edge to the receiver. Unlike the strip, the difference in path length of the two pulses is a function of distance from the corner, an effect which can be observed as a difference in the interference patterns in the two lower curves of Figure 26.

#### D. FORWARD DIFFRACTIONS BY A THICK BARRIER

The usual theoretical approach to solving the problem of diffraction by a plate is to consider it to be an

infinitely thin, rigid half-plane. However, a real barrier which significantly attenuates the direct path of sound must, of necessity, have a thickness which is a significant fraction of a wavelength at high frequency. In Reference 12, Bremhorst presented data which showed the diffracted pressure at various points in the shadow of a 3/16" thick steel plate. In particular, Figures 37 through 46 of Reference 12 showed that the measured diffracted pressure was generally less than that predicted by B-T, especially near the surface of the plate (on the shadow side). Bremhorst attributed this to the finite thickness of the plate. To confirm this hypothesis, an experiment was performed using two barriers of different thickness.

The variable thickness was achieved by placing a piece of aluminum stock of the appropriate thickness between two 3/16" aluminum plates and machining the resulting "edge" smooth and square. Damping material was placed in the gap between the plates to attenuate the direct path. An example of the thick edge can be seen in the photograph of Figure 14. Thicknesses of 2.2 and 3.5 cm were evaluated utilizing the geometry shown in Figure 33. Measurements were made at  $\theta = 300^\circ$  and  $345^\circ$ , where there was considerable disagreement between Bremhorst's measurements and B-T theory. The measured data are shown in Figure 34, compared to the Bremhorst's results and the B-T theory.

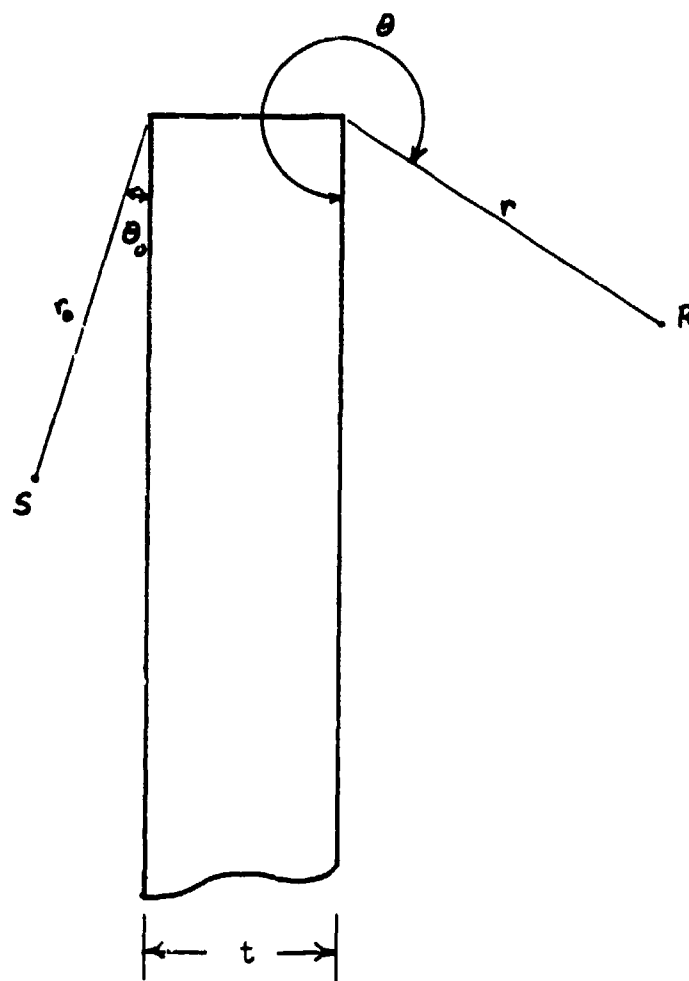


Figure 33. Thick Barrier Measurement Geometry.

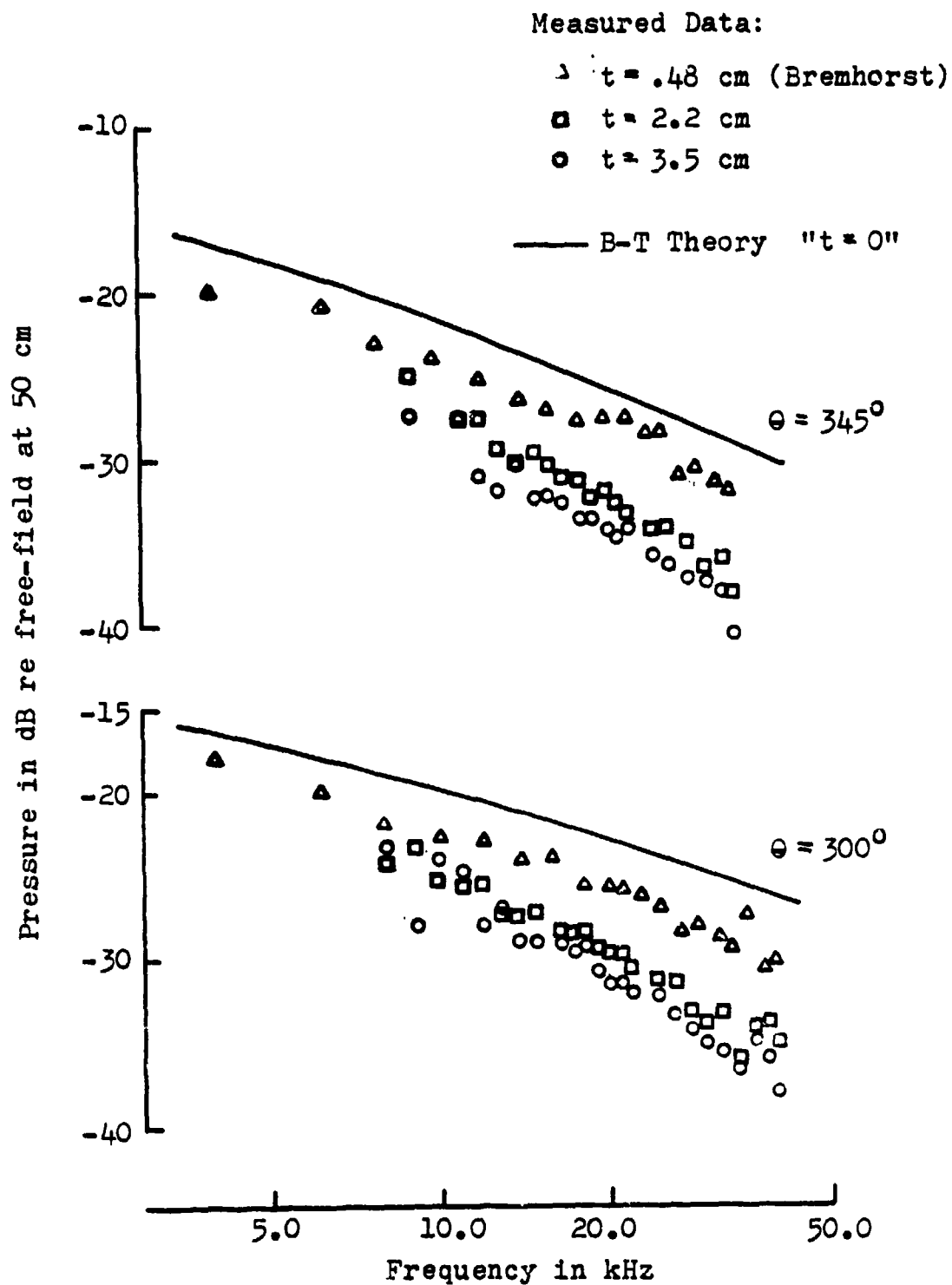


Figure 34. Forward Diffracted Pressure as a Function of Frequency for Various Thickness ( $t$ ) Plates,  $\theta_0 = 15^\circ$ ,  $r=r_0=25$  cm.

The data presented in Figure 34 indicate that barrier thickness is an important parameter in determining the diffracted pressure field, especially when the thickness is on the order of  $\frac{1}{2}$  wavelength (10-15 kHz for the thick barriers tested). It has been suggested by Medwin<sup>3</sup> that this thickness can be handled by a secondary diffraction calculation based on the B-T theory, as discussed earlier for the thin strip, by considering the thickness to be a double edge. This has not been verified at this time, although the thickness does appear to explain the discrepancy between Bremhorst's data and the B-T theory.

#### E. FORWARD DIFFRACTION BY A BARRIER ON A RIGID BASE

A typical noise control barrier consists of a plane screen or plate mounted perpendicular to a flat base, as shown in Figure 35. The total pressure field at the receiver, if it is in the shadow region, consists of the source signal arriving via multiple paths. The usual approach to solving this problem is to consider that for the top edge there are four geometrically distinct paths, each involving one diffraction at the top of the barrier, made up of all possible combinations of source, receiver, and images of source and

---

<sup>3</sup>Personal communication to the author by Dr. H. Medwin.

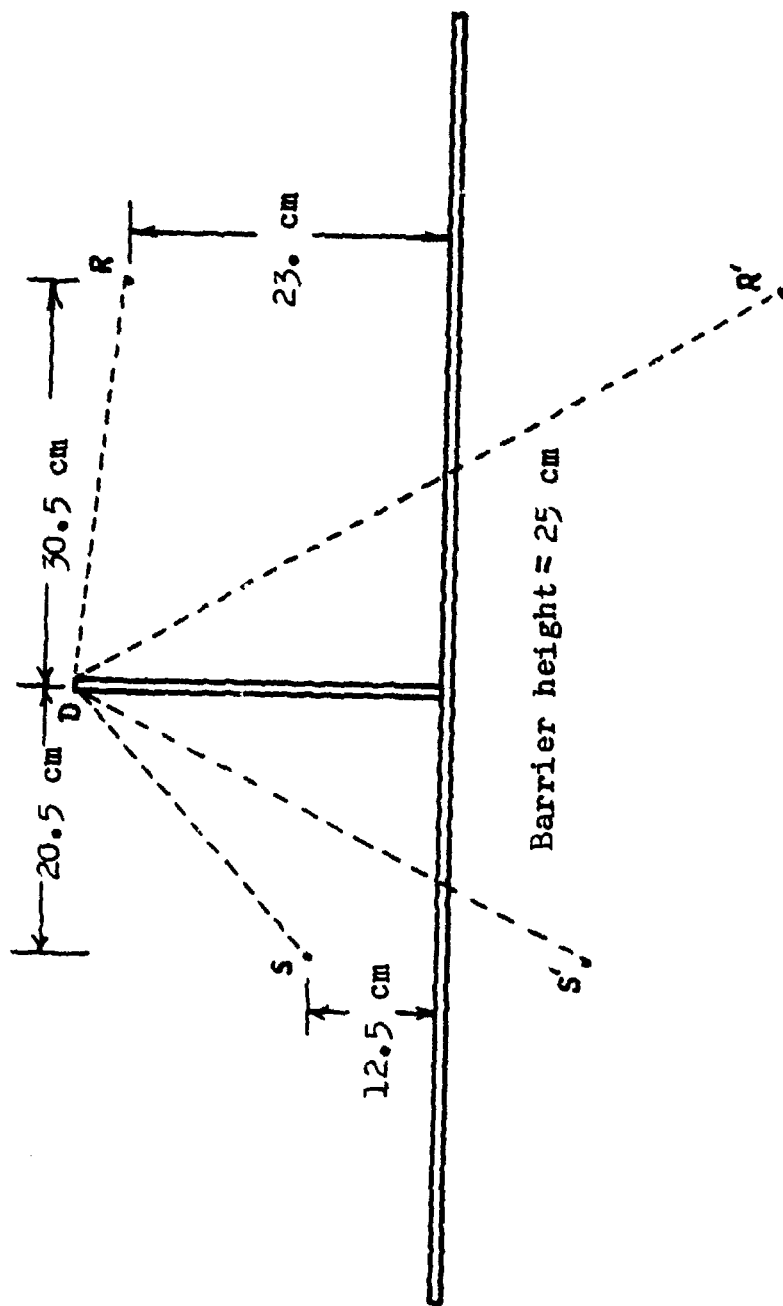


Figure 35. Geometry of Barrier on Rigid Base.

receiver in the base, as shown in Figure 35. Using the notation of Figure 35, these paths are denoted as SDR, S'DR, SDR', S'DR'. It should be pointed out that S' and R' here are true images as used in optics and acoustics to describe reflection from a plane surface. The term "image" is also used by authors in the noise control field [cf. Ref. 5] in conjunction with the "image of the source in the barrier", as discussed in section II. This usage is considered here to be inappropriate and will always be set apart by quotation marks ("image") to prevent confusion with the more common term (image).

To test the hypothesis that the four paths described above adequately characterize propagation from source to receiver in this case, a simple experiment was performed. A barrier with base was constructed of 3/16 inch aluminum plate with an overall width of 120 cm and barrier height of 25 cm in the basic configuration shown in Figure 35. Source and receiver (both 1/2" B+K microphones) were positioned so that each of the four paths would have a different length, and each path would intersect the axis of the microphone at approximately the same angle. This would allow at least a qualitative comparison of the relative strengths of the various paths. Use of the pulsed source of earlier experiments would allow the identification, in the time domain, of each path by its characteristic propagation time.

Similarly, undesirable paths such as backscatter from the edges of the finite base and diffraction around barrier sides would have propagation times longer than the longest (S'DR') path of interest and could be eliminated in the time domain. The results of this experiment are shown in Figure 36, compared to the calculated arrival times of each of the four paths. It is clear from these results that the four paths constructed from the source, receiver and their images in the base are the dominant paths in this basic barrier configuration. If any other paths exist, they must be of relatively low level or coincide with one or more of the four basic paths. The path due to the "image of the source in the barrier" as discussed by Isei [Ref. 5] would coincide with the SDR and SDR' paths of Figure 36. The relative amplitude of the various paths also behave as expected, with the later arrivals (longer paths) having lower amplitudes.

The strengths of the various paths were examined by varying the geometry slightly. By increasing the barrier height to 42 cm and changing the receiver location (Figure 37), the separation in time between the paths was increased enough to allow a separate spectrum analysis of each pulse. The data of Figure 38, taken with the source/receiver oriented to insonify/receive both SDR and S'DR paths equally (approximately), show the separation between the two pulses, and the general trend in their amplitudes. As expected, the S'DR pulse appears to be an exact replica of the SDR pulse.



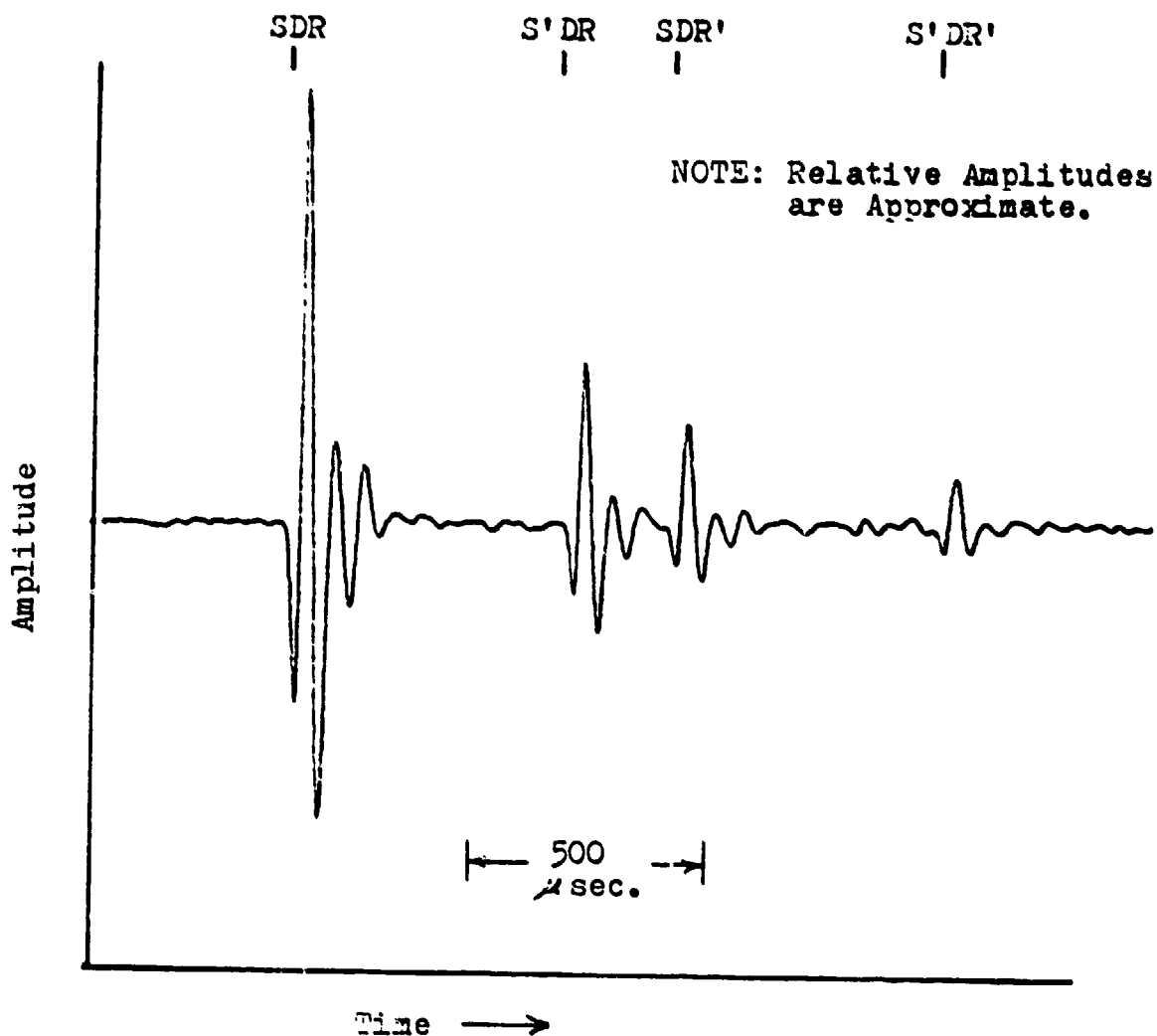


Figure 36. Total Received Time Domain Signal Due to the Four Paths of Barrier on Base (Geometry of Fig. 35).

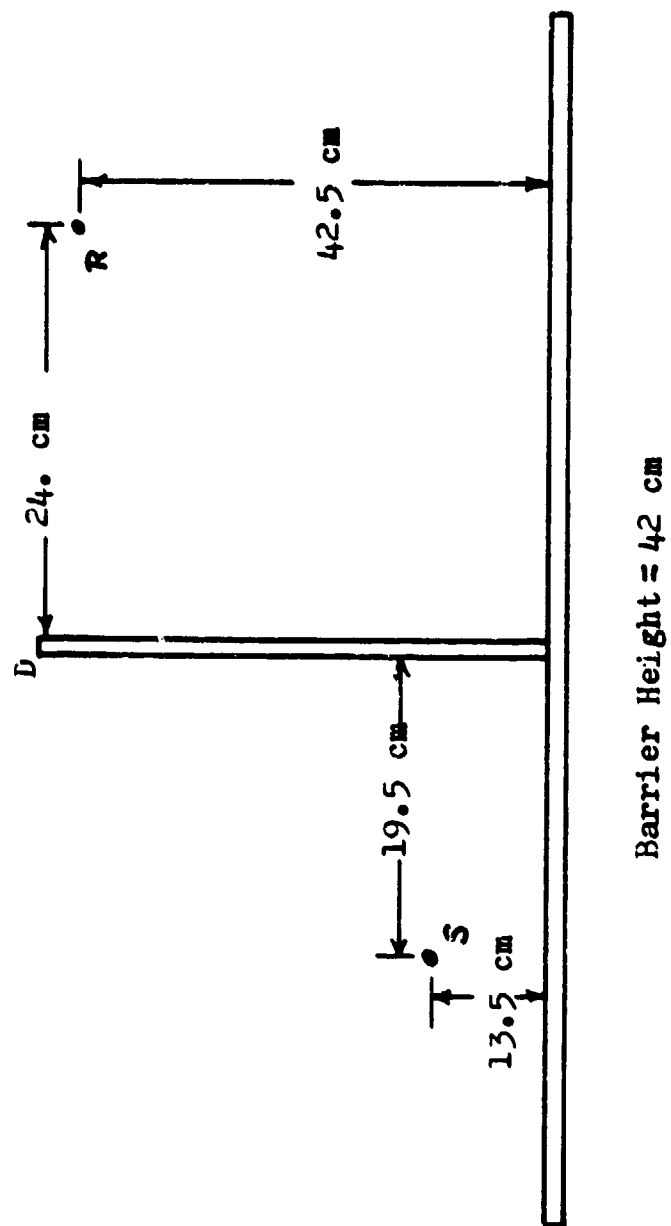


Figure 37. Geometry of Barrier on Rigid Base, Tall Barrier.

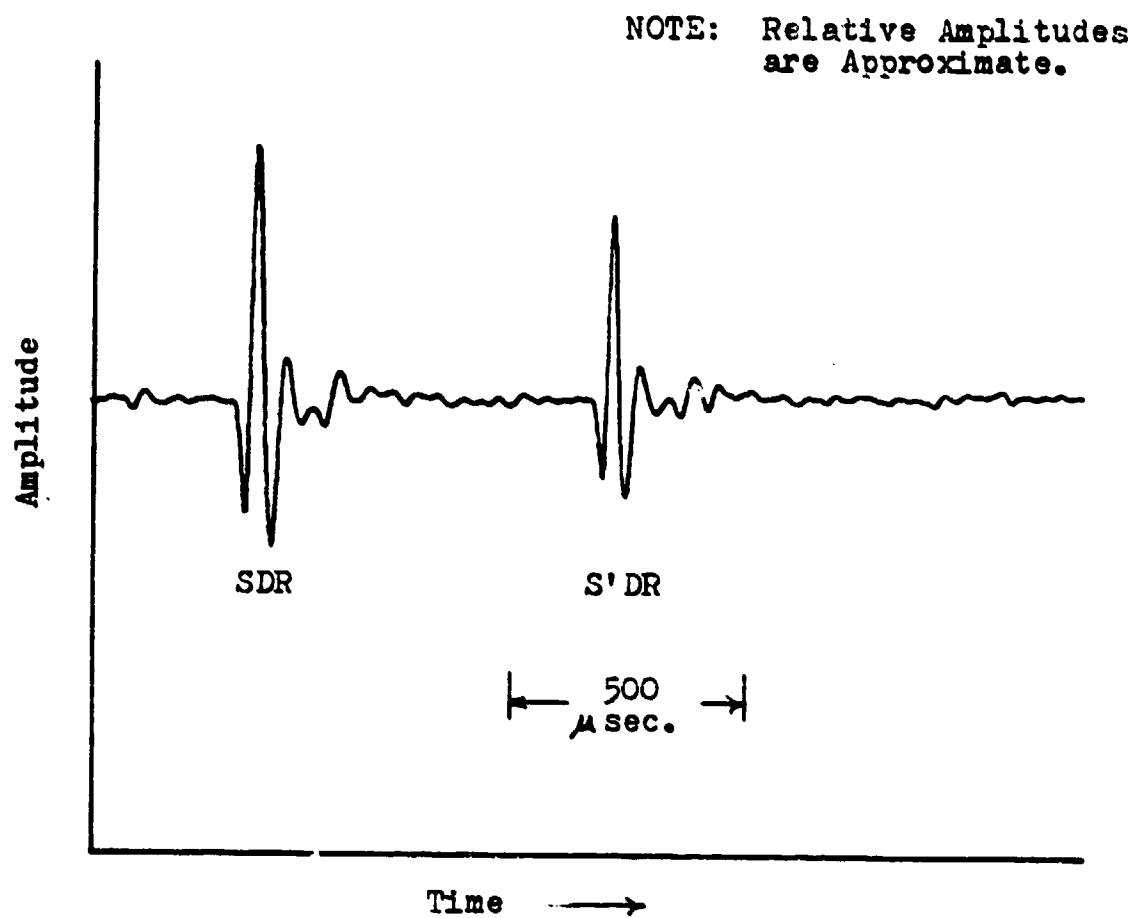


Figure 38. Received Time Domain Signal Due to the SDR and S' DR paths (Geometry of Fig. 37).

The actual strength of each path was measured by "pointing" the source in the direction of the path of interest (the receiver always pointed toward the edge, D) and Fourier transforming only the received pulse corresponding to that path. This was done for both the SDR and S'DR paths. The data, normalized by the free field pressure at the receiver with the barrier and base removed, (source/receiver pointed at each other) are presented in Figure 39. Also presented for comparison are the B-T infinite half-plane theoretical results for each path. The agreement between theory and measurements shown in Figure 39 is excellent, indicating that the diffracted field at the receiver due to SDR and S'DR paths may be computed separately, using the geometry of the source and the image of the source in the base. The total diffracted pressure at the receiver may then be obtained by adding the contributions of each path.

It is important to note that the theoretical results in Figure 39 were obtained from the complete form of the B-T infinite half-plane solution. The complete theoretical solution for the diffracted field at R in Figure 35 consists of the sum of four terms. Isei [Ref. 5] approaches the same problem by adding the contributions of six different paths, as shown in Figure 3 of Reference 5. It appears that he has used the solution due to Macdonald in a form which is separated into "real" and "image" components as discussed in section II and is applying these separately to the six paths.

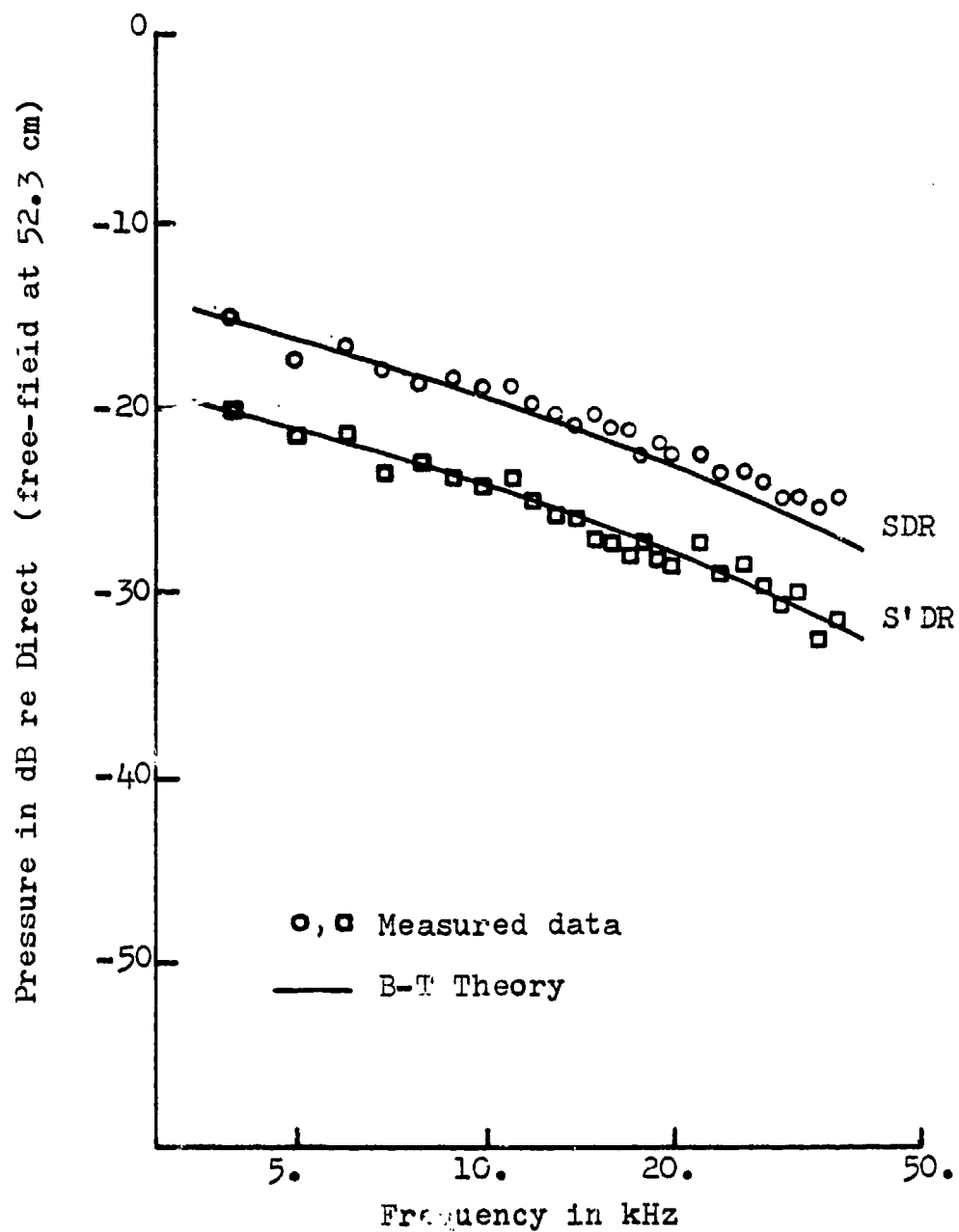


Figure 39. Diffracted Pressure as a Function of Frequency for the SDR and S'DR Paths Compared to the B-T Theory (Geometry of Fig. 37).

Figure 39 shows that the correct approach is to apply the complete solution (e.g. in Macdonald's solution this would be the sum of the "real" and "image" source components) to each of the four paths to obtain the correct diffracted field. One need not consider the "image of the source in the barrier" because it is an integral part of the complete solution.

In addition to the four paths described earlier, it is possible to have an additional path which propagates from the source, diffracts at the intersection of the barrier and base B, then diffracts over the top edge of the barrier to the receiver, shown in Figure 40 as SBDR. This assumes a non-perpendicular intersection of barrier and base since Tolstoy [Ref. 7] shows that there will be no diffraction from a  $90^\circ$  "interior" corner. The theoretical prediction of this diffracted pressure at the receiver was approached in the same way as for the thin strip, discussed earlier.

The geometry shown in Figure 40 was constructed of 3/16" aluminum, as before, with the source and receiver located as shown. The SDR and SEDR paths (see Figure 40) can be seen directly in the time domain in Figure 41. (The relative amplitudes are only approximate due to source directivity.) Once again, the source was pointed toward the path of interest and the received pulse was analyzed separately. The frequency spectrum of the SBDR pulse, normalized by the direct, free-field pressure, is shown in Figure 42. Also shown is the

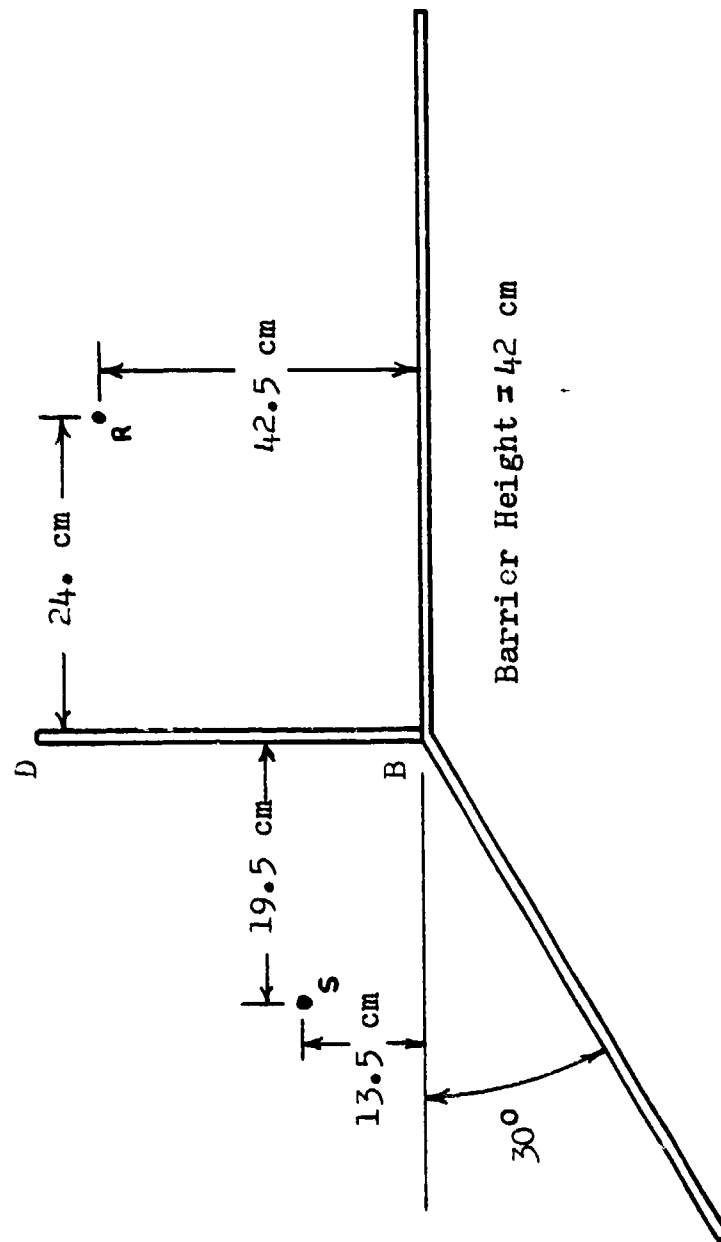


Figure 40. Geometry of Barrier on Angled Base.

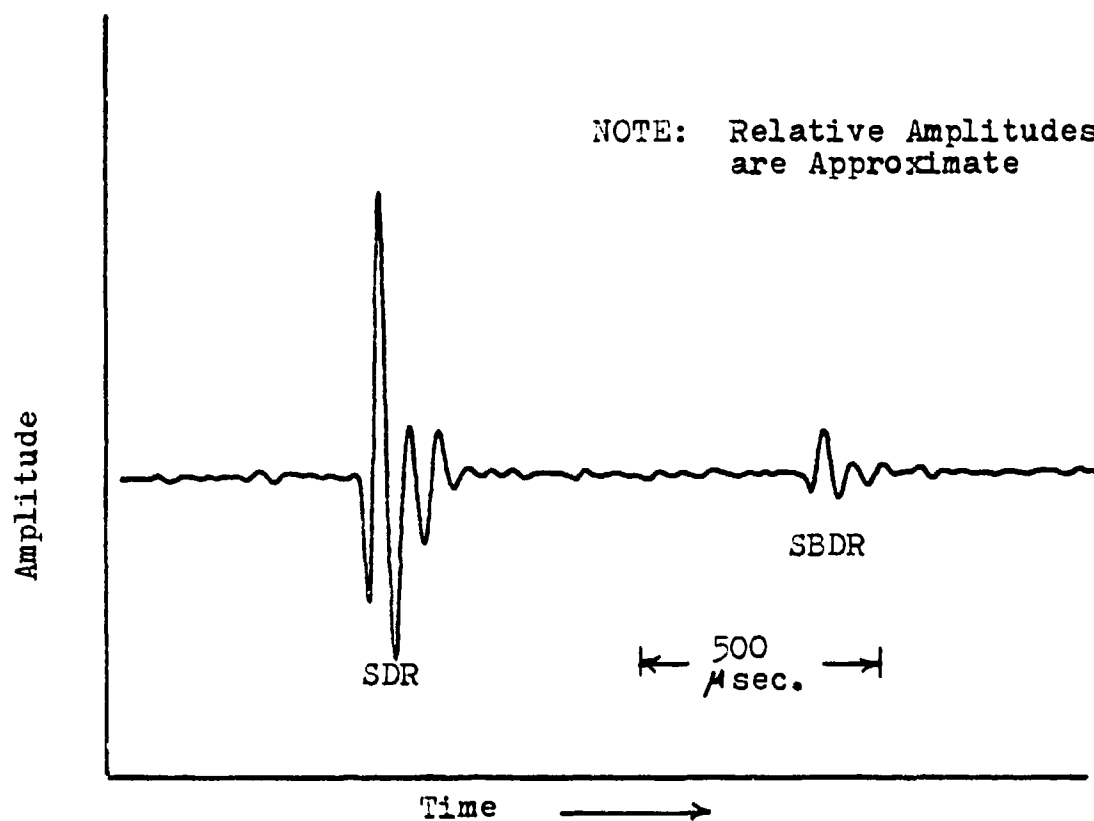


Figure 41. Received Time Domain Signal Due to the SDR and SBDR Paths (Geometry of Fig. 40).



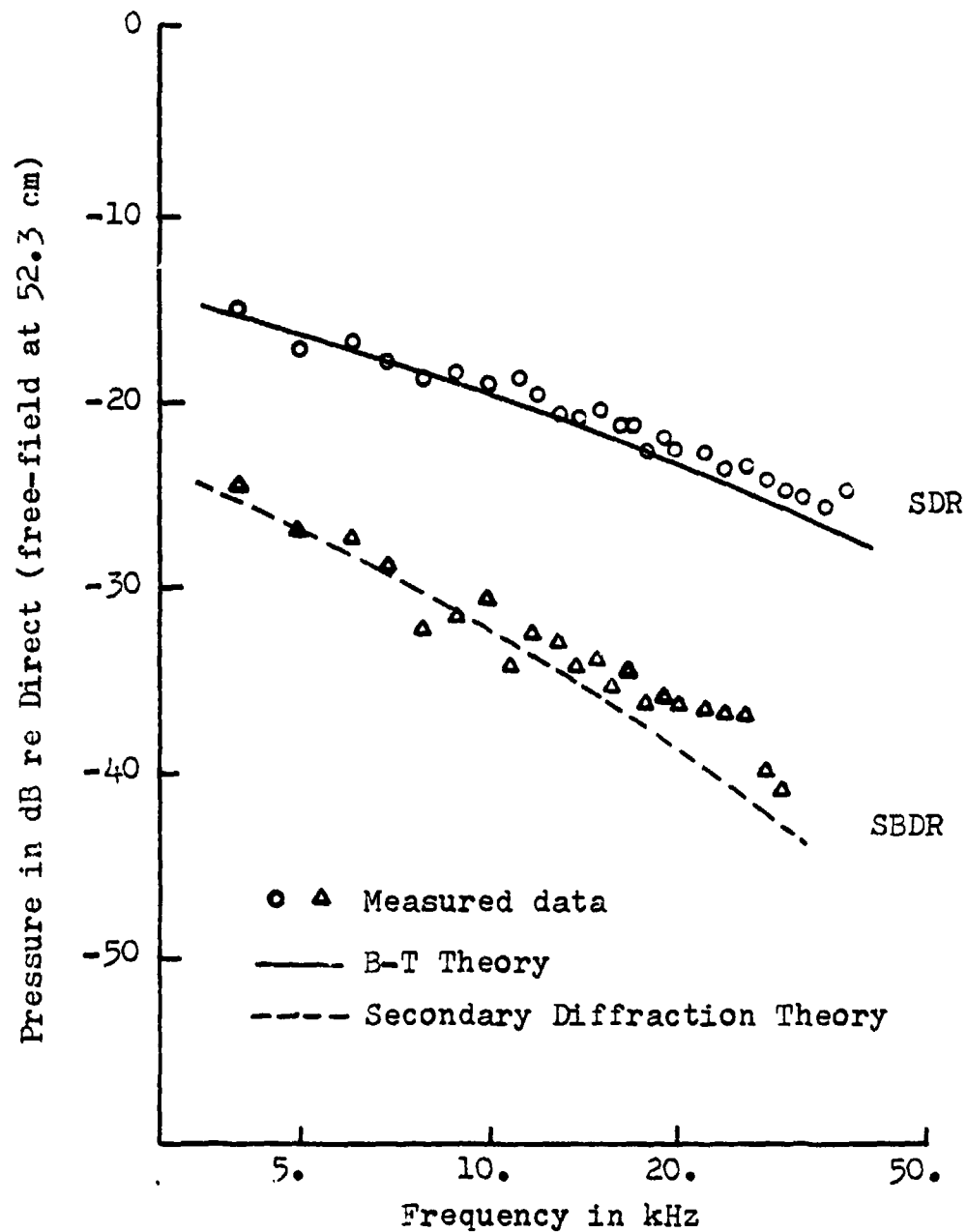


Figure 42. Diffracted Pressure as a Function of Frequency for the SDR and SBDR Paths Compared to the B-T Theory and Secondary Diffraction Theory, respectively (Geometry of Fig. 40).

theoretical result from the secondary diffraction program. For comparison, the SDR path data and theory from Figure 39 are also presented. (The SDR geometry is identical to the previous experiment.) The additional diffraction in the SBDR path is seen in the data as a different frequency dependence as well as a lower overall level. When the B-T theory is used as a basis for secondary diffraction, there is excellent agreement with the measured data.

## VII. CONCLUSIONS

The exact impulse diffraction solution of Biot and Tolstoy (B-T) has been compared to the exact CN diffraction solution of Macdonald for forward scattering and to the impulse solution to the Helmholtz equation (H-K) for backscatter using the Kirchhoff approximation. For backscatter from an infinite edge, B-T and H-K have been found to reduce to a similar although analytically different time domain form. Comparison of B-T and H-K in the frequency domain showed substantial disagreement, except for geometries where the diffracted pulse was close to the reflected pulse in time, where both solutions approached the same value. Backscatter near the plate was found to be grossly underestimated by the H-K solution, due to the boundary condition used by Kirchhoff to simplify the integral. The backscattered pressure near the surface predicted by B-T was confirmed by laboratory measurement.

Macdonald and B-T solutions for forward diffraction from a plate were both found to be in good agreement with the experiment. Both solutions can be expressed as the sum of a term containing the source/receiver angles as  $(\theta - \theta_0)$  and a term containing  $(\theta + \theta_0)$ . These terms were originally identified by Macdonald as the "real" and "image" source terms. The concept of "image of the source in the barrier", as used

in the noise control literature, is found to be a misinterpretation of Macdonald's solution. For a barrier on a rigid base, the diffracted pressure due to the real source and the true image source (the image of the source in the base) were measured separately and both were found to agree with the complete (both  $\theta - \theta_0$  and  $\theta + \theta_0$  terms) B-T solution.

The solution of finite barrier problems was found to be facilitated by the time domain, impulse nature of the B-T solution. Measurements of forward diffraction near a plate corner show that Medwin's proposed approach of truncating the B-T time domain solution to account for the corner accurately predicts the diffracted field. Experimental results do not agree with simple spherical radiation from the corner over most of the range of  $kr$  between 1 and 150. Limited data do show a trend toward spherical divergence as  $kr$  approaches 150. Measurements of the forward diffraction by a thin strip confirm the presence of secondary diffraction, i.e., waves that first diffract at one edge, propagate across the surface of the strip, and diffract again at the other edge. The time domain B-T solution is shown to be a useful starting point in characterizing this secondary diffraction. At high frequencies, forward diffraction loss by a plate of finite thickness is found to be considerably greater than the theoretical prediction, for an infinitely thin screen. It appears that this may also be explained by the double edge creating secondary diffraction with an additional diffraction contribution at the second edge.

## APPENDIX: A

### APPROXIMATION OF THE BIOT-TOLSTOY SOLUTION NEAR THE SHADOW BOUNDARY

Since the B-T solution is a delta function impulse solution, it is expected that it will approach the delta function form for limiting cases where the receiver is approaching the boundary between "illuminated" and "shadow" regions, herein referred to as the shadow boundary. As this limit is approached, the early time portion of the diffracted pulse will increasingly dominate the solution, creating a difficult numerical calculation problem. To better understand this problem, the solution will be approximated for the following conditions:

- A.  $\theta_w = 2\pi$  (thin plate)
- B.  $\theta = \theta_o + \pi + \epsilon$  (receiver in the shadow region,  $\epsilon$  small)
- C.  $t - \tau_o \rightarrow 0$  from the positive side (early diffracted pulse)

For  $\theta_w = 2\pi$ , the complete solution can be written as

$$p(t) = - \frac{S_0 c}{8\pi^2} \{\beta\} [rr_o \sinh Y]^{-1} [\exp(-Y/2)] \quad (A-1)$$

where

$$Y = \arg \cosh \left[ \frac{c^2 t^2 - (r^2 + r_o^2 + z^2)}{2rr_o} \right] \quad (A-2)$$

and  $\beta$  is a four term sum written symbolically as

$$\beta = \frac{\sin[\frac{1}{2}(\pi \pm \theta \pm \theta_0)]}{1 - 2\exp(-\frac{1}{2}Y)\cos[\frac{1}{2}(\pi \pm \theta \pm \theta_0)] + \exp(-Y)} \quad (A-3)$$

For the early diffracted pulse

$$\Delta t = t - \tau_0 \rightarrow 0$$

Medwin [Ref. 8] shows that when  $\frac{\Delta t}{\tau_0} \ll 1$ , the factor containing  $\sinh Y$  can be approximated as

$$(rr_0 \sinh Y)^{-1} \approx (2 t_0 c^2 rr_0)^{-\frac{1}{2}}$$

(This same result for the specific case of backscatter was shown in section III.) This factor goes to infinity as  $\Delta t$  approaches zero and is generally assumed to be the factor that determines the time dependence of  $p(t)$  under these circumstances. Time dependence also enters A-1 through the  $\exp(-Y/2)$  term but this will be ignored because this function only varies between 1 and zero and is relatively constant for  $Y$  (and therefore  $\Delta t$ ) approaching zero.

The  $\beta$  term contains both time and geometry dependence in a rather complex way. The approach here will be to separate the  $\beta$  into four terms and examine each one in the limit as both  $Y$  and  $\epsilon$  approach zero. ( $Y$  is directly, although not linearly, related to  $\Delta t$ . The expansion of  $\arg \cosh$  is not trivial and so the limiting procedure here will be with respect to  $Y$  rather than  $t$ .) The  $\beta$  term can be written as  $(\beta_{++} + \beta_{+-} + \beta_{-+} + \beta_{--})$  with the subscripts referring to the various combinations as shown in Table (A-1).

TABLE A-1

TERM	COMBINATION OF $\pi, \theta, \theta_0$	SUBSTITUTION OF $\theta = \theta_0 + \pi + \epsilon$
$\beta_{++}$	$\pi + \theta + \theta_0$	$2\pi + 2\theta_0 + \epsilon$
$\beta_{+-}$	$\pi + \theta - \theta_0$	$2\pi + \epsilon$
$\beta_{-+}$	$\pi - \theta + \theta_0$	$-\epsilon$
$\beta_{--}$	$\pi - \theta - \theta_0$	$-(2\theta_0 + \epsilon)$

Using the usual, first order approximations for sine and cosine of small angles, these terms can be approximated by the following

$$\begin{aligned}
 \beta_{++} &\approx - \frac{\sin \theta_0 + \epsilon/2 \cos \theta_0}{1 + 2 \exp(-Y/2) [\cos \theta_0 - \epsilon/2 \sin \theta_0] + \exp(-Y)} \\
 \beta_{+-} &\approx - \frac{\epsilon/2}{1 + 2 \exp(-Y/2) + \exp(-Y)} \\
 \beta_{-+} &\approx - \frac{\epsilon/2}{1 - 2 \exp(-Y/2) + \exp(-Y)} \\
 \beta_{--} &\approx - \frac{\sin \theta_0 + \epsilon/2 \cos \theta_0}{1 - 2 \exp(-Y/2) (\cos \theta_0 + \epsilon/2 \sin \theta_0) + \exp(-Y)}
 \end{aligned} \tag{A-4}$$

With these first order approximations, the behavior of each  $\beta$  term can be examined at  $Y = 0$

$$\begin{aligned}
 \beta_{++}|_{Y=0} &\approx - \frac{\sin \theta_0 + \epsilon/2 \cos \theta_0}{2(1 + \cos \theta_0 - \epsilon/2 \sin \theta_0)} \\
 \beta_{--}|_{Y=0} &\approx - \frac{\sin \theta_0 + \epsilon/2 \cos \theta_0}{2(1 - \cos \theta_0 - \epsilon/2 \sin \theta_0)} \\
 \beta_{+-}|_{Y=0} &\approx - \frac{\epsilon}{8} \\
 \beta_{-+}|_{Y=0} &\approx (\text{denominator goes to zero})
 \end{aligned}$$

From this first order analysis, it is seen that three of the four  $\beta$  terms have the potential of dominating the  $p(t)$  solution at small values of  $Y$ . These terms will now be examined to second order in the denominator. (The numerator contains no difference terms and so the first order



approximation for small  $\epsilon$  will be retained for simplicity.)

Considering  $\beta_{-+}$ , the following approximations are used

$$\cos(-\epsilon/2) \approx 1 - \frac{\epsilon^2}{8}$$

$$\exp(-Y) \approx 1 - Y + \frac{Y^2}{2}$$

to obtain

$$\beta_{-+} \approx - \frac{2\epsilon}{Y^2 + \epsilon^2 - \frac{Y\epsilon^2}{2} + \frac{Y^2\epsilon^2}{8}}$$

Neglecting terms higher than second order in the small quantities  $Y$  and  $\epsilon$ ,

$$\beta_{-+} \approx - \frac{2\epsilon}{Y^2 + \epsilon^2(1-Y/2)} \quad (A-5)$$

which approaches a finite value as  $Y$  approaches 0,

$$\lim_{Y \rightarrow 0} \beta_{-+} = - \frac{2}{\epsilon}$$

Using an identical approach yields the following results for  $\beta_{++}$  and  $\beta_{--}$ :

$$\lim_{Y \rightarrow 0} \beta_{++} = - \frac{\sin \theta_0 + \epsilon/2 \cos \theta_0}{2(1 + \cos \theta_0 + \epsilon^2/8 \cos \theta_0 - \epsilon/2 \sin \theta_0)} \quad (A-6)$$

$$\lim_{Y \rightarrow 0} \beta_{--} = - \frac{\sin \theta_0 + \epsilon/2 \cos \theta_0}{2(1 - \cos \theta_0 + \epsilon^2/8 \cos \theta_0 - \epsilon/2 \sin \theta_0)} \quad (A-7)$$

A detailed analysis of the  $\beta_{++}$  and  $\beta_{--}$  terms was not done, however, they assume the following maximum values at  $Y = 0$ :

$$\begin{aligned}\beta_{++} &= \frac{2}{\epsilon} \quad \text{at } \theta_0 = \pi; Y = 0 \\ \beta_{--} &= -\frac{2}{\epsilon} \quad \text{at } \theta_0 = 0; Y = 0\end{aligned}$$

Since these limiting values are the same as for the  $\beta_{-+}$  term and will be less for other values of  $\theta_0$ , it is concluded that the  $\beta_{-+}$  term will dominate  $\beta$  for the early diffracted pulse.

For comparison, the  $(rr_0 \sinh Y)^{-1}$  term can also be approximated for  $Y$  approaching zero as

$$(rr_0 \sinh Y)^{-1} = \frac{1}{rr_0} (Y + \frac{Y^3}{6} + \dots)^{-1} \approx \frac{1}{rr_0 Y} \quad (\text{A-8})$$

Comparing Equations A-8 and A-5 leads to the conclusion that the  $rr_0 \sinh Y$  factor will determine the time dependence of the early diffracted pulse only when  $\epsilon^2$  is much greater than  $Y^2$  and  $Y$  is much less than 1.

In terms of the basic diffraction problem geometry, this means that as the receiver approaches the shadow boundary from inside the shadow ( $\epsilon$  approaches zero), the time region over which the  $(rr_0 \sinh Y)^{-1}$  factor will determine the time dependence of  $p(t)$  becomes very small. This region must be determined, based on the geometry, before an analytical plus digital approach such as outlined by Medwin [Ref. 8] can be employed. This is illustrated in Figures A-1, A-2 which show the behavior of  $(\sinh Y)^{-1}$  and  $\beta_{-+}$  as a function of  $Y$  for two values of  $\epsilon$ . Since the B-T solution contains the product of these terms, one can be assumed to be the factor which determines the time dependence only when the slope of the other

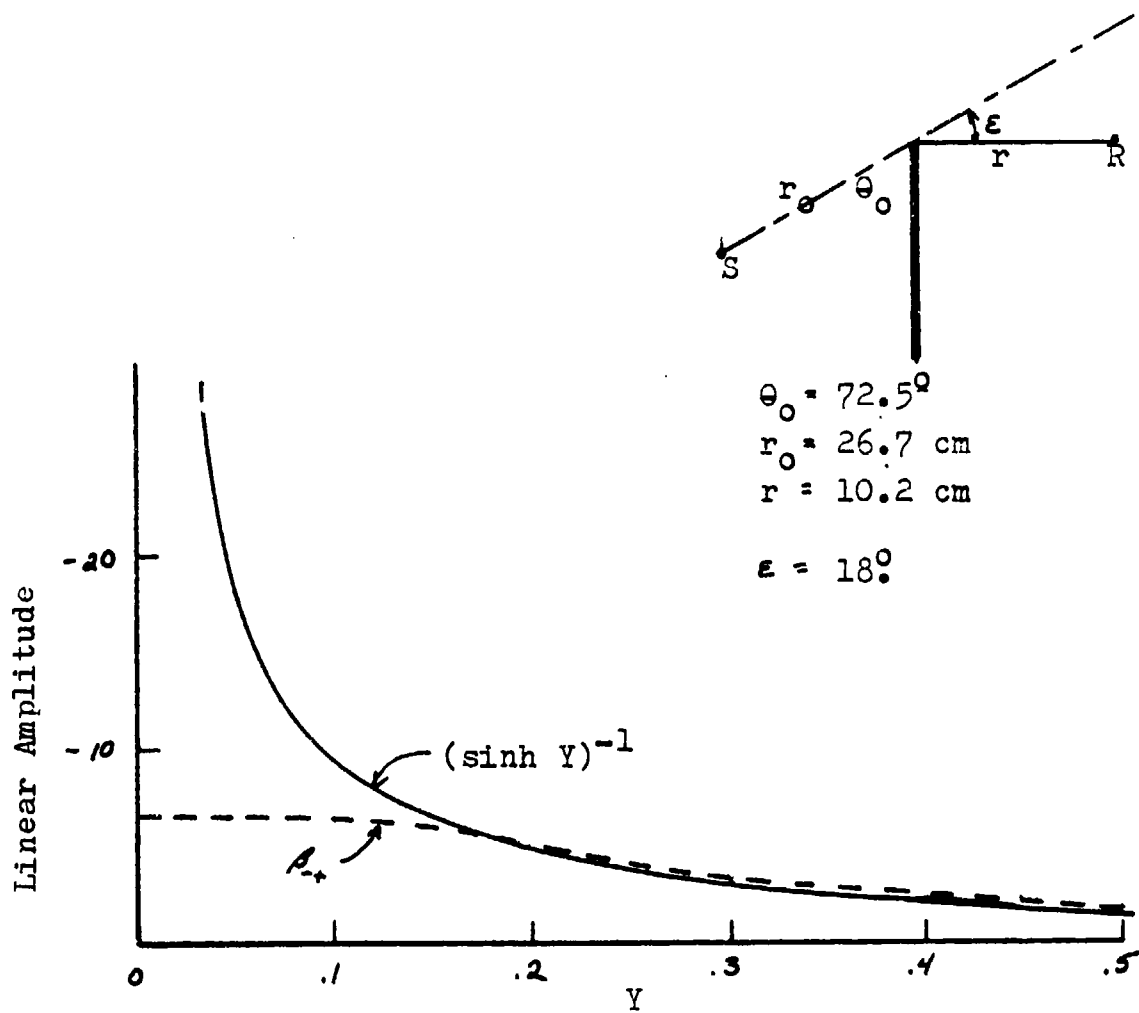


Figure A-1 Behavior of the B-T Solution Near the Shadow Boundary,  $\epsilon = 18^\circ$ .

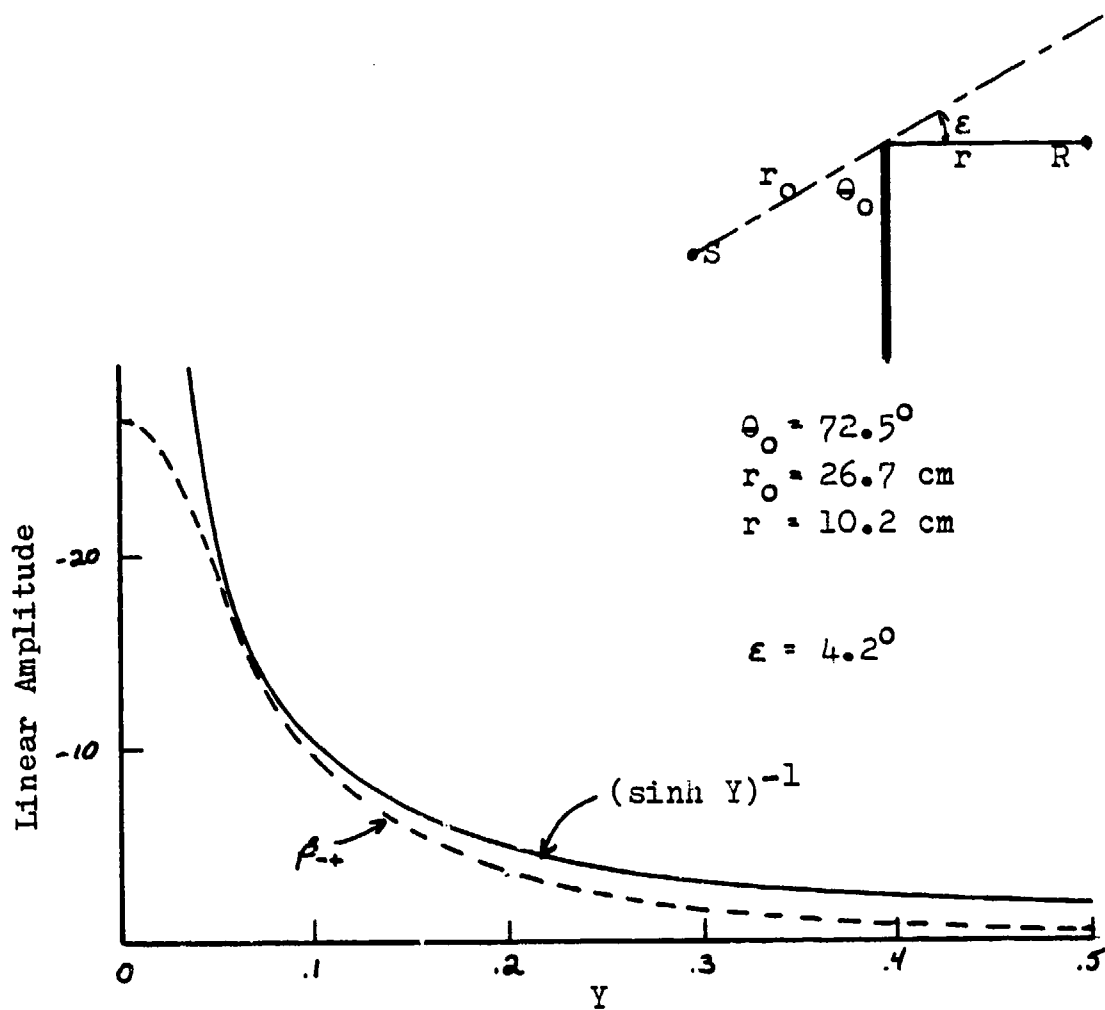


Figure A-2 Behavior of the B-T Solution Near the Shadow Boundary,  $\epsilon = 4.2^\circ$ .

approaches zero. Based on this, the  $(\sinh Y)^{-1}$  term would dominate below approximately  $Y = .1$  for  $\epsilon = 18^\circ$  and below  $Y = .01$  for  $\epsilon = 4.2^\circ$ .

# LIST OF REFERENCES

1. Sommerfield, A., Mathematische Annalen, v. 47, p. 317, 1896.
2. Carslaw, H. S., Proceedings of the London Mathematical Society, v. 30, p. 121, 1899.
3. Macdonald, H. M., "A Class of Diffraction Problems", Proceedings of the London Mathematical Society, v. 14, p. 410, 1915.
4. Biot, M. A. and Tolstoy, I., "Formulation of Wave Propagation in Infinite Media by Normal Coordinates with an Application to Diffraction", The Journal of the Acoustical Society of America, v. 29, p. 381, 1957.
5. Isei, T., Embleton, T. F. W., and Piercy, J. E., "Noise Reduction by Barriers on Finite Impedance Ground", The Journal of the Acoustical Society of America, v. 67, p. 46, 1980.
6. Baker, B. B. and Copson, E. T., The Mathematical Theory of Huygen's Principle, 2nd ed., Oxford. 1950.
7. Tolstoy, I., Wave Propagation, McGraw-Hill, 1973.
8. Medwin, H., "Shadowing by Finite Noise Barriers", The Journal of the Acoustical Society of America, (to be published in the April 1981 issue).
9. Watson, G. N., A Treatise on the Theory of Bessel Functions, 2nd ed., The Macmillan Company, 1945.
10. Clay, C. S. and Medwin, H., Acoustical Oceanography: Principles and Applications, John Wiley and Sons, 1977.
11. Kawai, T., Fujimoto, K., and Itow, T., "Noise Propagation Around a Thin Half-Plane", Acustica, v.38, p. 313, 1977.
12. Bremhorst, J. H., Impulse Wave Diffraction by Rigid Wedges and Plates, M. S. Thesis, Naval Postgraduate School, Monterey, CA., 1978.
13. Bowman, J. J., Senior, T. B. A., and Uslenghi, P. L. E., Electromagnetic and Acoustic Scattering by Simple Shapes, North-Holland Publishing Co., Amsterdam, 1969.

14. Decker, W., Backscatter from a Composite Rough Surface, M. S. Thesis, Naval Postgraduate School, Monterey, CA., Dec. 1980.
15. Frederiksen, E., "Condenser Microphones Used as Sound Sources", Bruel and Kjaer Technical Review, No. 3, 1977.
16. Keller, J. B., "Diffraction by an Aperture", Journal of Applied Physics, v. 28, p. 426, 1957.
17. Hutchins, D. L., and Kouyoumjian, R. G., "Calculation of the Field of a Baffled Array by the Geometrical Theory of Diffraction", The Journal of the Acoustical Society of America, v. 45, p. 485, 1969.

INITIAL DISTRIBUTION LIST

	No. Copies
1. Library, Code 0142 Naval Postgraduate School Monterey, California 93940	2
2. Department Chairman, Code 61 Department of Physics and Chemistry Naval Postgraduate School Monterey, California 93940	2
3. Professor H. Medwin, Code 61Md Department of Physics and Chemistry Naval Postgraduate School Monterey, California 93940	6
4. Professor K. Woehler, Code 61Wh Department of Physics and Chemistry Naval Postgraduate School Monterey, California 93940	1
5. Professor C. S. Clay University of Wisconsin 1215 W. Dayton Street Madison, Wisconsin 53706	1
6. Gary M. Jebsen Code 1932 David Taylor Naval Ship R&D Center Bethesda, MD 20084	1
7. Director of Defense Research and Engineering Office of the Secretary of Defense Washington, D.C. 20301 ATTN: Office, Assistant Director (Research)	1
8. Professor I. Tolstoy Knockvennie, Castle Douglas S. W. SCOTLAND	1
9. Professor K. Gray, Code 62Gy Department of Electrical Engineering Naval Postgraduate School Monterey, California 93940	1



	No. Copies
10. Defense Technical Information Center Cameron Station Alexandria, Virginia 22314	2
11. Director Naval Research Laboratory Washington, D.C. 20375 ATTN: Library, Code 2620	6
12. Office of Naval Research Arlington, Virginia 22217 ATTN: (Code 480) ATTN: (Code 460) ATTN: (Code 102-OS) ATTN: (Code 102IP)	3 1 1 6
13. Dr. M. Sevik Code 19 David Taylor Naval Ship R&D Center Bethesda, MD 20084	1
14. Mr. J. F. O'Donnell Code 193 David Taylor Naval Ship R&D Center Bethesda, MD 20084	1
15. Dr. W. G. Neubauer, Code 8132 Naval Research Laboratory 4555 Overlook Avenue Washington, D.C. 20375	1
16. Dr. J. Piercy Physics Division National Research Council Ottawa, Ontario K1A 0S1 CANADA	1
17. Dr. S. Hayek Pennsylvania State University 224 Hammond University Park, PA 16802	1
18. Dr. Tony F. W. Embleton Department of Physics National Research Council Montreal Road Ottawa, Ontario K1A 0S1 CANADA	1

No. Copies

19. Ms. Emily Childs  
Code 61  
Department of Physics and Chemistry  
Naval Postgraduate School  
Monterey, California 93940

1